AFRL-RV-PS-
TR-2019-0066

REGIONAL WAVE PROPAGATION INCLUDING SMALL-SCALE HETEROGENEITIES AND Q(F)

Kim Olsen and Te-Yang Yeh

San Diego State University
Dept of Geol. Sci.
GMCS – 213A
San Diego, CA 92182

30 May 2019

Final Report

AIR FORCE RESEARCH LABORATORY
Space Vehicles Directorate
3550 Aberdeen Ave SE
AIR FORCE MATERIEL COMMAND
KIRTLAND AIR FORCE BASE, NM 87117-5776

DITC COPY

NOTICE AND SIGNATURE PAGE

Using Government drawings, specifications, or other data included in this document for any purpose other than Government procurement does not in any way obligate the U.S. Government. The fact that the Government formulated or supplied the drawings, specifications, or other data does not license the holder or any other person or corporation; or convey any rights or permission to manufacture, use, or sell any patented invention that may relate to them.

This report was cleared for public release by AFMC/PA and is available to the general public, including foreign nationals. Copies may be obtained from the Defense Technical Information Center (DTIC) (http://www.dtic.mil).

AFRL-RV-PS-TR-2019-0066 HAS BEEN REVIEWED AND IS APPROVED FOR PUBLICATION IN ACCORDANCE WITH ASSIGNED DISTRIBUTION STATEMENT.

//SIGNED//	//SIGNED//
Dr. Frederick Schult Program Manager, AFRL/RVB	Dr. Thomas R. Caudill, Chief AFRL Geospace Technologies Division

This report is published in the interest of scientific and technical information exchange, and its publication does not constitute the Government's approval or disapproval of its ideas or findings.

REPORT DOCUMENTATION PAGE

Form Approved
OMB No. 0704-0188

1. REPORT DATE *(DD-MM-YYYY)*	**2. REPORT TYPE**	**3. DATES COVERED** *(From - To)*
30-05-2019	Final Report	1 May 2016 – 30 Apr 2019

4. TITLE AND SUBTITLE

Regional Wave Propagation Including Small-Scale Heterogeneities and Q(f)

5a. CONTRACT NUMBER

FA9453-16-C-0017

5b. GRANT NUMBER

5c. PROGRAM ELEMENT NUMBER
62601F

6. AUTHOR(S)

Kim Olsen and Te-Yang Yeh

5d. PROJECT NUMBER
1010

5e. T00019634ASK NUMBER
PPM00019634

5f. WORK UNIT NUMBER
EF128702

7. PERFORMING ORGANIZATION NAME(S) AND ADDRESS(ES)

San Diego State University
Dept of Geol. Sci.
GMCS – 213A
San Diego, CA 92182

8. PERFORMING ORGANIZATION REPORT NUMBER

9. SPONSORING / MONITORING AGENCY NAME(S) AND ADDRESS(ES)

Air Force Research Laboratory
Space Vehicles Directorate
3550 Aberdeen Avenue SE
Kirtland AFB, NM 87117-5776

10. SPONSOR/MONITOR'S ACRONYM(S)
AFRL/RVBN

11. SPONSOR/MONITOR'S REPORT NUMBER(S)
AFRL-RV-PS-TR-2019-0066

12. DISTRIBUTION / AVAILABILITY STATEMENT

Approved for public release; distribution is unlimited. (AFMC-2019-0435 dtd 18 Jul 19).

13. SUPPLEMENTARY NOTES

14. ABSTRACT

High-frequency synthetics computed in the SALSA3D velocity model overpredict Rayleigh wave amplitudes by more than an order of magnitude while underpredicting coda amplitudes on the Korean Peninsula. However, ensemble 0-4 Hz FD simulations of regional wave propagation with addition of a von Karman distribution of small-scale heterogeneities with correlation lengths of ~1 km, Hurst number of 0.1, horizontal-to-vertical anisotropy of ~5 and s=10% in the top ~7.5 km of the crust produce synthetic envelopes in general agreement with data. Deeper scattering tends to decrease the initial P wave amplitudes to levels much below those for the data. The synthetics accurately predict Pg, Lg, and Pg/Lg ratios, while Pn and Sn amplitudes and associated ratios are likely biased from erroneous upper mantle SALSA3D Vp and Vs gradients. Array analysis for KSRS data and synthetics using NKNTS events supports our favored statistical models of crustal small-scale heterogeneities. The predominant S wave train for deep double-couple sources very efficiently generates converted S-P scattered waves after Pn, in contrast to shallow explosive sources. Both data and simulations show efficient Lg propagation along continental Asia paths and less efficient propagation across the Sea of Japan, consistent with the findings of published simulations for earthquake sources. Topography on the Korean Peninsula can be well approximated by a power-law PSD with an exponent of 3.5.

15. SUBJECT TERMS
seismic scattering, high frequency scattering, seismic attenuation

16. SECURITY CLASSIFICATION OF:			**17. LIMITATION OF ABSTRACT**	**18. NUMBER OF PAGES**	**19a. NAME OF RESPONSIBLE PERSON**
a. REPORT	**b. ABSTRACT**	**c. THIS PAGE**			Dr. Frederick Schult
Unclassified	Unclassified	Unclassified	Unlimited	82	**19b. TELEPHONE NUMBER** *(include area code)*

This page is intentionally left blank.

Table of Contents

List of Figures

1. SUMMARY

We have carried out 3D finite difference simulations (FD) of regional wave propagation for North Korea nuclear explosions and validated the results against instrument-corrected records at stations in South Korea and Japan. Synthetics computed in the relatively smooth Sandia/Los Alamos National Laboratory SALSA3D velocity model significantly overpredict Rayleigh wave amplitudes by more than an order of magnitude while underpredicting coda amplitudes at stations INCN and TJN in South Korea. The addition to SALSA3D of a von Karman distribution of small-scale heterogeneities with correlation lengths of ~1,000 m, Hurst number of 0.1, and horizontal-to-vertical anisotropy of ~5 produces synthetics in general agreement with the data. The best fits are obtained from models with a gradient in the strength of the velocity and density perturbations, and strong scattering (10%) limited to the top 7.5-10 km of the crust. Deeper scattering tends to decrease the initial P wave amplitudes to levels much below those for the data, a critical result for methods discriminating between explosive and earthquake sources. In particular, the amplitude at the onset of P_n can be affected by as little as 2% small-scale heterogeneity in the lower crust and upper mantle. Simulations including constant Q of 200-300 below 1 Hz and a power-law Q(f) formulation at higher frequencies with an exponent of 0.3 (P and S-waves) generate synthetics in best agreement with the data. These results are valid for both isotropic sources and source descriptions with a 20% non-isotropic component present.

Our simulations show that S-wave energy present in the source area (e.g., generated by a triggered tectonic component) improves in particular the fit on the transverse component at regional distances for the long-period signal, as compared to that from an isotropic source. The fit for the envelope of 5-realization ensemble broadband synthetics derived from a source including a 20% non-isotropic component is comparable to that from the isotropic source. However, the results of simulations with an isotropic source where the small-scale heterogeneities are omitted in the vicinity of the source indicate that only a small amount of (high-frequency) scattering from the near-source area accumulates over the regional path. Thus, our study suggests that a large part of the high-frequency seismic energy recorded on the transverse component of the recorded waveforms is generated by P-S wave scattering primarily in the upper crust along the regional path from the source to the stations.

We measure root-mean-square amplitudes of Pn, Pg, Sn, and Lg phases in the frequency bands tabulated in Table 1 and compare P/S ratios for data and 5-realization ensemble simulations for shallow isotropic and 20% non-isotropic moment tensors, as well as 10-km deep double-couple results. The observed Pg amplitudes are well predicted in all frequency bands up to 4 Hz by explosive and double-couple sources. While the isotropic and 20% non-isotropic moment tensor sources predict similar Pg/Lg ratios, those from the double-couple source are lower by ~0.5 log units in the 2 - 4 Hz band. The simulations overpredict Pn amplitudes, particularly in the 0-2 Hz bandwidth. The large error bars associated with the Pn amplitude measurements at higher frequencies suggest that Pn amplitudes are very sensitive to the small-scale perturbations in the crust. Since Lg amplitudes are well predicted, the Pn/Lg ratios are over-predicted at various levels. Both the isotropic and the 20% non-isotropic moment tensor simulations underpredict Sn

amplitudes at the high frequencies, indicating that the inclusion of a realistic S-wave content at the source is not able to produce Sn amplitudes in agreement with data. As Sn amplitudes generated by the double-couple source are in better agreement with those from data than those generated by the explosive sources, our simulated Pn/Sn ratios are not as effective for event discrimination as Pg/Lg and Pn/Lg. The likely reason for the biased Pn and Sn amplitudes is erroneous SALSA3D Vp and Vs gradients in the upper mantle.

We carried out array analysis for KSRS data and synthetics for the North Korean Nuclear Test Site (NKNTS) events and deep double-couple events. Results for the synthetic waveforms computed without small-scale heterogeneities are highly coherent across the array, as expected. The small-scale heterogeneities dramatically lower the coherency for the simulations, to a level similar to that for the data. The back azimuths are generally in the range 0-20 degrees, representing the direct path from the NKNTS, located NNE from the array. The apparent velocities start out with ~8 km/s around the Pn arrival with high coherency and consistent direction of arrival, decreasing to ~6 km/s for Pg with very similar direction of arrival as for Pn. Following Pg, the apparent velocities and back azimuths show large variation with low coherency values. Apparent velocities converge to ~4.5 km/s at the expected window of Sn, reducing to ~4.0 km/s for Lg. Interestingly, the waves from the shallow explosive sources show a drop in apparent velocities from the expected P-wave speeds to S-wave speeds at ~80-110s. However, the phases for the double-couple source in this range are found to be P phases with speeds of ~7-8 km/s, indicating a different scattering behavior for the two different source types (e.g., P-S versus S-P scattering). This result seems to indicate that the predominant S wave train for the double-couple source is very efficiently generating converted S-P scattered waves after Pn. The back azimuths of the Lg waves indicate that early NNE directions turn toward N as time progresses within the phase window, suggesting that rays for late arriving Lg waves follow faster continental paths. The direction of coda wave arrivals following the Lg window is rather erratic, with additional paths from -60 to -80 degrees (more continental, or westerly, path). The strongly scattered late coda shows a bi-modal distribution of apparent velocities between 2-4 km/s. The synthetics for the explosive sources and data show similar patterns in the Pn and Pg windows, as well as the strong scattering following Pg, while the results for the 20% non-isotropic source reveals higher coherency and consistency in the Lg window as compared to the isotropic source, closer to that for the real data. Both shallow explosive source simulations predict less scattering after the Lg window as well as less variation in apparent velocity of the coda waves, as compared to that for data.

We have simulated 0-2 Hz wave propagation for the 20% non-isotropic source from the NKNTS to Japan to examine potential differences in the attenuation of Lg waves for the continental crust beneath the Korean Peninsula and Southwest Japan, and the oceanic crust beneath Sea of Japan. Specifically, we compare Lg/Sn ratios computed from observed and simulated waveforms at 20 stations in Korea and Japan. Generally, simulations with and without small-scale heterogeneities produce similar patterns as those for the observed paths along continental and oceanic crusts. We find that both data and simulations show more efficient Lg propagation along continental Asia to Kyushu and less efficient propagation along paths across the Sea of Japan, which is consistent with the findings of Furumura et al. (2014) for earthquake sources.

Finally, we have modeled the radially-averaged 2D Power Spectral Density (PSD) derived from the topography around the NKNTS using the same statistics as used for the small-scale heterogeneities in the current simulations. A von Karman autocorrelation function overpredicts the spectral energy for smaller wavenumbers of the topography data. On the other hand, we find that the topography can be well approximated by a power-law PSD with an exponent of 3.5. A comparison between power-law simulated and observed topography shows similar features, supporting that the estimated statistical parameters can characterize the topography.

2. INTRODUCTION

Accurate ground modeling requires that anleastic attenuation, typically parameterized by Q, be included. For frequencies less than about 1 Hz, a frequency-independent Q approach has generally been sufficient to fit the distance decay of seismic amplitudes caused by anelastic losses (e.g., Olsen, 2000; Cui et al., 2010; and many other studies). However, as frequencies increase, seismic data demands frequency dependency of Q, with progressively decreasing attenuation (e.g., Raoof et al., 1999; Lekic et al., 2009; McNamara et al., 2012; Phillips et al., 2013). Such frequency-dependency of Q can be formulated numerically for deterministic ground motion simulations (Withers et al., 2015). Moreover, as frequencies grow, small-scale heterogeneities of the medium increasingly affect the wave propagation via scattering. While not feasible to directly map the in-situ small-scale crustal variation, the velocity and density perturbations can be formulated statistically. Using such techniques, several studies have proposed ranges of the controlling parameters from analyses of sonic logs and V_s30 data (e.g., Savran and Olsen, 2016) and ambient noise modeling (Nakata and Beroza, 2015).

One objective of this study is to push the simulation of wave propagation in state-of-the-art 3D crustal models from shallow explosive sources to larger distances and higher frequencies using validation from broadband seismic data. We have reached a point where High Performance Computing (HPC) capabilities and sophistication of scientific models allow simulating high-frequency (here, up to 4 Hz) regional wave propagation to distances of several hundred kilometers. Our approach includes a highly-scalable FD method, a 3D crustal structure, Q(f), and statistical descriptions of small-scale velocity and density perturbations.

Amplitudes of regional seismic phases such as Pn, Pg, Sn, and Lg carry information on the source properties, with additional effects from the characteristics of the velocity structure. In particular, previous studies have shown that P/S ratios can be used as a powerful tool to discriminate earthquake and explosive sources. Here, we use vertical-component synthetics along a profile from the NKNTS to INCN, and compare phase amplitudes and Pn/Lg, Pg/Lg and Pn/Sn ratios for data and ensembles of synthetics for the isotropic source for frequencies between 0.5 and 4 Hz.

In order to better understand the characteristics of the wave propagation and to further validate the synthetics we calculate the apparent velocities and back azimuths for the phases travelling across the KSRS array in South Korea using our simulations. We also attempt to better understand the differences between the phases generated by

earthquakes and explosive sources. In particular, it has been suggested that Q values, needed for discrimination purposes, are different for modes propagating in the upper and lower parts of the crust. For the same reason, Q values derived from earthquake data (usually with deep sources) may provide a bias in Q due to different Lg modes than for explosions, creating a source of error in the discrimination efforts. To test this idea, we propagate both isotropic and double-couple sources from NKNTS toward INCN and analyze the resulting windowed phases in both time and frequency domains.

Lg waves are known to be generated by the superposition of post-critical S-waves trapped between the Moho discontinuity and the free-surface. Kennett and Furumura (2001) showed that long-standing Lg waves require continuous constructive interference of modes to support the strong amplitude. It is therefore expected that the attenuation of Lg waves is extremely sensitive to crustal and Moho structures. As reported by Furumura et al. (2014), Furumura and Kennett (2001) and Kennett and Furumura (2001), Lg waves lose constructive interference when encountering an abrupt change of thickness of the crust, such as the transition between continental and oceanic components. To test whether these results hold for shallow explosive sources, we compared the attenuation of simulated 0-2 Hz Lg amplitudes to those from data for paths from the NKNTS to South Korea and across the Sea of Japan for the 20% non-isotropic source.

Finally, we examine the other source of scattering, surface topography, in order to understand its statistical properties. We model the radially averaged 2D Power Spectral Density (PSD) derived from the topography around the NKNTS using the same statistics as used for the small-scale heterogeneities in the current simulations, namely colored Gaussian noise with a von Karman autocorrelation and power spectrum, as well as a power-law function. Our goal is to gain a better understanding of the differences caused by surface topography and crustal and mantle heterogeneities on the seismic wavefield.

3. METHODS, ASSUMPTIONS AND PROCEDURES

3.1 Numerical Method

We have used the AWP-ODC-GPU code to simulate the wave propagation presented in this study. AWP-ODC-GPU is a highly-scalable GPU-based anelastic wave propagation code that solves the 3D velocity-stress wave equation explicitly by a staggered-grid FD method with fourth-order accuracy in space and second-order accuracy in time (Olsen, 1994; Cui et al., 2013). The code has been extensively validated for a wide range of problems in 3D crustal models (e.g., Day et al., 2008; Bielak et al., 2010).

Anelastic attenuation plays a critical role for the regional propagation distances considered here. A power-law description of the form $Q=Q_o(f/f_o)^{\gamma}$ has been successfully used to model Q to higher frequencies, where Q_o and γ are region-dependent parameters. Here, we use the accurate coarse-grain memory-variable approach implemented in AWP-ODC by Withers et al. (2015), with separate values of Q for P-waves (Q_p) and S-waves (Q_s) specified for each grid point in the model.

3.2 Velocity Model

We have used velocity information from the SALSA3D (SAndia LoS Alamos 3D, Begnaud, 2015) global three-dimensional tomography model of the Earth's crust and mantle. The model was developed to obtain improved locations of explosive sources, with P- and S-wave velocity distributions obtained by separate tomographic inversions. Density in our calculations was calculated from V_s using the relation by Nafe and Drake (1957) for V_p<6.2 km/s, and Birch's law (Birch, 1961) for V_p>6.2, with a smooth transition between the two regions.

Figure 1 shows the distribution of V_s at a depth of 3.3 km in the region used to model the wave propagation from the North Korea nuclear test site (NKNTS), a 450 km (E-W) by 670 km (N-S) by 80 km (depth) sub-volume of the SALSA3D model at a uniform grid spacing of 100 m everywhere (24 billion grid points). Note the higher velocities inside the N-S oriented band within the Korean peninsula, as compared to the continental shelf to the east. It is clear that SALSA3D in our area of interest is considerably smooth, with apparent horizontal correlation lengths on the order of tens to hundreds of kilometers. This lack of smaller-scale variation is addressed separately through a statistical approach, in order to introduce realistic scattering for frequencies up to 4 Hz.

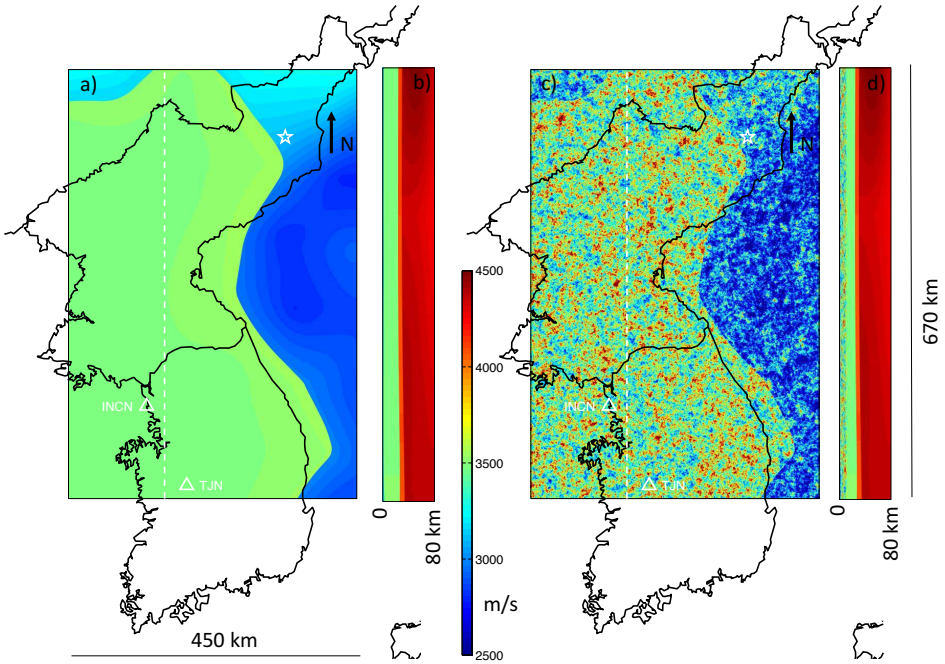

Figure 1. S-wave Velocity From the SALSA3D Model at 3.3 Km Depth Without (left, Model 1 in Table 1) and with (right, Model 6 in Table1) a Distribution of Small-scale Heterogeneities. ***Cross-sections Along the N-S Profile Denoted by the Dashed White Line are Shown to the right of the Depth Sections. The Star Denotes the Source Location for the May 25 2009 North Korea Nuclear Test. Two Stations (INCN, TJN) in South Korea with Instrument-corrected Records Available Used in This Study are Shown by White Triangles***

3.3 Source Descriptions

We model the sources for the North Korean nuclear explosions at 41.2914° North, 129.0819° East, at a depth of 600 m below the surface, consistent with the location found by Patton and Pabian (2014) for the 2009 event. Ford et al. (2009) and Shin et al. (2010) estimated a total M_w for the event of ~4.5, as well as the mb=6.3 September 3 2017 event. We use both isotropic sources, the inverted (20% non-isotropic) source by Chiang et al. (2018), and double-couple sources, in order to examine differences in S-wave generation and their path effects.

We use instrument-response corrected ground motion histories from stations on the Korean Peninsula as well as Japan (see Figure 1 for station locations). The data and simulations were processed in a similar way, and the horizontal components were rotated into radial and transverse components. Some simulations were carried out with a source low-pass filtered to 4 Hz with a 10-pole Butterworth filter with two forward passes (see Figure A1). In other cases, we used a generic deconvolution method to perform simulations with a minimum-phase source-time function (see appendices of Day et al., 2001, 2003). The idea is that there is an analytical solution to the deconvolution of a minimum-phase source-time function such that the deconvolution can be performed stably and a new source-time function of any form can be convolved into the synthetics. The minimum-phase source time function is of form

$$S(t) = \frac{t}{T^2} e^{-t/T} \quad (1)$$

where T is the characteristic time and t is time. And the inverse form of this function has a close form expression

$$S^{-1}(t) = (1 + T\frac{d}{dt})^2 \quad (2)$$

which works as a differentiation operator. Deconvolving the minimum-phase source-time function and re-convolving a new source-time function can be done with a filter

$$F(t) = S^{-1}(t) S_{new}(t) = \left(1 + T\frac{d}{dt}\right)^2 S_{new}(t)$$
$$= S_{new}(t) + 2T\frac{dS_{new}(t)}{dt} + T^2\frac{d^2 S_{new}(t)}{dt^2} \quad (3)$$

where $S_{new}(t)$ is the new source-time function. The new seismogram can be written as

$$u'(t) = u(t) * F(t) \quad (4)$$

3.4 Data and Resources

We use a GPU-enabled fourth-order accurate staggered-grid FD method (AWP-ODC-GPU, Cui et al., 2013, open source referenced (BSD-2) for our NKNTS wave propagation simulations, with discontinuous-mesh capabilities. The simulations required

between 80 mins and ~5 hours of Wall-clock time on the Oak Ridge National Laboratory (ORNL) Titan and Summit supercomputers. The observed array data for the 2009 event was obtained from the Comprehensive Test Ban Treaty Organization, data records for single stations in South Korea were downloaded from IRIS, and stations of the F-net was obtained from the National Research Institute for Earth Science and Disaster Prevention (NIED) in Japan.

4. RESULTS AND DISCUSSION

4.1 Wave Propagation From NKNTS to INCN and TJN Using SALSA3D

Several studies have reported values for Q in east Asia, typically crustal-wide estimates associated with specific phases such as P_n, P_g, S_n and L_g waves, including Mitchell et al., 1997; Xie et al., 2006; Hong and Rhie, 2009; and Ford et al., 2010. These studies typically report crustal-wide values of Q_o and γ assuming a power-law relation $Q=Q_o(f/f_o)^{\gamma}$, obtained from attenuation tomography methods. In general, these results tend to agree reasonably well for the Korean Peninsula. These studies typically report Q values associated with phases such as P_n, P_g, S_n and L_g. It is not immediately clear how these Q values relate to those for P- and S-waves, which are required for the viscoelastic modeling with AWP-ODC. As a starting point for our modeling, we select values of $Q_{os}=Q_{op}=350$ and $\gamma=0.3$ as a reference model for our simulations (Model 1, see Table 1), based on the published studies listed above.

Figure 2 shows three-component snapshots of velocity wave propagation in Model 1. The snapshots show coherent P and surface waves developing at the NKNTS at 27.5 s, with some limited P-S scattered energy developing in between. At 82.5 s the amplitudes of the P waves have diminished to a level not observable relative to that for the coherent surface waves at 82.5 s and later times. The surface waves impinge on South Korea around 137.5 s, and propagate between stations INCN and TJN at 192.5 s. The largest surface wave amplitudes are found on the vertical component, consistent with the particle motion of a Rayleigh wave. The surface waves are slowed down in the offshore area east of the Korean Peninsula due to lower seismic velocities.

Comparisons of observed and simulated 0-4 Hz waveforms in the SALSA3D model for the 2009 NKNTS at INCN are shown in Figure 3; the comparisons at TJN are shown in Appendix A, Figure A3. In these figures, and subsequent waveform comparisons, the windows of the Pn, Sn, Pg, Sg, Rg and Lg are indicated; see section 4.3.1 for the method to estimate the windows.

The radial and vertical components show large-amplitude initial P_n and P_g waves, and a strongly dispersive Rayleigh wave starting at the end of the L_g window, and persisting ~25 s past the window. The transverse component has little initial S-wave energy, but a dispersive Love wave appears simultaneously with the Rayleigh wave. It is evident from the comparison that the reference model very poorly reproduces the data from the two stations, in both time and frequency domains. Specifically, we observe the following areas in need of improvement: i) while initial (P) phases in the synthetics arrive at approximately at the expected time, their peak amplitudes are too large, ii) the surface waves are too energetic and arrive too late, iii) the amplitudes between the P wave and

surface waves are too small, and iv) the spectral amplitudes are overpredicted for frequencies higher than about 0.4 Hz.

The details of the misfits in Figures 3 and A2 suggest that our reference model is deficient in scattering by smaller-scale features, not included in the rather smooth SALSA3D model. Scattering by geological features with scale lengths less than ~10 km, insufficiently represented in the model, is expected to introduce incoherency in and therefore decrease the amplitude of the P and surface waves, as well as generate converted body waves between the P and surface wave arrivals, and increase the late coda wave train. In order to improve the waveform fits we will introduce small-scale scattering in the SALSA3D model using a statistical approach.

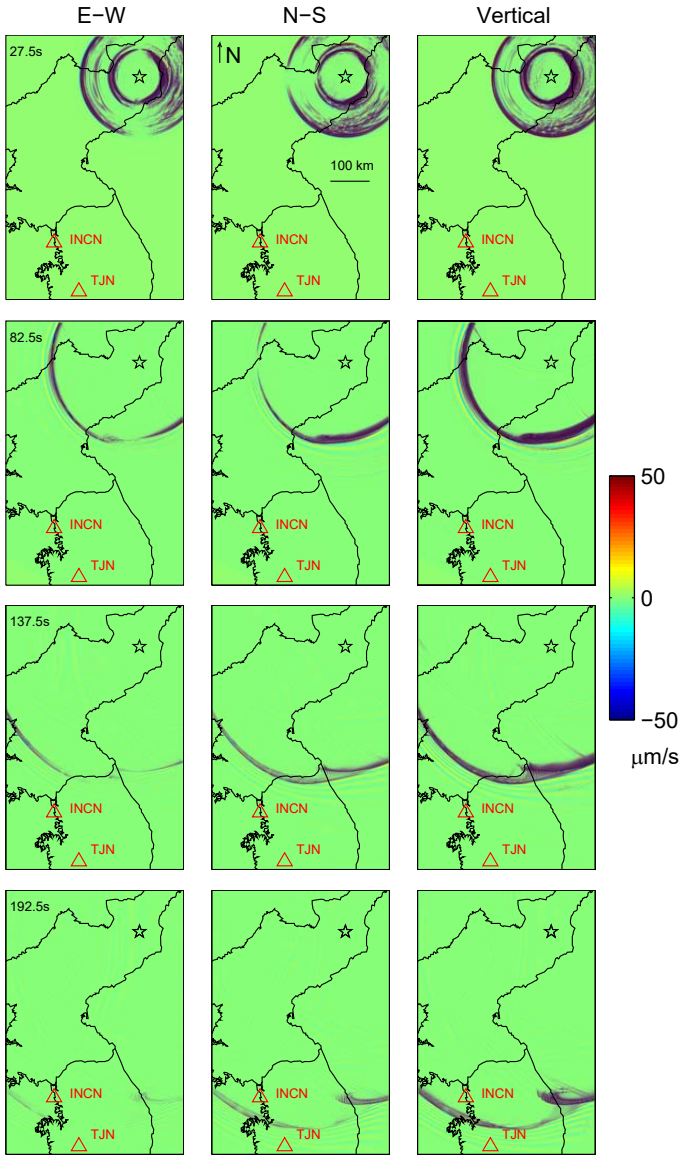

Figure 2. Snapshots of Wave Propagation (< 4 Hz) in SALSA3D (Model 1, Table 1)

Table 1. Q(f) and Small-scale Heterogeneity Parameters for FD Models*

Model	a (m)	R (km)	σ (%) $d<d_1$	d_1(km)	σ (%) $d>d_2$	d_2(km)	H/V	Seed	Q_o	γ
1	-	-	-	-	-	-	-	-	350	0.3
2	1,000	5	5	-	5	-	5	1	350	0.3
3	1,000	5	10	-	10	-	5	1	350	0.3
4	150	5	10	-	10	-	5	1	350	0.3
5	1,000	5	10	-	10	-	5	1	200	0.3
6	1,000	5	10	10	2	12.5	5	1	200	0.3
6a	1,000	0	10	10	0	12.5	5	1	200	0.3
7	1,000	0	10	7.5	2	10	5	1	200	0.3
7a	1,000	0	10	7.5	0	10	5	1	200	0.3
8	1,000	5	10	5	2	5	5	1	200	0.3
9	1,000	5	10	2.5	2	2.5	5	1	200	0.3
10	1,000	5	10	10	2	12.5	1	1	200	0.3
11	1,000	5	10	10	2	12.5	7	1	200	0.3
12	1,000	5	10	10	2	12.5	10	1	200	0.3
13	150	0	10	10	0	12.5	5	1	200	0.3
14	2,000	0	10	10	0	12.5	5	1	200	0.3
15	3,000	0	10	10	0	12.5	5	1	200	0.3
16	1,000	0.5	10	10	0	12.5	5	1	200	0.3
17	1,000	0.5	10	10	0	12.5	5	2	200	0.3
18	1,000	0.5	10	10	0	12.5	5	4	200	0.3
19	1,000	0.5	10	10	0	12.5	5	5	200	0.3
20	1,000	0.5	10	10	0	12.5	5	6	200	0.3

*All models use ν=0.1

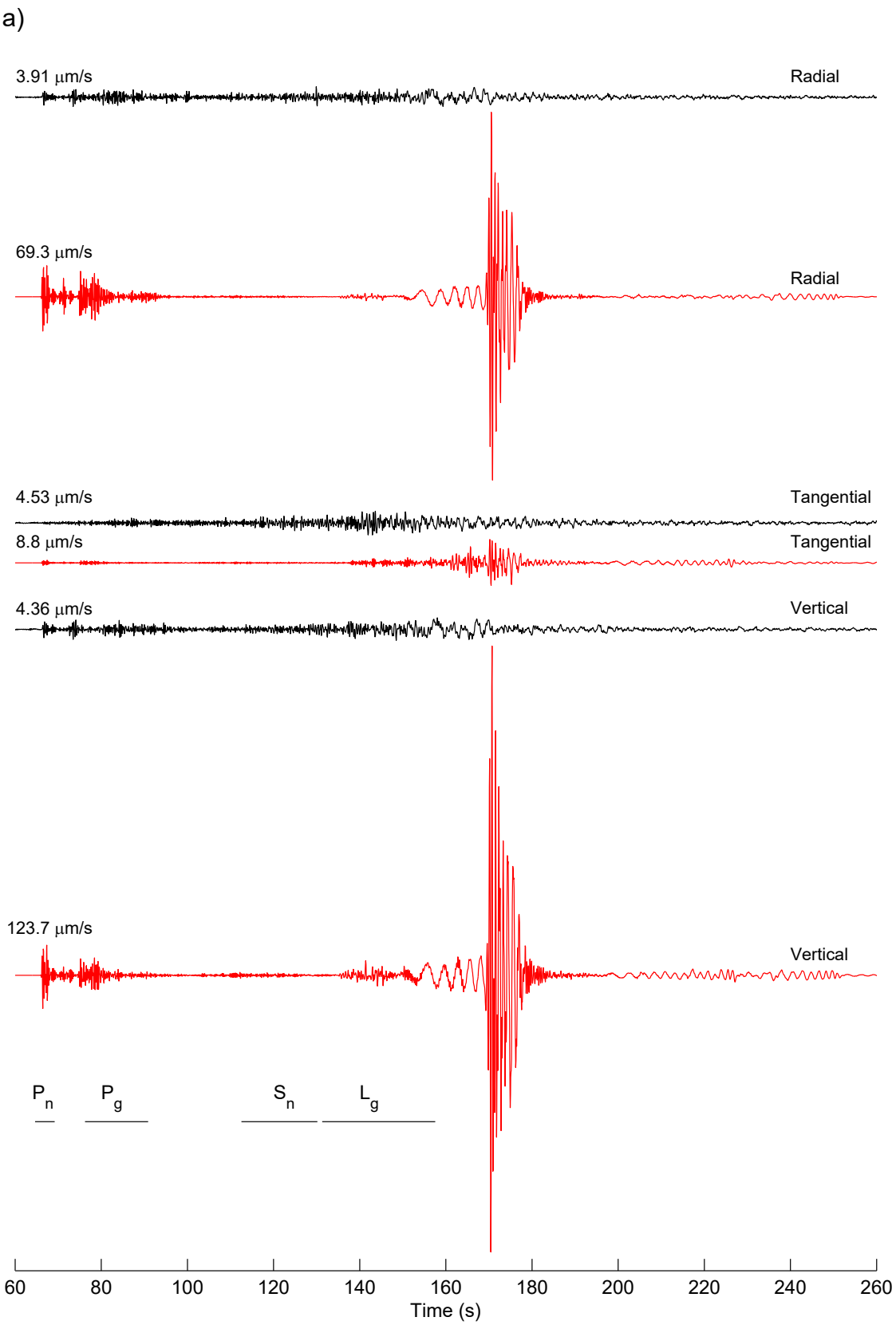

Figure 3. Comparison of Observed (Black) and Synthetic Waveforms at INCN for the SALSA3D Model with Small-scale Heterogeneities (Model 1, Table 1) in (a) Time and (b) Frequency Domains

b)

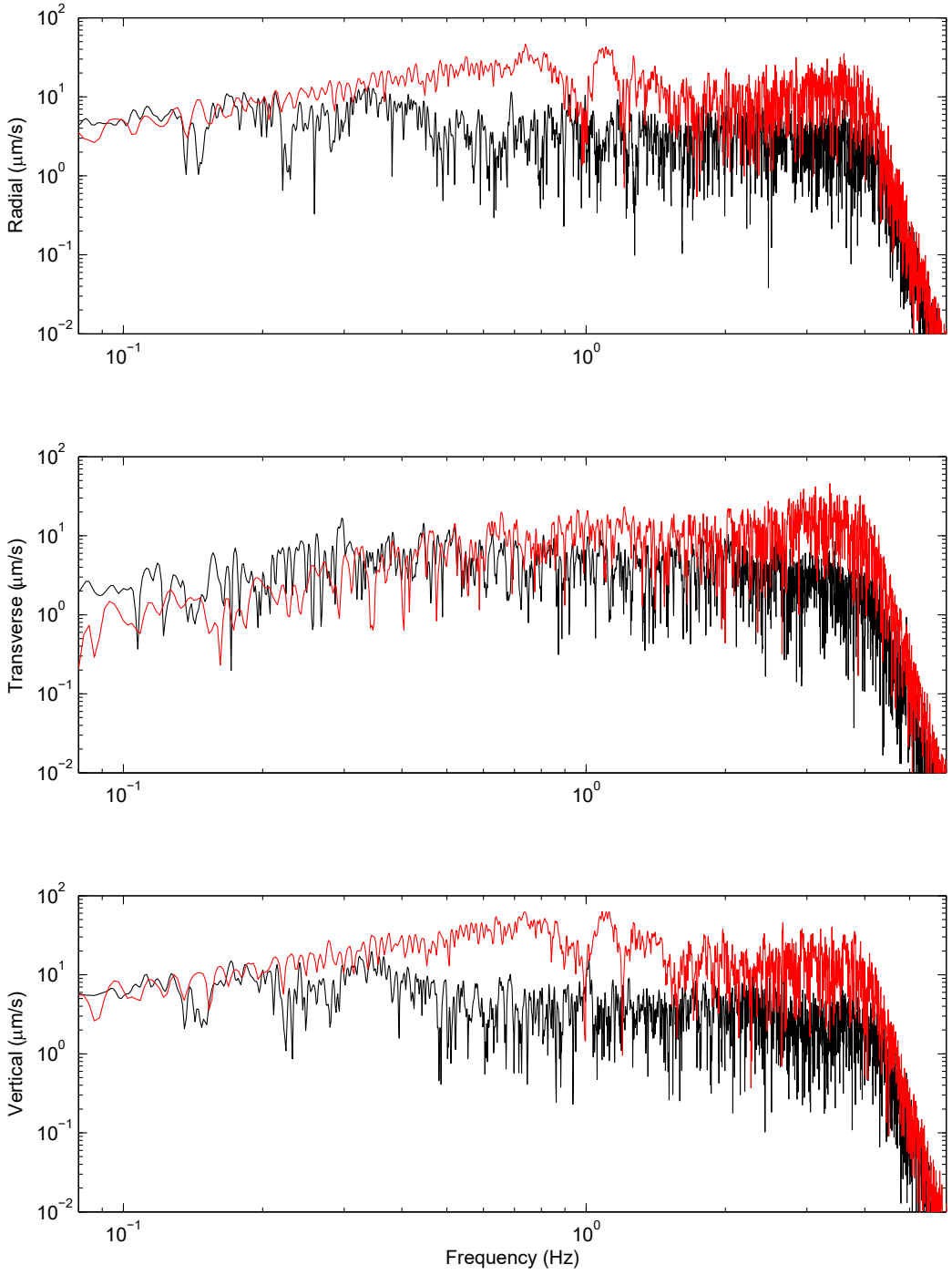

Figure 3. (Cont.) Comparison of Observed (Black) and Synthetic Waveforms at INCN for the SALSA3D Model with Small-scale Heterogeneities (Model 1, Table 1) in (a) Time and (b) Frequency Domains

4.2 Small-Scale Media Heterogeneities

4.2.1 Statistical Description

Small-scale heterogeneities can be described statistically, for example using von Karman auto covariance functions shown in eq. 5 with Fourier transform in eq. 6,

$$\Phi_{v,L}(r) = \sigma^2 \frac{2^{1-v}}{\Gamma(v)} \left(\frac{r}{a} \right)^v K_v \left(\frac{r}{a} \right) \tag{5}$$

$$P(k) = \frac{\sigma^2 (2\sqrt{\pi} a)^E \Gamma(v + E/2)}{\Gamma(v)(1 + k^2 a^2)^{v+E/2}} , \tag{6}$$

or using other statistical descriptions (e.g., Gaussian or Exponential distributions, see for example, Frankel and Clayton, 1986). Constraints on the parameters of the statistical distributions - the correlation length, *a,* Hurst exponent, ν, and standard deviation, σ - can be obtained from sonic logs, digitized geological maps and V_s30 measurements (e.g., Wu et al., 1994; Levander et al., 1994; De et al., 1994; Holliger, 1996; Holliger, 1997; Dolan et al., 1998; Nakata and Beroza, 2015; Savran and Olsen, 2016). These studies report Hurst exponents of 0.0-0.3 and correlation lengths between 60-160 m in the vertical direction, and horizontal to vertical anisotropy (H/V) between ~2-25. There is considerable variation in the correlation lengths found among the studies, reflecting the variable constraints from the underlying data (e.g., teleseismics may favor longer correlation lengths as compared to data from near-field stations). Moreover, the results from analysis of detailed sonic logs with sample spacings < 1 m are prone to produce smaller (high frequency) values than those from much more coarsely distributed measurements (such as V_s30).

Other constraints on the parameters of the small-scale heterogeneities are obtained from applying the statistical distributions in wave propagation simulations. Frankel and Clayton (1986) generated small-scale heterogeneities with three distinct autocorrelation functions, Gaussian, exponential (corresponding to ν = 0.5), and self-similar (corresponding to a ν = 0.0). By testing end-member cases of the von Karman autocorrelation function their 2D simulations provided constraints on ν estimates for the small-scale heterogeneities that fall in the range [0.0, 0.5] with a preferred value of 0.0. Hartzell et al. (2010) used ν=0.0 with *a*=5-10 km and σ=5-10%, while Jacobsen and Olsen (2011) included statistical distributions with ν=[-0.5-0.5], *a*=250 m and σ=5-10% in their simulations. Imperatori and Mai (2013) used a Hurst exponent of 0.3 with correlation lengths on the order of hundreds of meters to kilometers.

Using a von Karman model we have generated distributions of small-scale heterogeneities with parameters based on the published studies discussed above, and added the result to the SALSA3D model. Figure 1 (right) shows horizontal and vertical slices of V_s, where *a*=1000 m, ν=0.1, σ=10%, H/V=5 (Model 2, see Table 1). In the

following we use trial-and-error modeling to constrain the parameters of the statistical parameters of the von Karman and anelastic parameters generating synthetics with the best fit to data. In the series of tests concerning a particular parameter, all other parameters are kept constant.

4.2.2 Scattering Effects from Depth-independent Models.

Figures 4 (INCN) and A3 (TJN) show a comparison of data and simulations including a von Karman model with models 2-5, see Table 1. The small-scale heterogeneities are added to the entire depth extent of the reference model, and we use γ=0.3 for the frequency-dependent power-law exponent. Compared to Model 1 without small-scale heterogeneities, Model 2 with σ = 5% and Q_o=350 still produces a coherent Rayleigh wave, albeit with reduced amplitude, and the amplitudes between the P wave and surface waves and coda following the surface waves continue to be larger than that for the data. When σ is increased to 10% throughout the model (Model 3), the surface wave amplitudes are further reduced, the amplitudes between the P wave and surface waves are now similar to or smaller than those for the data, and the coda amplitude after the surface waves is increased from the 5% case (Model 2). Model 3 generates synthetics with coda amplitudes similar to data at TJN, but tends to overpredict those at INCN.

The Hurst number of the small-scale heterogeneities in models 2-5 (ν=0.1) was selected in agreement with the variogram analysis of borehole sonic logs from the Los Angeles basin (Savran and Olsen, 2016). This analysis also found vertical correlation logs of 50-150 m, much shorter than the a=1,000 m used in Models 2-3. However, it is clear from Model 4, using a=150m and σ =10%, that the shorter correlation length, while reducing the higher-frequency amplitudes in the synthetics, still produces Rayleigh Wave amplitudes much larger than those in the data. Thus, varying the parameters of the small-scale heterogeneities does not appear to produce a satisfactory fit of the synthetics to the data. Instead, a lower Q_o of 200 with a=1,000 m and σ =10% (Model 5) produces synthetics with closer match to the data at INCN, but generally underpredicting the data at TJN. This result suggests that the path from the NKNTS to TJN is characterized by somewhat smaller low-frequency attenuation (Q_o~350) than that to INCN (Q_o~200).

Probably the most pronounced effect of Models 2-5 on the synthetics is the reduction of the P_n amplitude to values much below those for the data. We examine in the following section whether this issue can be overcome using a depth dependency of σ.

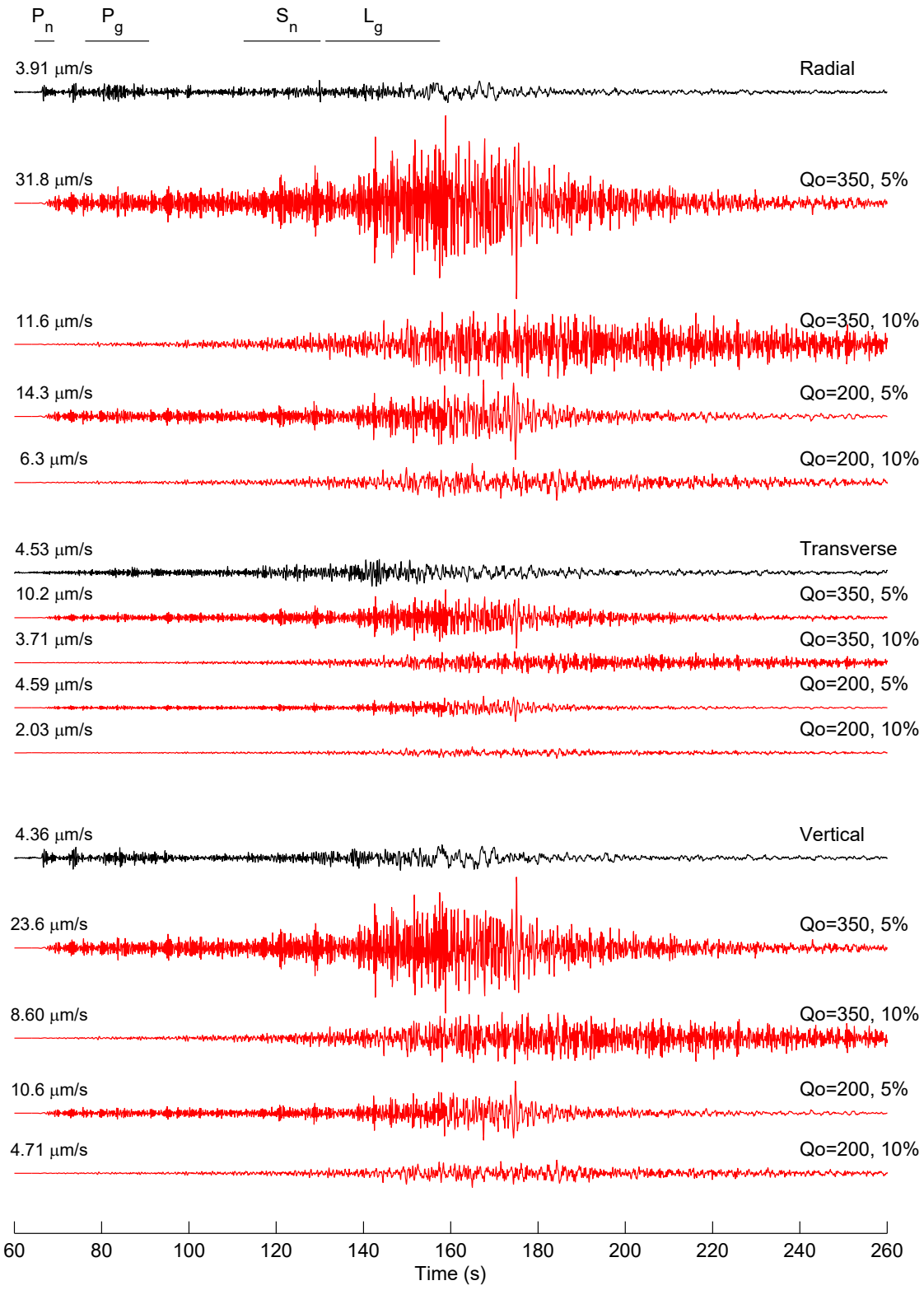

Figure 4. Comparison of Observed (black) and Synthetic Waveforms at INCN for the SALSA3D Model with Models 2-5 (Table 1)

4.2.3 Scattering Effects from Depth-dependent Models.

It is likely that the strength of the small-scale heterogeneities decreases with depth, for example due to the associated increase in lithostatic pressure and ductility of crustal material at deeper depths. To test such depth dependency of the scattering we have simulated wave propagation in 4 different gradient models of von Karman statistical distributions of small-scale heterogeneities (Figs. 5, INCN, and A4, TJN, Models 6-9 in Table 1). The gradient models are all characterized by $\sigma = 10\%$ from the surface to a depth of d_1 (km), $\sigma = 2\%$ below a depth of d_2 (km), and a linear gradient in between. The values of d_1 and d_2 are listed by the synthetics. Here, we choose to use the relation $Q(f)=200\ f^{0.3}$ which produced an optimal fit for INCN using Model 5.

It is clear from Figs. 5 and A4 that the decrease in strength of the small-scale heterogeneities with depth in the upper crust improves the fit between the data and synthetics by generating larger amplitude initial P waves, and improving the amplitude of converted phases between the P and surface arrivals. Models 6-7 are selected for further analysis in the following sections based on their favorable fit to the data.

The scattering originating from the deeper parts of the model is further illustrated in Figs. 6 (INCN) and A5 (TJN), where the effects of the scattering from models with $\sigma = 0\%$ and 2% below the lower threshold depth (d_2) in the gradient models of Figs. 5 and A4 are highlighted. The results show that even a small value of σ of 2% below d_2 can have a significant effect on the wave train, including the first arriving P phases. Specifically, the gradient model with $\sigma = 2\%$ generates a gradual onset of P_n over 1-2 seconds, affecting the initial amplitude. On the other hand, if small-scale heterogeneities are omitted below d_2, the arrival time and amplitude of the P_n amplitudes are more impulsive. This result can have implications for techniques discriminating between explosive and earthquake sources based on ratios of P and S wave amplitudes. The modeling effects of the small-scale heterogeneities thus suggest that the scattering strength in the Earth's lower crust and the upper mantle strongly controls the amplitude and character of the initial P waves.

4.2.4 Constraints on Anisotropy of the Small-scale Crustal and Mantle Heterogeneities.

Several studies have estimated the horizontal-to-vertical anisotropy (H/V) of the small-scale heterogeneities in the crust from statistical analyses (e.g., Nakata and Beroza, 2015, using random-field model representations of a 3-D *P*-wave velocity model at Long Beach, CA, finding H/V~5). While these H/V measurements are based on analysis of representations of the crustal structure we here constrain the anisotropy from modeling regional wave propagation from the NKNTS to stations INCN and TJN. Figures 7 (INCN) and A6 (TJN) show waveform comparisons for the gradient model of small-scale heterogeneities with $\sigma = 10\%$ from the surface to a depth of 10 km, $\sigma = 2\%$ below a depth of 12.5 km, with H/V =1, 5, 7, 10 (Models 6, 10-12, Table 1). The model with no anisotropy (H/V=1) generates a Rayleigh wave deficient in higher frequencies and with larger amplitude than observed in the data. The Rayleigh wave for H/V values of 7 and 10, while limited to a narrower time window, also overpredicts the amplitude of the phase in the data. The (high-frequency) energy associated with the P_n phases for the simulations with H/V = 1, 7, and 10 are larger than that for the data, in particular for H/V=7. The

value of H/V that generates the synthetics in best agreement with data for both initial P waves and surface waves, is 5, in agreement with the results by Nakata and Beroza (2015).

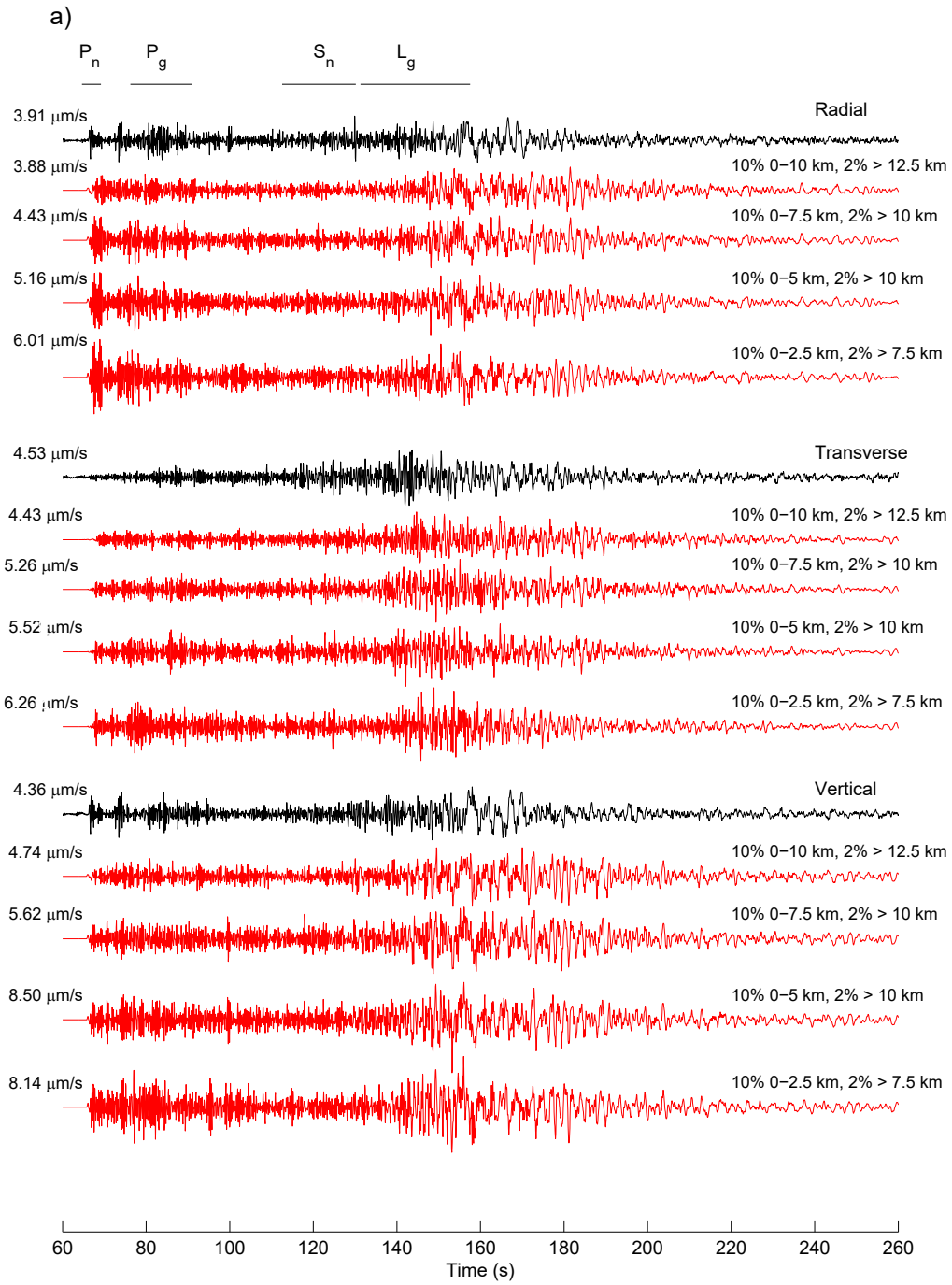

Figure 5. (top) Comparison of Observed (Black) and Synthetic (red) Waveforms at INCN for Models 6-9 (Table 1). ***The Gradient Models are all Characterized by s = 10% From the Surface to a Depth of d1 km, s = 2% Below a Depth of d2 km, and a Linear Gradient in Between. The Values of d1 and d2 are Listed by the Synthetics.*** **The Bottom Figure Shows the Comparison in the Frequency Domain for Model 6 (Table 1)**

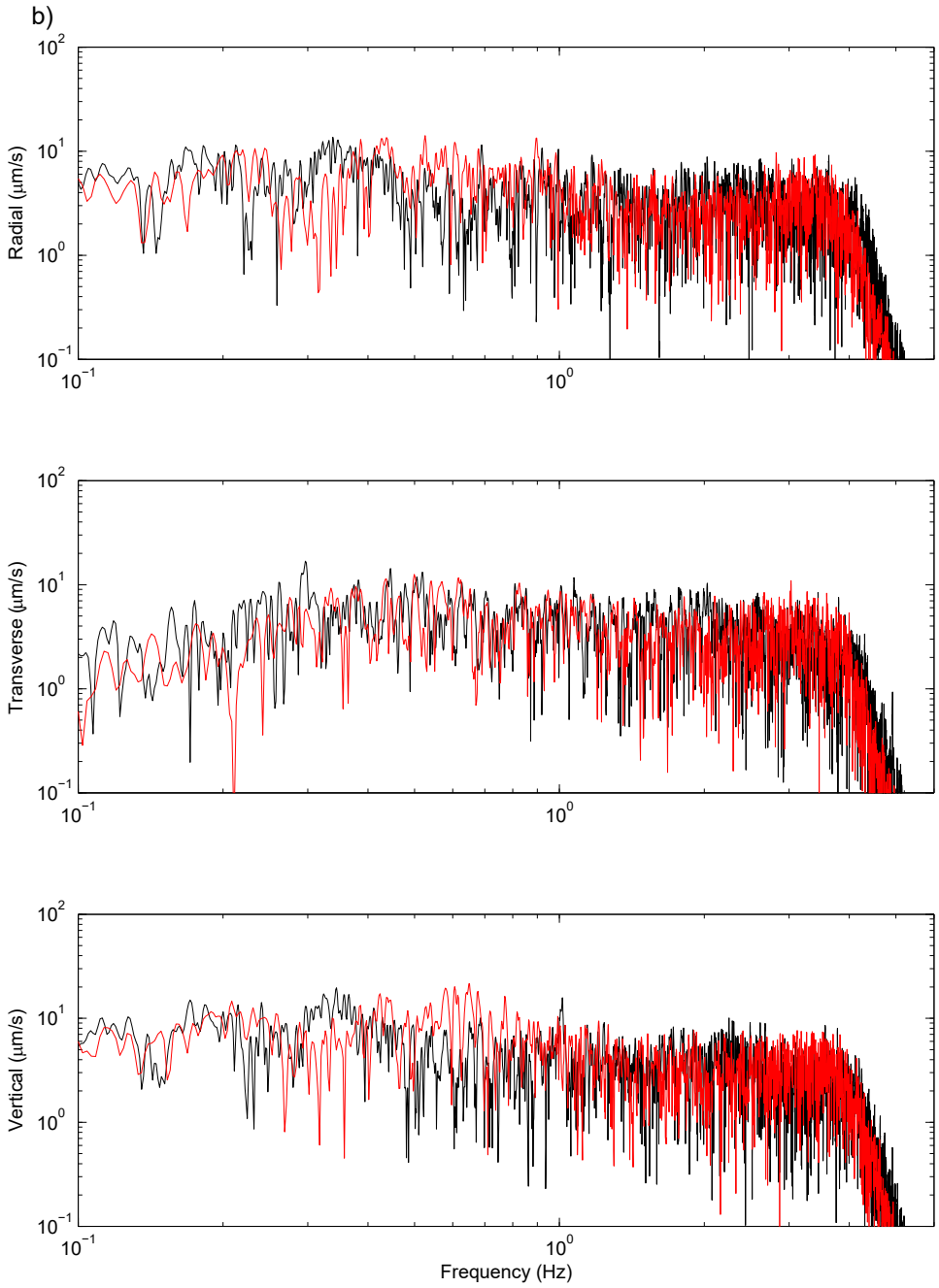

Figure 5. (cont.) (top) Comparison of Observed (Black) and Synthetic (red) Waveforms at INCN for Models 6-9 (Table 1). ***The Gradient Models are all Characterized by σ = 10% From the Surface to a Depth of d_1 km, σ = 2% Below a Depth of d_2 km, and a Linear Gradient in Between. The Values of d_1 and d_2 are Listed by the Synthetics.*** **The Bottom Figure Shows the Comparison in the Frequency Domain for Model 6 (Table 1)**

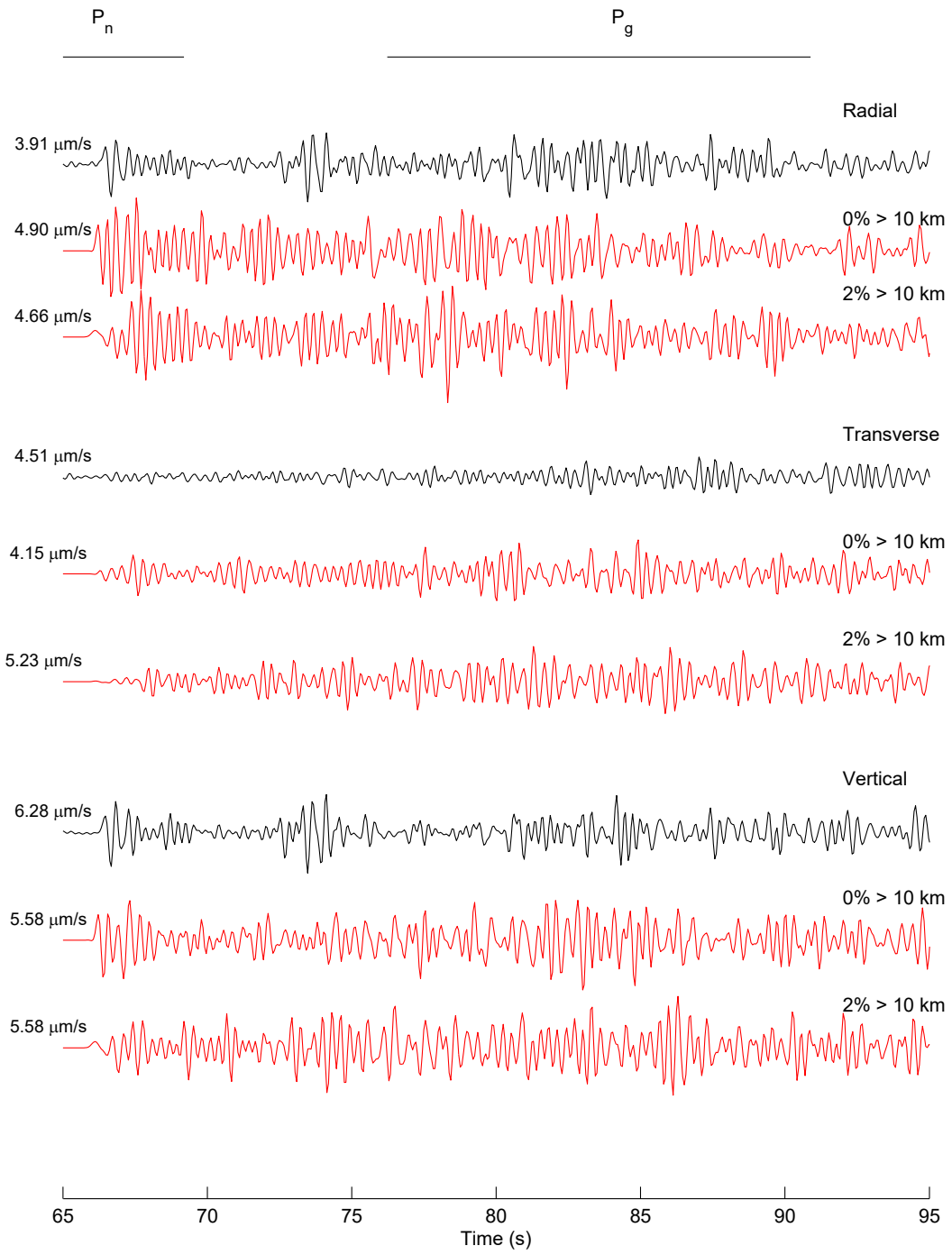

Figure 6. Zoom of the Time Domain Comparison for INCN Using Models 7 and 7a (Table 1). ***Peak Velocities Listed Refer to the Time Interval Shown***

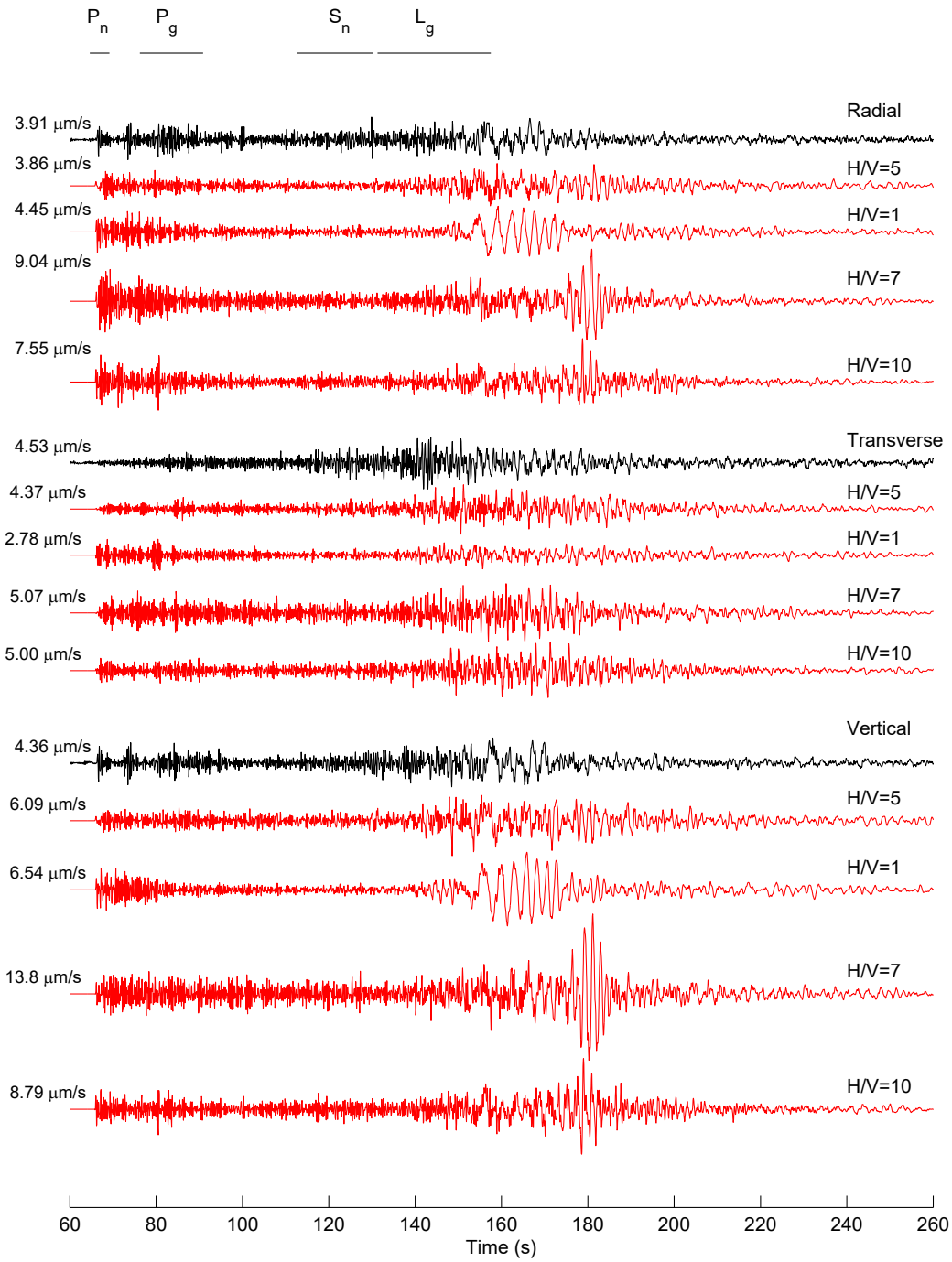

Figure 7. Comparison at INCN of the Scattering Effects From Anisotropy in the Small-scale Heterogeneities, Quantified by the Ratio of Horizontal-to-vertical Dimensions of the Velocity and Density Perturbations (H/V). Results for H/V=1, 5, 7, and 10 (Models10, 6, 11 and 12, Table 1) are Shown

4.2.5 Constraints on Correlation Length of the Small-scale Crustal and Mantle Heterogeneities.

Previous modeling studies that have included statistical models of small-scale heterogeneities have considered a tremendous range of correlation lengths for the velocity perturbations, from tens of meters to 10 km (see section **3.6.1**). Here, we test whether an optimal value for the correlation length of the crust and mantle between the NKNTS and INCN and TJN can be found, in terms of the match between data and synthetics at the two stations. Figures 8 and A7 show the waveform fits at INCN and TJN, respectively, for Q(f), ν, and σ of Model 6, and correlation length of 150 m, 1,000 m, 2,000 m, and 3,000 m (Models 13, 6, 14 and 15, Table 1). The synthetics for a = 150 m, 2,000 m and 3,000 m tend to generate large-amplitude Rayleigh waves (~160-180 s at INCN, ~200-230 s at TJN), with similarity to those obtained in Model 1 without small-scale heterogeneities (Fig. 3). On the other hand, the synthetics obtained from the model with a = 1,000 m (Model 6) generally resembles the waveform characteristics of the data, with much smaller Rayleigh-wave amplitudes, as compared to those from the models with shorter and longer values of a. Based on this result, we adopt a value of 1,000 m as an average correlation length for the path between the NKNTS and the western North Korean Peninsula.

4.2.6 Near-source Scattering and Generation of S-wave Energy.

An explosive source with limited tectonic release and other near-source effects primarily generates compressional seismic energy (e.g., Ford et al., 2009; Shin et al., 2010). However, records from explosive sources at regional distances often contain considerable S-wave energy (as is the case for the observed transverse component at INCN and TJN in our models). Our simulations have shown that crustal and mantle scattering processes from small-scale heterogeneities can explain almost all of the S-wave and Love wave energy, e.g., the main phases on the transverse component. The FD modeling technique allows us to investigate which fraction of the S-wave energy is generated in the near-source region.

Toward this goal, Figures 9 (INCN) and A8 (TJN) compare synthetics with small-scale heterogeneities added with the gradient from Model 6 (Table 1), where the small-scale heterogeneities are omitted within a spherical volume with radii of 0, 1, 5 and 10 km. At a first glance, the synthetics for the four different models are very similar, in both amplitude and general characteristics of the phases. The synthetics for the model with R=0 km are visually almost identical to those with R = 1 and 5 km, while smaller variations in phase and a slight decrease in peak amplitude start to appear in the synthetics for R = 10. These results apply to all three components, including the transverse component, with predominantly S-wave energy and where the contribution from an isotropic source is expected to be minimal. Thus, Figures 9 and A8 suggest that scattering within a narrow region around the source contributes negligibly to the S-wave energy recorded at INCN and TJN.

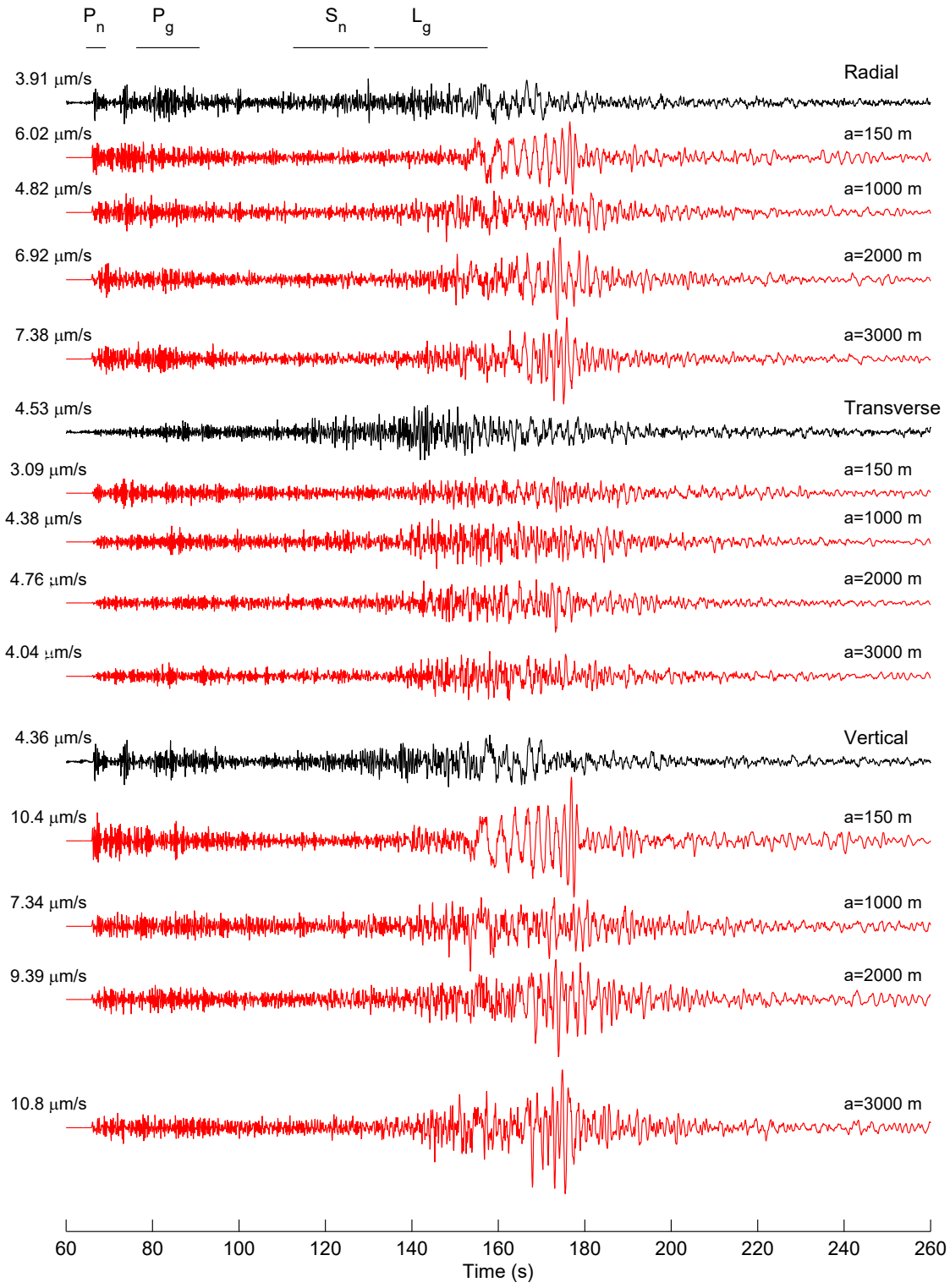

Figure 8. Comparison at INCN of the Scattering Effects From Different Correlation Length in the Distribution of Small-scale Heterogeneities (150 m, 1,000 m, 2,000 m, and 3,000 m) as Defined by Models 13, 6a, 14 and 15 (Table 1)

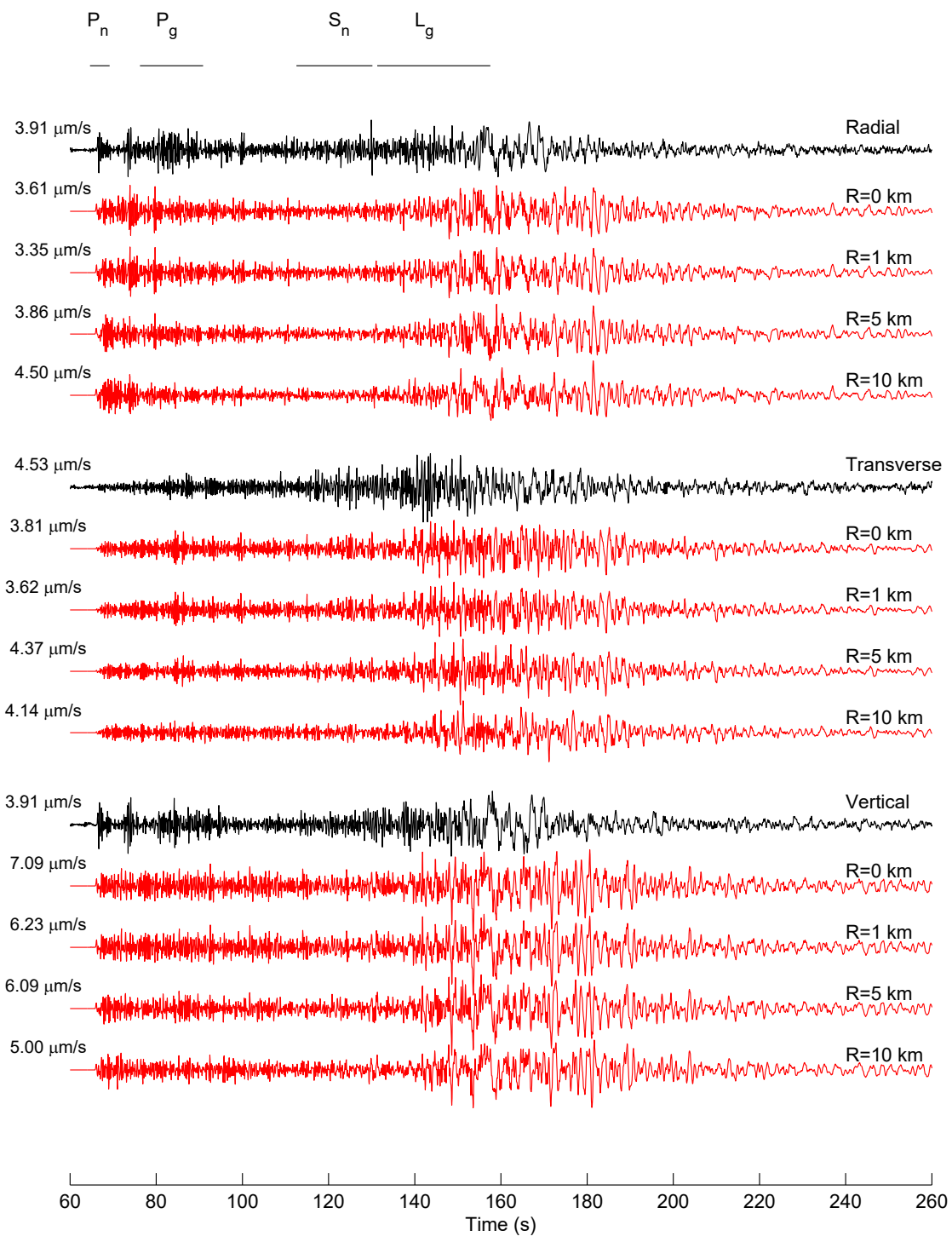

Figure 9. Significance of Near-source Scattering Effects From Small-scale Heterogeneities at INCN. The Statistical Model (6, Table 1) has Been Removed Within Radii (R) of 0-10 km From the Source, Listed by the Synthetics

Figure 10 shows snapshots of velocity wave propagation in Model 6 (Table 1). The contrast of the wavefield in Figure 10 compared to that in Figure 3 is striking, primarily due to the amount of crustal scattering generated by the small-scale heterogeneities. At 27.5s, P-to-S and P-to-P scattering dominates the area between the P waves and surface waves. The surface waves, characterized by large-amplitude coherent wave trains in the model without small-scale heterogeneities (Fig. 3), appear as a 100 km+ wide band of scattered energy at 82.5s. Here, the amplitudes diminish away from a central high, indicating the presence of both forward and backward scattering. At later times (82.5 s and 137.5 s), the largest scattered surface waves occur offshore east for the Korean Peninsula in the lower velocity material.

The stochastic nature of the velocity and density perturbations in the underlying crustal and mantle structure allows us to model the statistics of the resulting synthetics, while the details of the individual phases and coda depends on the realization of the specific distribution of small-scale heterogeneities. For this reason, an infinite set of ground motion synthetics can be derived from a given set of von Karman parameters. To estimate the range of ground motions to be expected from the possible realizations associated with the statistical distributions generated in this study, Figures 11 (INCN) and A9 (TJN) compare synthetics for 5 realizations the same gradient model of small-scale heterogeneities (Models 16-20, Table 1). As expected, the general characteristics including arrival times and amplitude of the simulated waveforms discussed in this article persist among the realizations. For example, the variation of the peak amplitude among the 5 realizations is less than 65%. It is interesting to note, however, that the amplitude of the individual phases can vary by a much larger amount. This result suggests that it is necessary to use an ensemble of simulations generated from different realizations of von Karman distributions of small-scale heterogeneities, in particular for applications depending specifically on P and S amplitudes, such as source discrimination.

Baker et al. (2012) reviewed the various mechanisms published for generating S wave energy from shallow explosions in relatively high-velocity crust (such as the crust between the NKNTS and INCN and TJN). This review concluded that the majority of the S energy is generated by the non-spherical component of the source volume, as opposed to regional scattering. Pitarka et al. (2015) used 0-10 Hz numerical simulations and data from the Source Physics Experiment (SPE) at the Nevada National Security site to analyze the generation of S wave energy at very-near source distances (<1 km). They found that a large part of the S wave energy present in the simulations were generated near the source. Further analysis is needed to explain the reasons for the different conclusions related to near-source S wave generation obtained here.

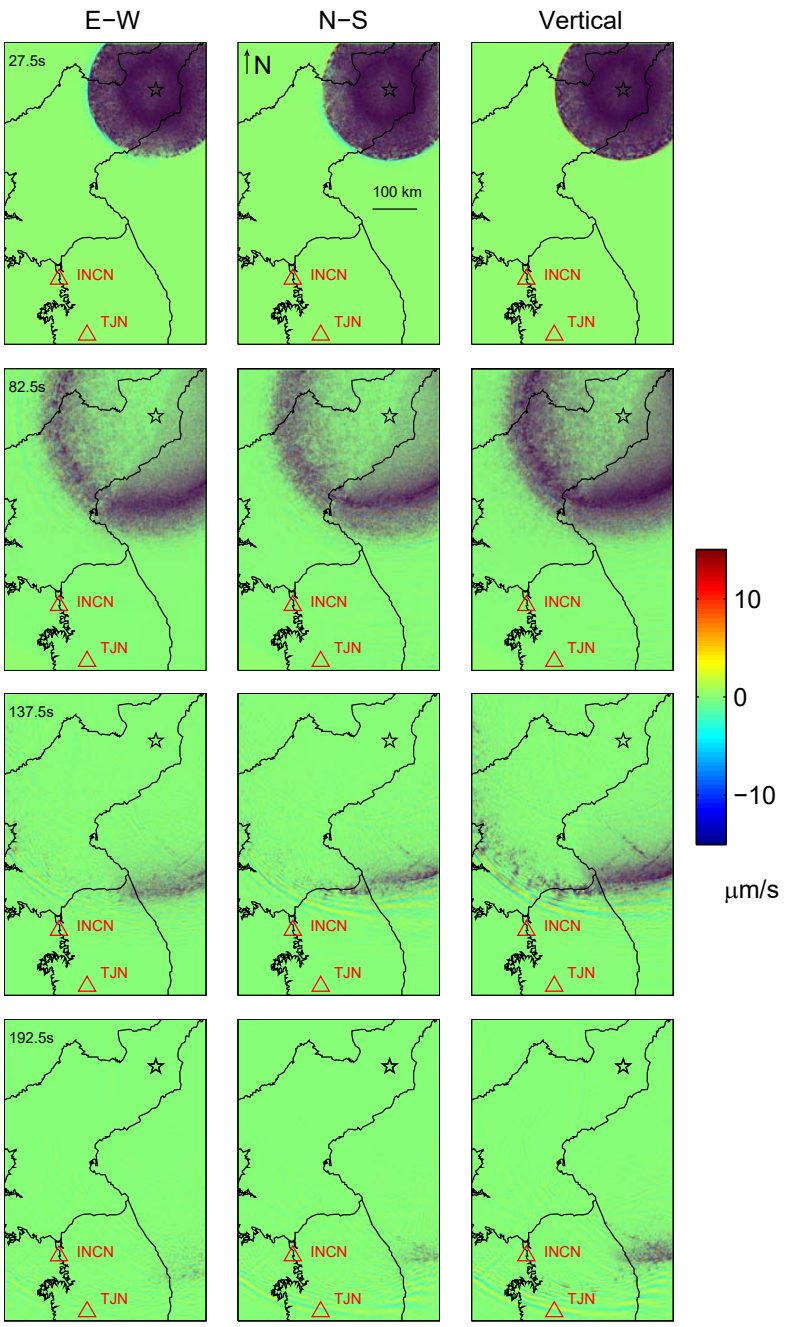

Figure 10. Snapshots of Wave Propagation for Model 6 (Table 1)

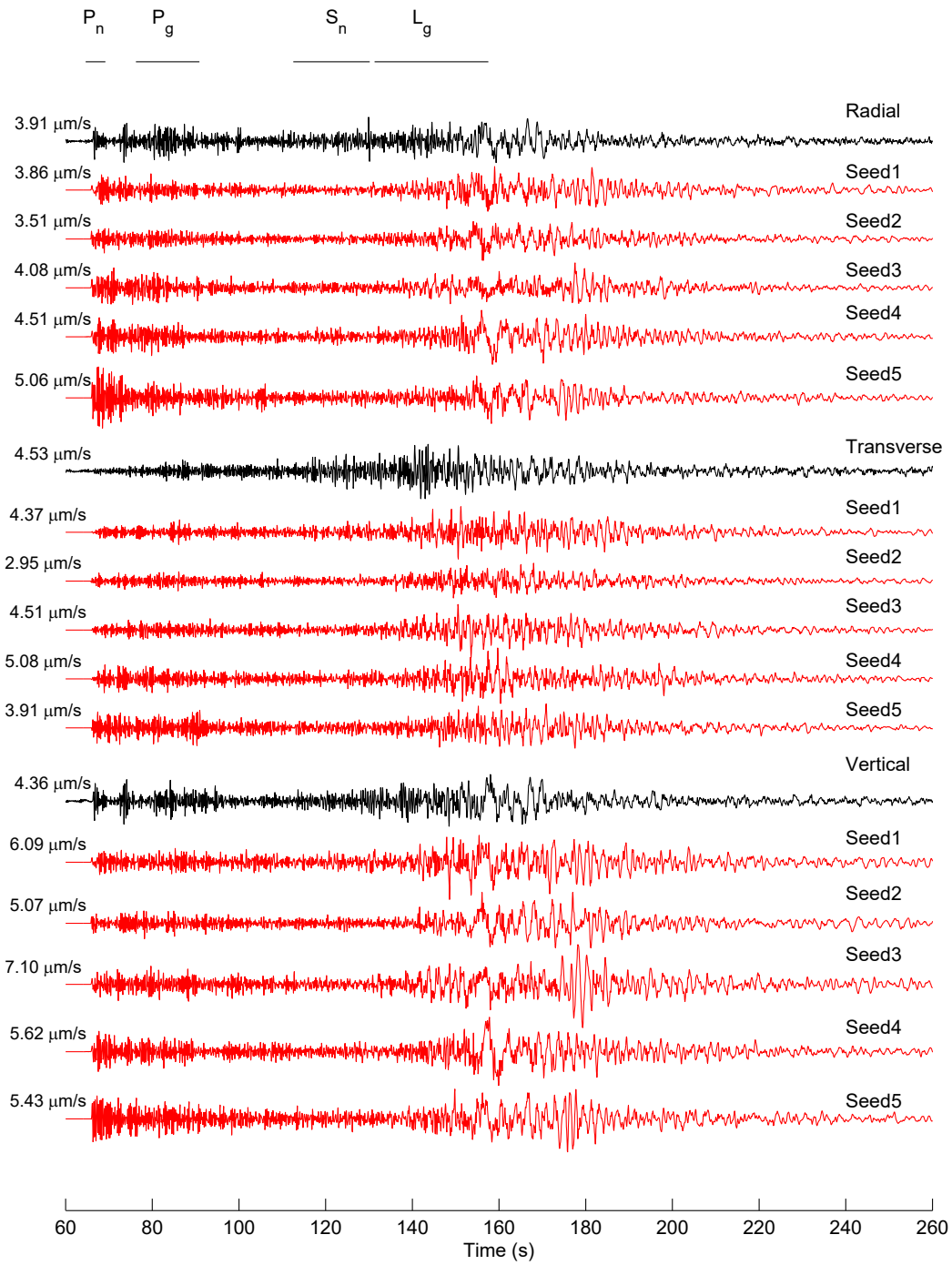

Figure 11. Comparison of Data to Synthetics Generated From a 5-realization Ensemble of Statistical Models of Small-scale Heterogeneities With Different Seed Numbers at INCN. All Simulations use the Q(f), a, H/V and σ of Models 16-20 (Table 1)

4.2.7 Wave Propagation for Isotropic Versus Inverted Moment Tensor Source

Chiang et al. (2018) published inversion results for all North Korean nuclear explosions using consistent methodology and data records. The seismic moment of the 2009 event from Chiang et al. (2018) (1.83e15 Nm) is very close to that estimated by Ford et al. (2009) (1.8e15 Nm), who inverted assuming an isotropic moment tensor. However, the moment tensor from Chiang et al. (2018) has a 20% non-isotropic component. The inclusion of the deviatoric part of the moment tensor considers the excitation of S-waves at the source region, in addition to that generated from scattering.

Figure 12 compares the long-period synthetic waveforms from the isotropic and Chiang et al. (2018) moment tensor sources, in the SALSA3D model (Begnaud, 2015) without small-scale heterogeneities, to the observations at INCN for the 2009 NK nuclear test. The fit for the two sets of synthetics is comparable, except for improved match of the primary arrival on the transverse component (~140 s) for the 20% non-isotropic source.

Figure 13 shows a comparison of a 5-realization ensemble of 0-4 Hz simulations using the favored model of small-scale heterogeneities (model 7a, Table 1), as compared to data for the 2009 NK nuclear test at INCN. While the ensemble shows strong variation of phase amplitudes, no significant improvement in the fit of the envelope to the data is obtained (compare to Figure 11 for the 5-realization ensemble for the isotropic source). The broadband coda envelope on the transverse component generated by both isotropic and Chiang et al. (2018) moment tensor sources are smaller than those for the data, indicating that the non-isotropic part of the source has limited effect on the generation of Sn amplitudes.

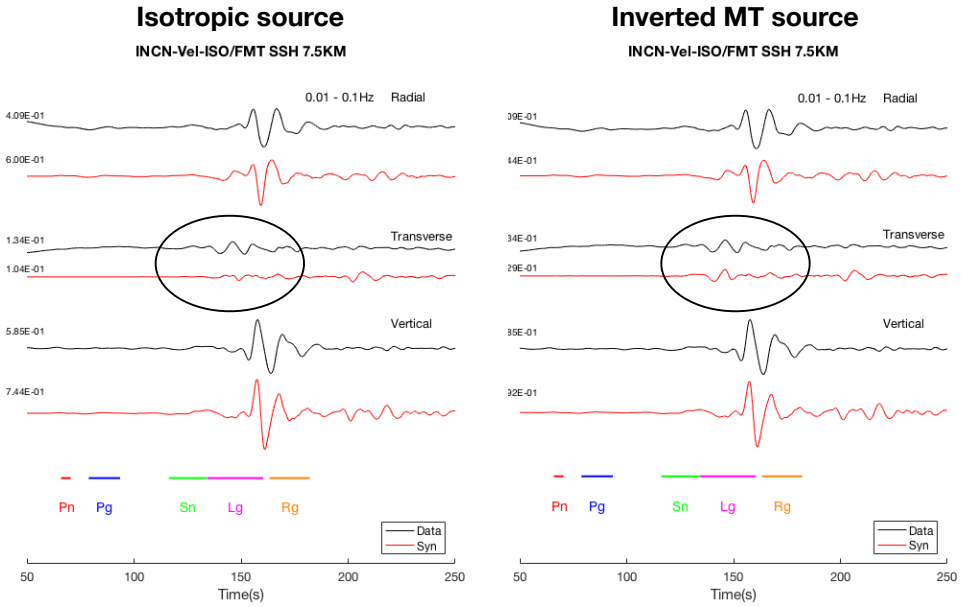

Figure 12. Comparison of Long-period (0.01-0.1 Hz) Synthetics for (Left) an Isotropic and (Right) a 20% Non-isotropic Source (Chiang et al., 2018) at INCN. ***The Oval Depicts the Primary Improvement in the Fit to Data Using the Inverted Source over the Isotropic Source on the Transverse Component***

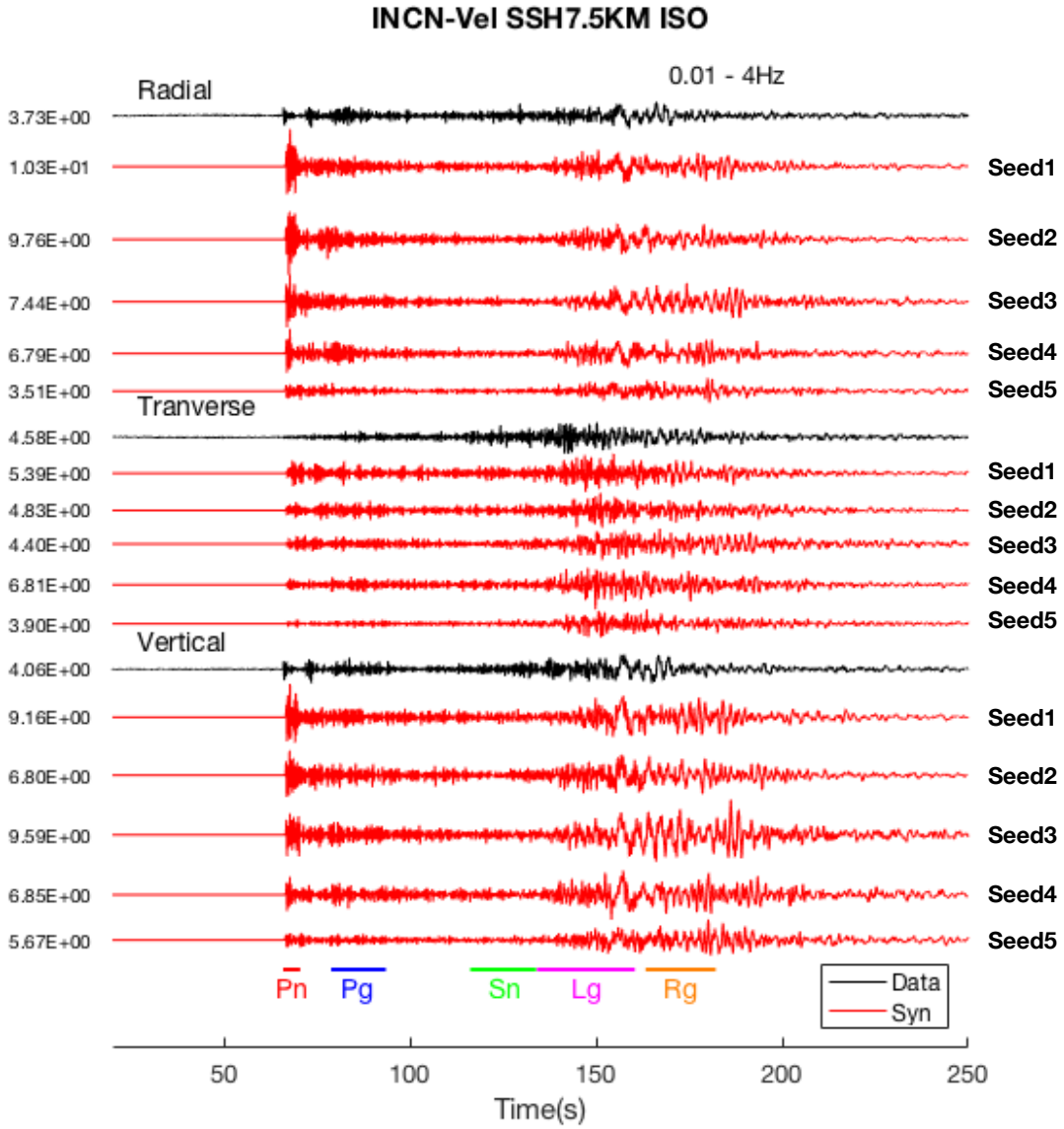

Figure 13. Comparison of Observed (Black) and 5-Realization Ensemble of Synthetic Waveforms (Red) Computed with the Inverted Moment Tensor Source by Chiang et al. (2018), in the SALSA3D Model Including a Distribution of Small-scale Heterogeneities Providing Optimal Fits to Data in our Previous work (model 7a, Table 1)

4.2.8 Discussion

Topographic scattering was omitted in the simulations carried out in our study, and thus was not necessary to obtain the waveform fits presented here. However, Rodgers et al. (2010) found that topographic scattering can have significant effects on the resulting wavefield, including enhancement of energy propagation near the source, surface wave

amplification, and SV and SH-wave polarization simulated for 0-8 Hz wave propagation from the 2006 and 2009 North Korean nuclear tests. Their simulations using different proposed locations of the sources a few kilometers apart generated significantly different wavefields due to the variation-specific source-coupling with local topography. Unfortunately, no observations were available within their 40 km x 40 km region for comparison. The largest topographic scattering effects were generated for frequencies larger than the 4 Hz used in our study. On the other hand, Takemura et al. (2015) used 3D 0-4 Hz FD simulations including both surface topography and small-scale heterogeneities to distances of 80 km from explosive and earthquake sources (buried 5 km, somewhat deeper than the our shallow sources). They found, in general agreement with our results, that the primary source of scattered energy was small-scale heterogeneities in the crust, while the cumulative effect of surface topography is limited over long distances. Future studies should further delineate the relative contributions of small-scale heterogeneities and surface topography on seismic waveforms for regional propagation distances.

We found that a vertical correlation length of 1,000 m represented an optimal value based on trial-and-error tests within a range of 150-3,000 m. Our preferred value of a=1,000 m is longer than that estimated from sonic logs by Savran and Olsen (2016) (<150 m). However, the efficacy of the longer correlation length in reproducing the INCN and TJN waveforms is not too surprising, as the detailed sonic logs with sample spacings < 1 m may be biased toward smaller (high frequency) correlation lengths, and the rather smooth SALSA3D is deficient in most length scales less than ~10 kilometer or more.

In order to reach a maximum frequency of 4 Hz for the simulations in this study (with a minimum of 6.25 points per minimum S-wave length), we have limited the minimum V_s in the crustal models to 2,500 m/s. This artificial constraint is implemented at a grid point by resetting V_s to 2,500 m/s, and replacing V_p by 2,500 m/s times the V_p/V_s ratio at the grid point. This modification has little effect within the N-S oriented band within the Korean peninsula where V_s^{min} is already near 3,100 m/s (see Fig. A10), in the general path between the NKNTS and western South Korea. However, the upper ~3.1 km of the continental shelf to the east of this band has V_s as low as 969 m/s, and may need to be included when modeling data further east.

The accuracy of the attenuation and scattering parameters on the Korean Peninsula estimated in this study relies on an estimate of the magnitude of the 2009 NKNTS explosion. We have estimated the moment of our isotropic source function by comparing the low-frequency spectral amplitude for synthetics and data at INCN and TJN ($1.58e^{15}$ Nm, M_w=4.1), as well as long-period waveform comparisons (Fig. 12). This estimate of the source magnitude is in agreement with Ford et al. (2009), supporting our results. A slightly refined estimate of the source magnitude obtained using additional data constraints is not expected to significantly change the conclusions of this study.

4.3 Comparison of P/S Ratios for Synthetics and Data

4.3.1 Prediction of Phase Time Windows

The first step toward measuring the phase amplitudes is to window the phases. It is composed of two elements, arrival time and window length. The arrival times of phases

in the observed data are hand-picked, with the guidance from the predictions by the Regional Seismic Travel Time (RSTT) package distributed by Sandia National Laboratory. For the observed data, this estimate serves as good guidance for manual picking, while we use the RSTT predictions directly if no clear arrival can be identified. The lengths of windows for the observed records are determined in the same way as described below for the synthetic phases.

For shallow events, a linear equation of form $t_i = t_{offset} + Distance/v_o$ is often applied to predict travel times for different phases, where the offset and the velocity v_o need to be tuned for specific regions. The phase windows increase in length with distance, following the form $Distance/v_2 - Distance/v_1$, where v_1 and v_2 are group velocity bounds. In the earlier stage of this project we assumed this could accurately be applied to the synthetic data, with the offsets and velocities listed in Table 2.

Table 2. Velocities and Offsets used in the Linear Equation to Predict Phase Time Windows (v_o, v_1, and v_2 in km/s, Offset in Sec)

	v_o	v_1	v_2	t_{offset}
Pn	8.1	8.2	7.6	7
Pg	6.15	6.2	5.2	0
Sn	4.6	4.7	4.0	12
Lg	3.5	3.6	3.0	0
Rg	2.9	2.9	2.6	0

Although this approach gives fairly good guidance on phase windows, 3D effects appear to prevent accurate windowing of the first arriving phases like Pn. Instead we use 3D ray tracing in the SALSA3D model (Begnaud, 2015), to include any 3D structure that may affect the arrivals. The ray tracing code we use allows efficient and accurate calculation of travel times in the presence of sharp velocity contrasts (Hole, 1992). We leave out the stochastic part of the model and down-sample the velocity model to 1000 m resolution. Ray tracing provides travel times of first arriving P and S waves, which are Pn and Sn at distances beyond the crossover distance. In addition to Pn, the ray tracing provides refined prediction of Sn, which can be difficult to identify otherwise.

Both Pn and Sn travel times from the ray tracing can be well approximated by linear equations beyond the critical distances. Figure 14 (left) show examples of ray-traced P- and S-wave travel times along the path from NKNTS to INCN, with best-fit linear equations. It is clear that linear equations are good approximations to the ray-traced travel times in this area while offsets and velocities may need to be tuned for specific source-station paths to account for lateral variations (as evidenced by the best-fit v_o and offsets for Pn and Sn in Figure 14 (left) being slightly different from those in the Table 2).

Figure 14 shows that the best-fit parameters for the direct P-wave are very close to the values for Pg in Table 2, which suggests that the crustal model is sufficiently simple at shorter distances to be approximated by a 1D model. From this, we predict Pg arrival

times using the best-fit values shown in Figure 14 (right), while Lg and Rg arrival times (not obtained by ray-tracing) are predicted by the parameters in Table 2.

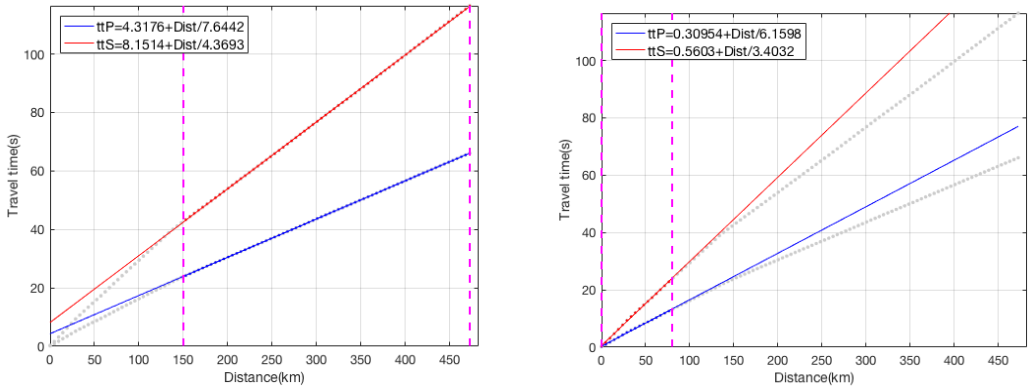

Figure 14. Travel Times Predicted by 3D Ray Tracing for the Velocity Model (SALSA3D) used in the Wave Propagation Simulations (Gray Dots). *The Distance Ranges Bounded by the Magenta Dashed Lines are Regions Where the Linear Regression is Performed for Offsets and Velocities Using Linear Travel Time Prediction. The Best-fit Parameters are Shown in the Inset at the Upper Left Corner. (Left) 150-485 km, and (Right) 0-80 km*

4.3.2 Measurement of RMS Phase Amplitude

Based on advice from W.S. Phillips (LANL) we are picking phases using RMS amplitudes. Once a phase window is in place, the RMS phase amplitude is measured in various frequency ranges (Table 3). We first apply a Butterworth filter with 2 poles and 2 passes to the entire record, before calculating the RMS values in the phase windows. We then estimate the ratios Pn/Lg, Pg/Lg, and Pn/Sn in these frequency bands. The RMS amplitudes and ratios measured at INCN are shown in Figures 15-21, where we compare the phase amplitudes and ratios estimated from the seismic records of the 2009 North Korean nuclear test to those from an ensemble of simulations with an explosive
(isotropic) source. The ensemble is composed of 5 realizations with different random seed numbers for the generation of small-scale heterogeneities. Small-scale heterogeneities are generated by coloring a white spectrum with a Von Karman correlation function for a vertical correlation length of 1 km and 5 km along vertical and horizontal directions, respectively, a Hurst exponent of 0.1, and standard deviation of 10% from 0-7.5 km depth, linearly tapering to 0% from 7.5 to 10 km depth.

Table 3. Band-pass Frequencies Where RMS Phase Amplitudes are Measured

High-pass corner	Low-pass corner
0.25 Hz	0.5 Hz
0.375 Hz	0.75 Hz
0.5 Hz	1 Hz
0.75 Hz	1.5 Hz
1 Hz	2Hz
1.25 Hz	2.5 Hz
1.5 Hz	3 Hz
2 Hz	4 Hz

We measure root-mean-square amplitudes of Pn, Pg, Sn, and Lg phases in the frequency bands tabulated in Table 3 and compare P/S ratios for data and simulations with 5-realization results for isotropic and Chiang et al. (2018) moment tensors, as well as 10-km deep double-couple results (see Figures 15-21). The simulations are carried out using one of the preferred scattering models (model 7a) from Olsen et al. (2018). The results show that the observed Pg amplitudes are well predicted in all the frequency bands by explosive and double-couple sources, where the moment tensor source by Chiang et al. (2018) produces slightly lower amplitudes than the isotropic source (Fig. 15). Estimated RMS Lg amplitudes from the double-couple ensemble are significantly higher than the other two source types, and increasingly so with frequency (Fig. 16). While the isotropic and Chiang et al. (2018) moment tensor sources predict similar Pg/Lg ratios, those from the double-couple source are lower by ~0.5 log units in the 2 - 4 Hz band. This result shows that the simulations support the use of Pg/Lg for event discrimination, with increasing efficacy at the higher frequency range tested here, consistent with conclusions derived from data (Fig. 17).

Our 5-realization ensemble simulations overpredict Pn amplitudes, particularly in the <=2 Hz bandwidth (Fig. 18). Pn amplitudes obtained by the Chiang et al. (2018) moment tensor source are closer to the observations than those predicted by the isotropic source. The large error bars associated with the Pn amplitude measurements at higher frequencies suggest that Pn amplitudes are very sensitive to the small-scale perturbations in the crust. Since Lg amplitudes are well predicted, the Pn/Lg ratios are over-predicted at various levels (Fig. 19).

Interestingly, both the isotropic and the Chiang et al. (2018) moment tensor simulations underpredict Sn amplitudes at the high frequencies (Fig. 20). The results show that the inclusion of a realistic S-wave content at the source is not able to produce Sn amplitudes in agreement with data (in fact, Sn amplitudes from the Chiang et al. (2018) moment tensor source are lower than those from the isotropic source). One interpretation of this result is that Sn is strongly dependent on P-to-S conversion, i.e., if

less P-wave energy is present in the source (such as, due to a non-isotropic source component), smaller Sn energy is generated from conversion. As Sn amplitudes generated by the double-couple source are in better agreement with those from data than those generated by the isotropic and the Chiang et al. (2018) moment tensor source, the simulated Pn/Sn ratios are not as effective for event discrimination as Pg/Lg and Pn/Lg (Fig. 21).

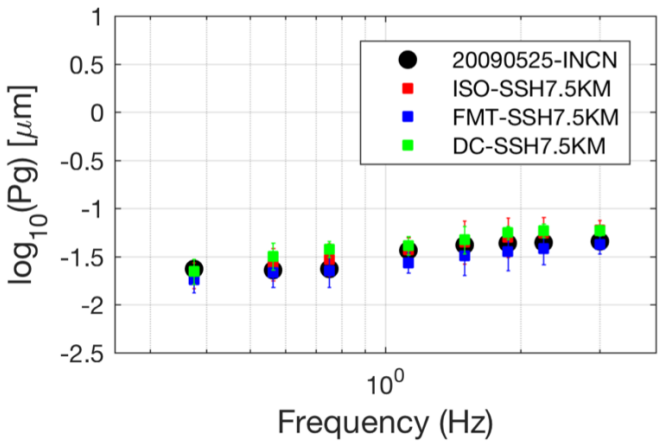

Figure 15. Pg RMS Amplitudes in Different Frequency Bands Measured from the Observed (Black) and Synthetic (Red: Isotropic Source, Blue: Moment Tensor Source by Chiang et al. (2018), Green: 10 km Double-couple Source) Vertical Velocity Component at INCN. ***Error Bars Indicate One Standard Deviation of the Mean. The Phase Amplitudes and Ratios are obtained from Simulations Including a Model of Small-Scale Heterogeneities to 7.5 km. For the Model Using Small-scale Heterogeneities to 10 km, See Figure A12.***

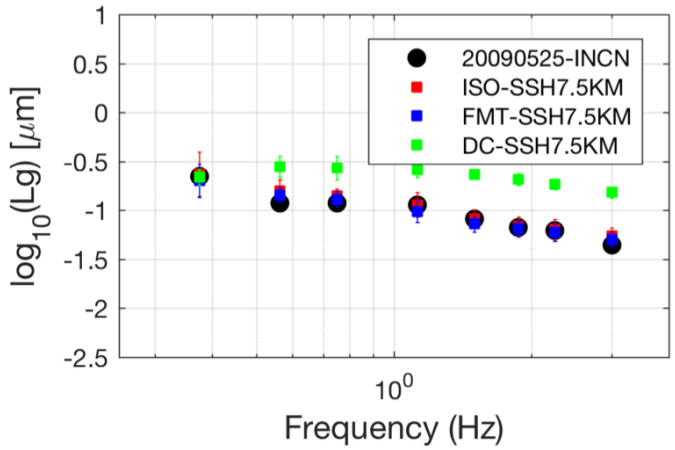

Figure 16. Same as Figure 15, but for Lg RMS amplitudes

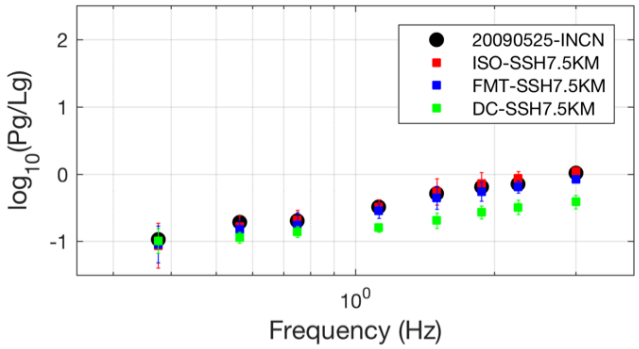

Figure 17. Same as Figure 15, but for Pg/Lg amplitude ratios

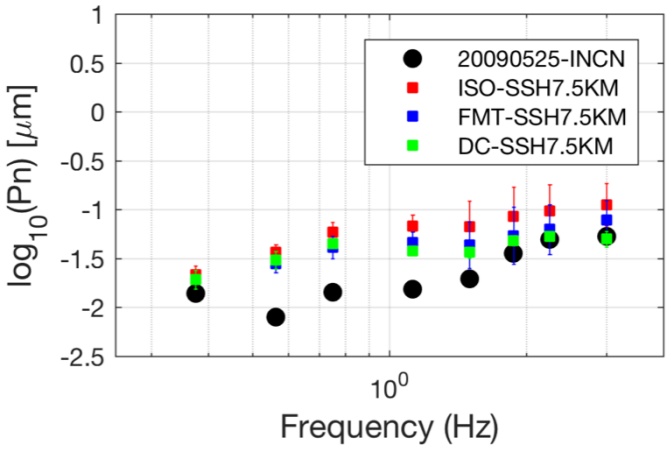

Figure 18. Same as Figure 15, but for Pn RMSAmplitudes

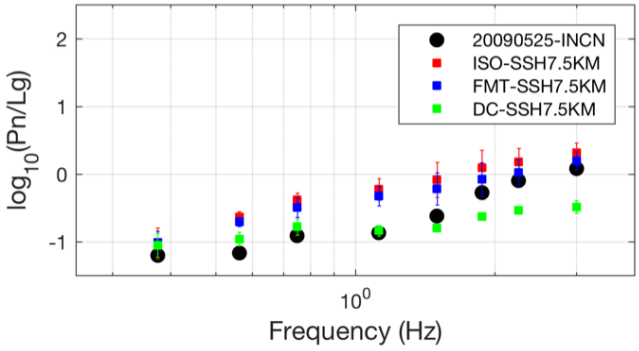

Figure 19. Same as Figure 15, but for Pn/Lg Ratios

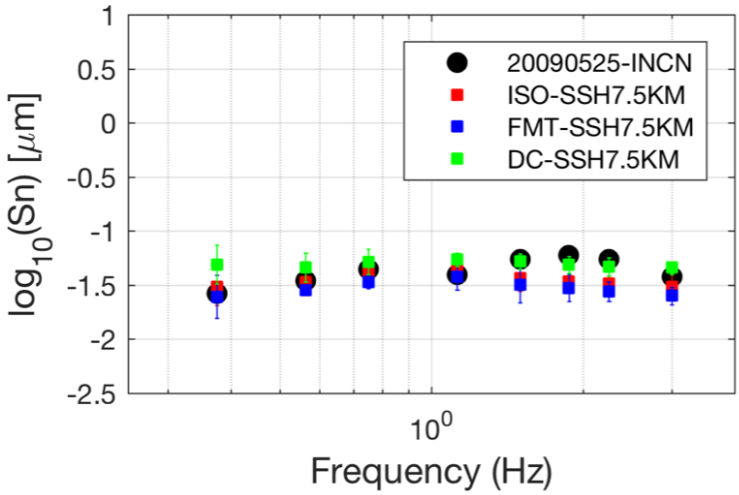

Figure 20. Same as Figure 15, but for Sn RMS Amplitudes

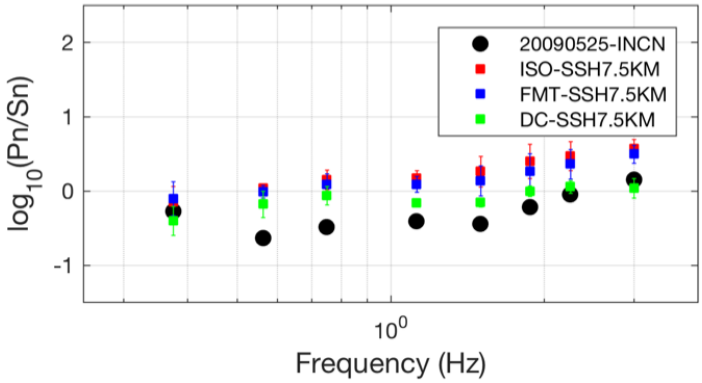

Figure 21. Same as Figure 15, but for Pn/Sn Amplitude Ratios

4.3.3 Discussion

Figures 15-21 show that the simulations produce slightly larger Pn amplitudes below 2 Hz and slightly weaker Sn amplitude between 1.5 Hz and 2.5 Hz. Here, we also tested the efficacy of a model extending the small-scale heterogeneities to deeper depth (10 km) in the crust, see Figure A11. While the fit of Pn is improved, the model generates less favorable Pg, Sn and Lg phase amplitudes as well as their ratios. Thus, we suspect that the discrepancies for Pn and Sn are not primarily related to the crustal small-scale heterogeneities.

Another possible reason for the discrepancies related to Pn and Sn is a systematic deviation of the upper mantle gradient in Vp and/or Vs in the SALSA3D model. We carried out some preliminary tests using 2D elastic FD simulations in a representative cross section of the SALSA3D model (Figs. A12 and A13). Moho depth was set at a

depth of Vp=7,600 m/s. Two end members of gradient perturbations of Vp and Vs (-2% and +2%) were tested, with the unperturbed model as the reference (Fig. A12). Figure A13 shows that perturbing the velocity gradient can manipulate Pn amplitudes at nearly all frequencies and Sn amplitudes above 1 Hz. These results indicate that lowering the Vp gradient and increasing Vs gradient in the upper mantle may improve the fits for Pn and Sn. However, more studies are needed to better constrain the values of perturbations for both Vp and Vs.

Finally, it is possible that the discrepancies associated with Pn and Sn may be related to truncating the model at 80 km depth (omitting some refracted Pn and Sn paths in the upper mantle), which should be tested in future work.

4.4 Array Analysis

Wagner and Langston (1992) and Wagner (2017) showed that array analysis can be used to constrain crustal parameters and characterize properties of the seismic wavefield. We carry out simulations of and compare array analysis at KSRS for the isotropic and Chiang et al. (2018) sources as well as for the 10-km deep double-couple source simulations to that for the data from the 2006 North Korean nuclear test, the only KSRS records we have available. However, the yield estimate and source locations for the 2006 and 2009 events are sufficiently small to justify using the 2006 data.

The analysis for the data (Fig. 22) shows that the apparent velocity starts out with ~8 km/s around the Pn arrival with high coherency and consistent direction of arrival, decreasing to ~6 km/s in the expected window of Pg with very similar direction of arrival as for Pn. Following Pg (~80-110 s), the apparent velocities and back azimuths show large variation with low coherency values, presumably caused by scattered waves generated in the heterogenous crust. Apparent velocities converge to ~4.5 km/s at the expected window of Sn, reducing to ~4.0 km/s in the adjacent Lg window, both associated with relatively high coherency. The back azimuths of the Lg waves indicate that early NNE directions turn toward N as time progresses within the phase window, suggesting that rays for late arriving Lg waves follow faster continental paths. The direction of arrival of the coda waves following the Lg window is rather erratic, with apparent velocity between 2 – 4 km/s, suggesting strong scattering late in the records.

We performed the same analysis to the synthetics computed for the isotropic moment tensor (Fig. 23), the Chiang et al. (2018) moment tensor (Fig. 24), and the double-couple moment tensor (Fig. 25). For both the isotropic and Chiang et al. (2018) moment tensor cases, the data show similar patterns in the Pn and Pg windows, as well as the strong scattering following Pg. Compared to the results for the isotropic source, the array analysis for the synthetics derived from the Chiang et al. (2018) source reveals higher coherency and consistency in the Sn and Lg windows, closer to that for the real data. On the other hand, both isotropic and Chiang et al. (2018) moment tensor source simulations predict less scattering after the Lg window as well as less variation in apparent velocity of the coda waves, as compared to that for data. The underprediction of the scattering in the late coda wave train could be due to the limited simulation domain, excluding scattered waves from larger distances. The change in direction toward north that we found in the Lg window of the data is also not clearly seen in the array analysis

for the synthetics, which may be a result of excluding sea water and bathymetry in the simulations.

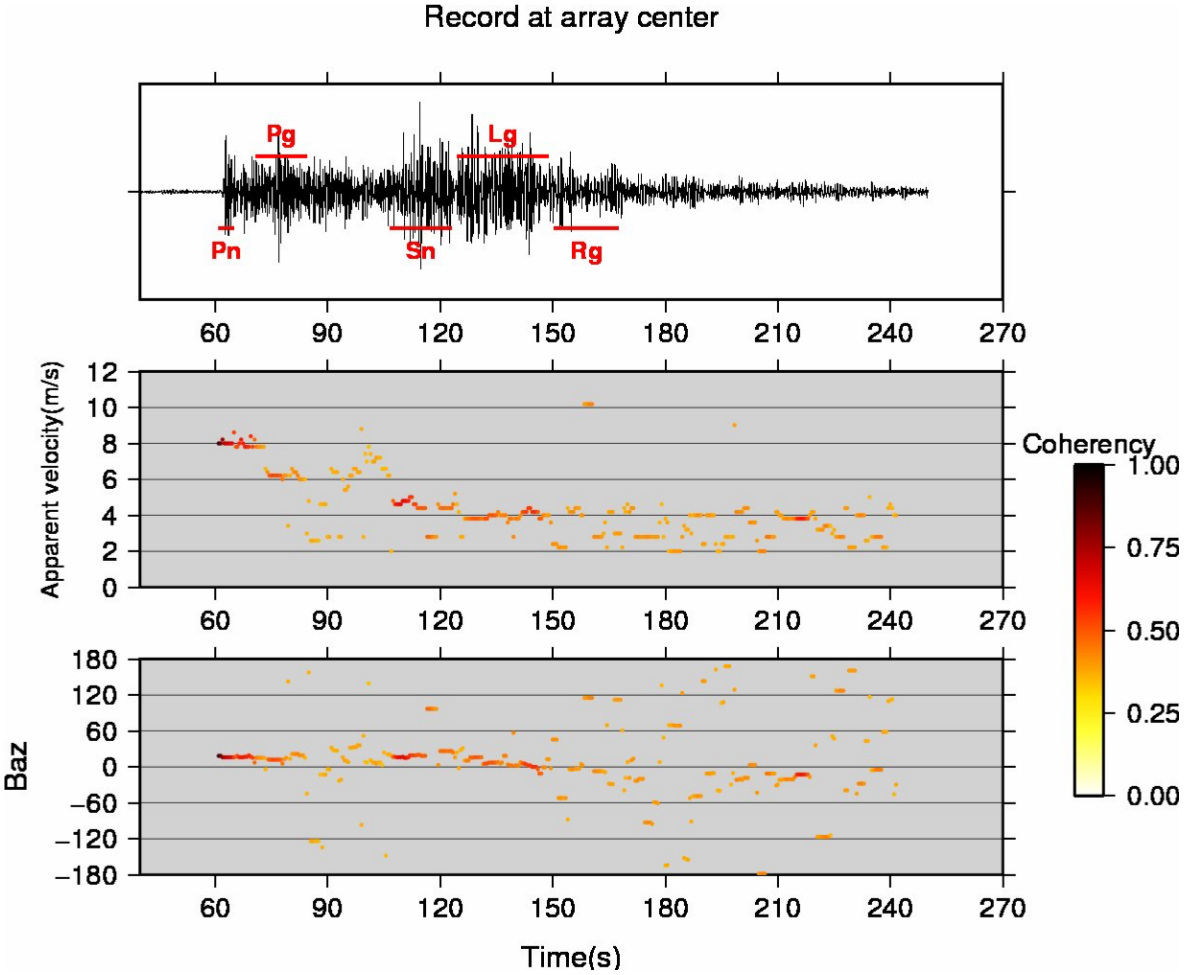

Figure 22. Array Analysis at KSRS array of the 20061009 North Korean Nuclear Test. ***Top Panel Shows the Vertical Velocity Component Seismogram at the Center of the Array with a Time Window of Seismic Phases. Middle and Bottom Panels Show Apparent Velocity and Back Azimuth, Respectively, with Colors Showing the Coherency***

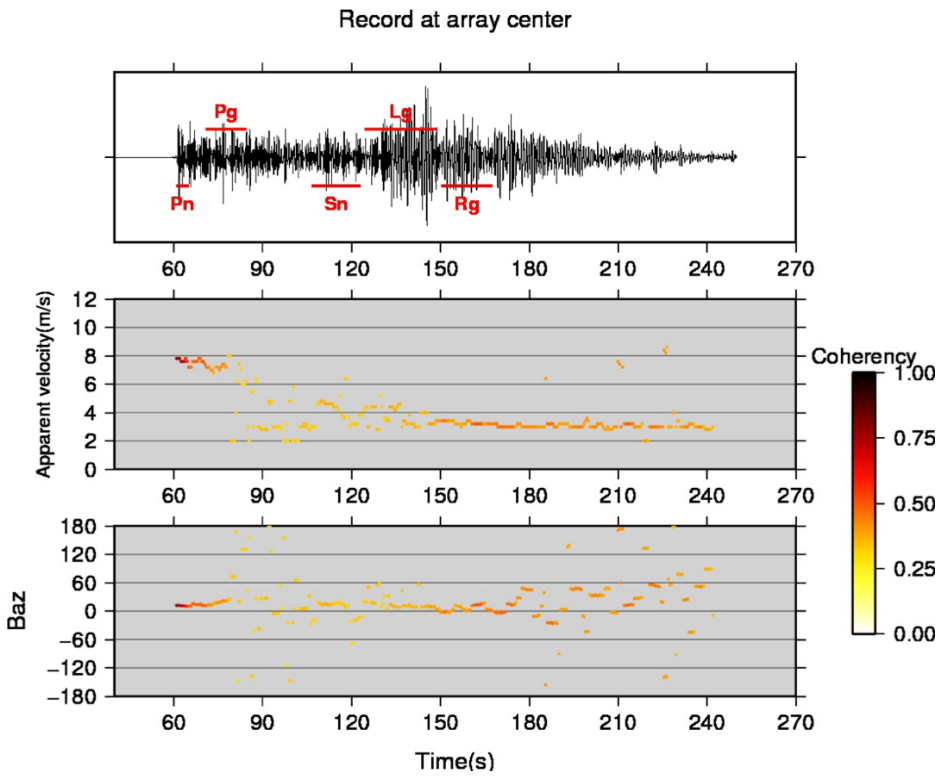

Figure 23. Same as Figure 22, but for a Simulation with an Isotropic Source

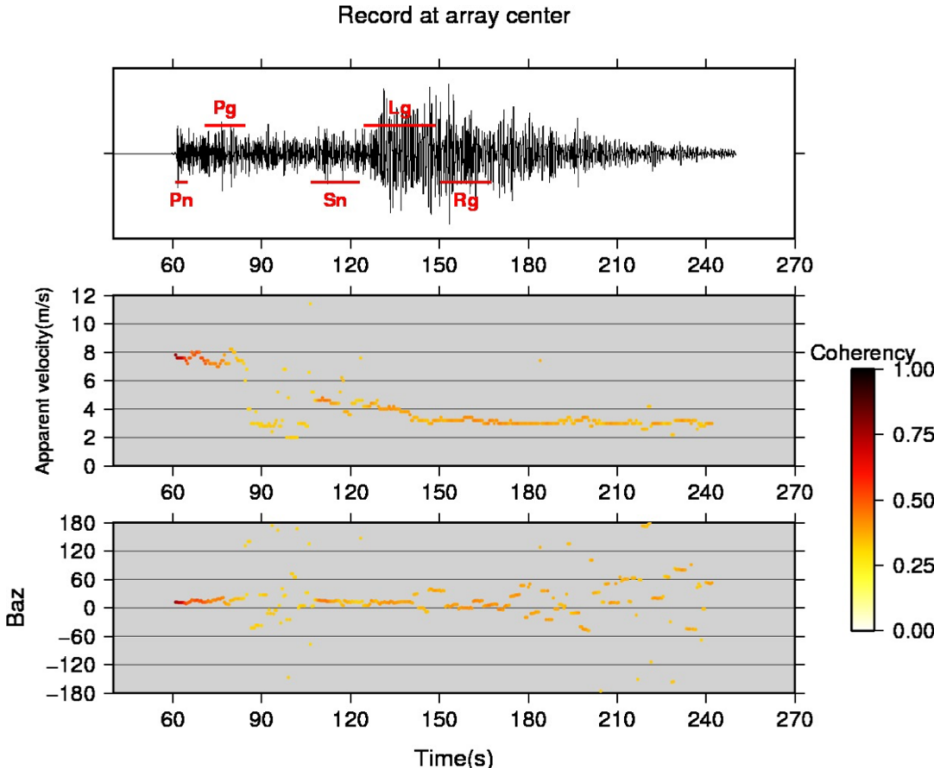

Figure 24. Same as Figure 22, but for a Simulation with the Chiang et al. (2018) Moment Tensor Source

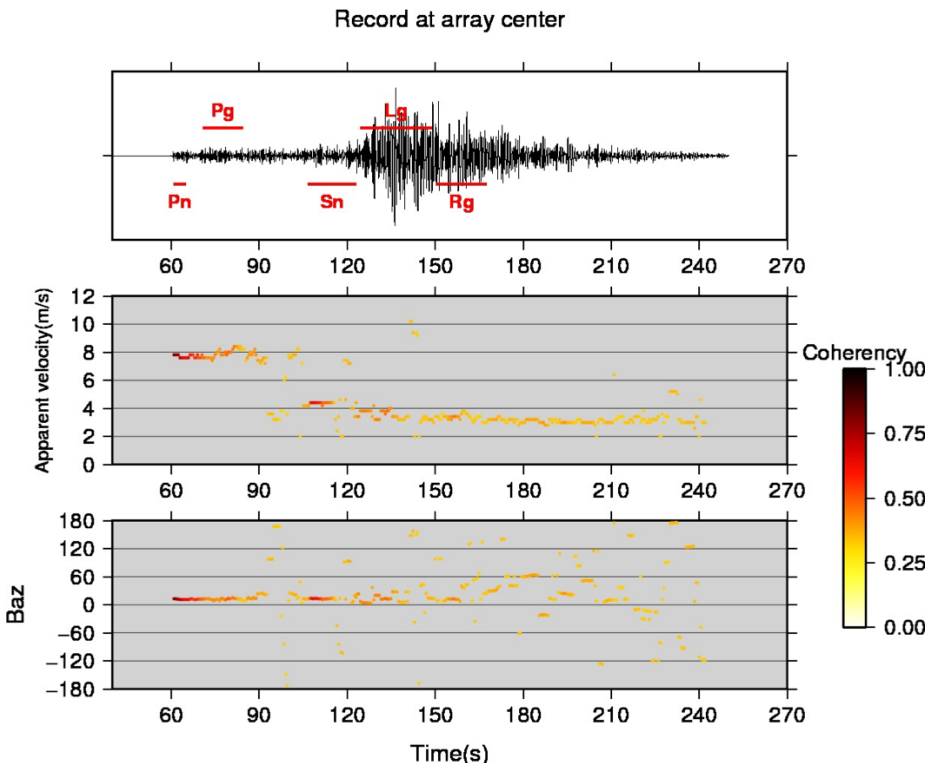

Figure 25. Same as Figure 22, but for a Simulation with a 10-km Deep Double-couple Source

4.5 Simulation of Lg waves Across the Sea of Japan

Olsen et al. (2018) have demonstrated the importance of including small-scale heterogeneities in the crust when modeling broadband (0-4 Hz) wave propagation at regional distances. For example, they showed that the envelope of broadband seismograms observed at stations INCN and TJN can be well modeled. The good agreement between the simulated and observed waveforms gives us confidence that the same approach can also be applied to a broader simulation domain, covering the Korean Peninsula and Southwest Japan (Fig. 26). However, simulating wave propagation from the NKNTS to Japan is more challenging since it covers two tectonically different environments - the continental crust beneath the Korean Peninsula and Southwest Japan, and oceanic crust beneath Sea of Japan.

Lg is known to be generated by the superposition of post-critical S-waves trapped between the Moho discontinuity and the free-surface. Kennett and Furumura (2001) showed that long-standing Lg waves require continuous constructive interference of modes to support the strong amplitude. It is therefore expected that the attenuation of Lg waves is extremely sensitive to crustal and Moho structures. As reported by Furumura et al. (2014), Furumura and Kennett (2001) and Kennett and Furumura (2001), Lg waves lose constructive interference when encountering an abrupt change of thickness of the crust, such as the transition between continental and oceanic components.

We performed an analysis on data and synthetics similar to that done by Furumura et al. (2014) to observe the attenuation of Lg through different paths. However, while Furumura et al. used earthquake sources in their analysis, we test the attenuation of Lg waves generated from a NK nuclear test. We modeled the mb=6.3 September 3 2017 which has a high signal-to-noise ratio at stations in Japan in the SALSA3D model (Begnaud, 2015). The moment tensor applied at the source location is the solution inverted from regional waveforms (Chiang et al., 2018), which contains an 84% isotropic component.

The simulations were carried out using AWP-ODC-GPU-DM (Cui et al., 2013; Nie et al., 2017), a highly scalable 4^{th}-order staggered-grid finite-differences wave propagation code with discontinuous mesh capabilities. We used a 1200 km x 700 km x 500 km domain, with a grid spacing of 90 m from 0 – 35 km depth and 270 m grid spacing at greater depths. The minimum S-wave velocity was constrained to 900 m/s, in agreement with the SALSA3D model. We incorporated the water layer above the ETOPO1 global relief model (Amante and Eakins, 2009). We adopted the same Qp=Qs=200. The source-time function is described by the time-domain reduced velocity potential (von Seggern and Blandford, 1972) with Mueller-Murphy empirical scaling parameters (Mueller and Murphy, 1971) for an explosion of a yield of 230kt (Chaves et al., 2018).

We use Lg/Sn ratios to quantify the relative strength of Lg recorded at each station; here, higher Lg/Sn ratios suggest more efficient Lg propagation, and vice versa. We bandpass filtered the waveforms to the 0.5 – 2 Hz and measured the average of the norm of the three-component waveforms for both Lg and Sn windows to estimate the mean amplitudes of Sn and Lg. We use two simulations – one without small-scale heterogeneities, and one including the preferred model from Olsen et al. (2018, vertical and horizontal correlation lengths of 1 and 5 km, Hurst number of 0.1, σ=10 % for 0-7.5 km depth, linearly tapered to 0% at 10 km depth). Figure 27 shows a comparison of waveforms at two stations in Japan, STM – 934 km, and NRW – 822 km, representing continental and oceanic crust, respectively. As expected we see that the model including small-scale heterogeneities provide the better comparison to the data. The windows used to pick the phases of Sn and Lg are shown in the figure.

Figure 28 compares the Lg/Sn ratios computed from observed and simulated waveforms at 20 stations in Korea and Japan to examine whether the simulations can produce a similar pattern as the observed. Generally, both with and without small-scale heterogeneities, the simulations produce similar patterns as those for the observed for paths along continental and oceanic crusts. We find that both data and simulations show more efficient Lg propagation along continental Asia to Kyushu and less efficient propagation along paths across the Sea of Japan where the crustal thickness is much less than that for continental crust, which are consistent with the findings of Furumura et al. (2014) for earthquake sources.

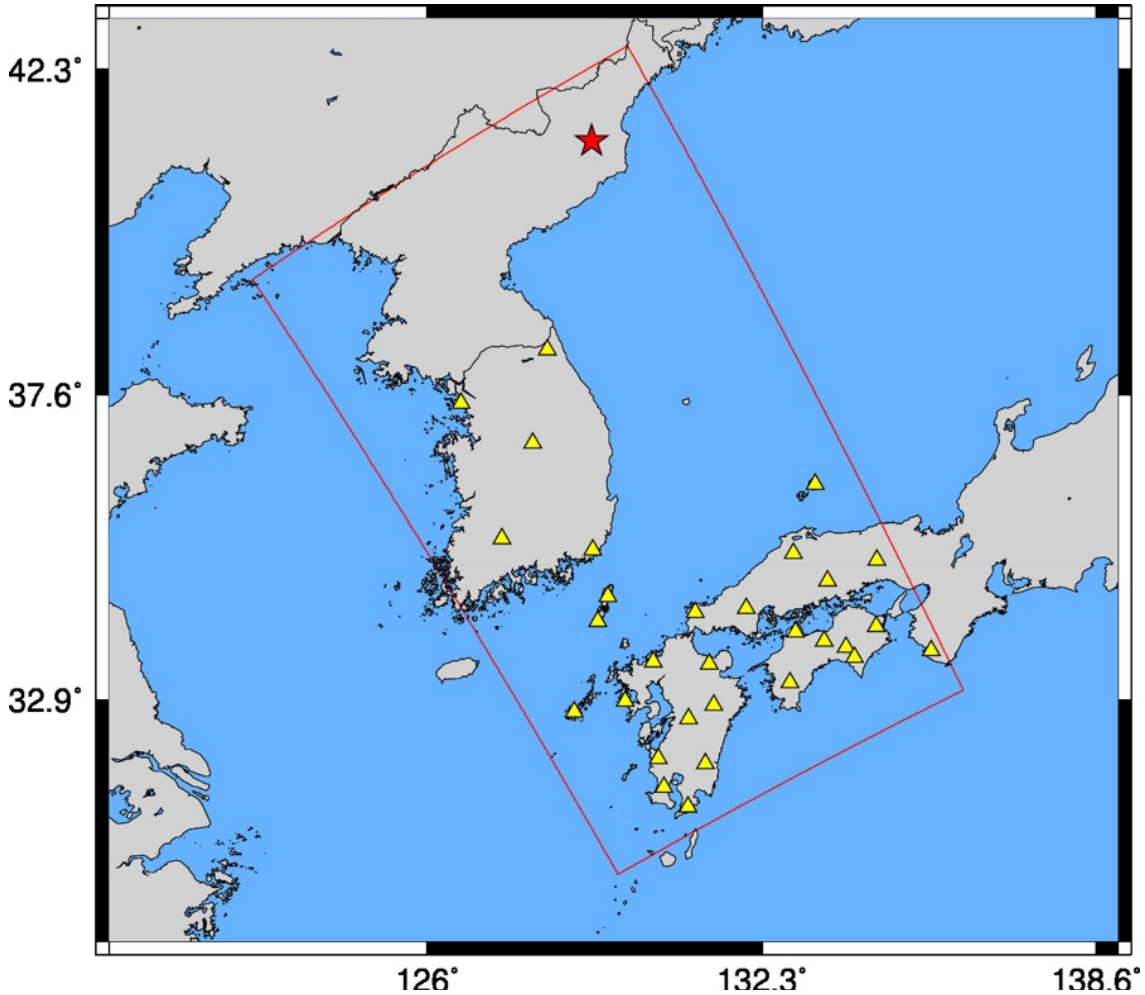

Figure 26. Simulation Domain Covering the Korean Peninsula and Southwest Japan. ***Red Star Shows the Location of the North Korean Nuclear Test Site (NKNTS). Yellow Triangles are Locations of 30 Broadband Seismic Stations with Recorded Ground Motions from the 2017 NKNTS Event used in the Analysis***

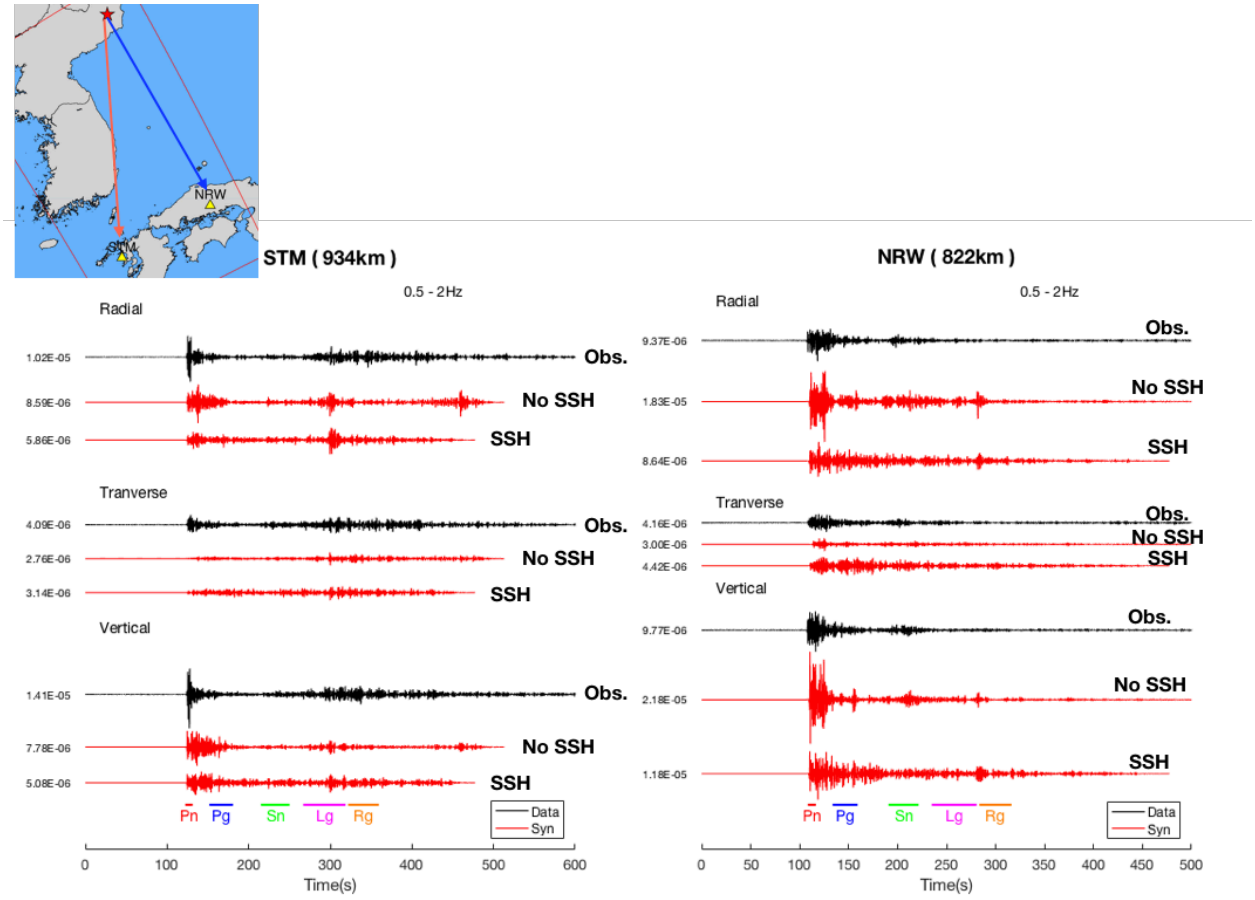

Figure 27. Comparison of Observed (black) and Simulated (red) Three-component Velocity Seismograms at Stations STM (Path Along Continental Crust) and NRW (Path Along Oceanic Crust) Bandpass Filtered to 0.5 – 2 Hz. Time Windows of Pn, Pg, Sn, Lg, and Rg are Shown on the Bottom

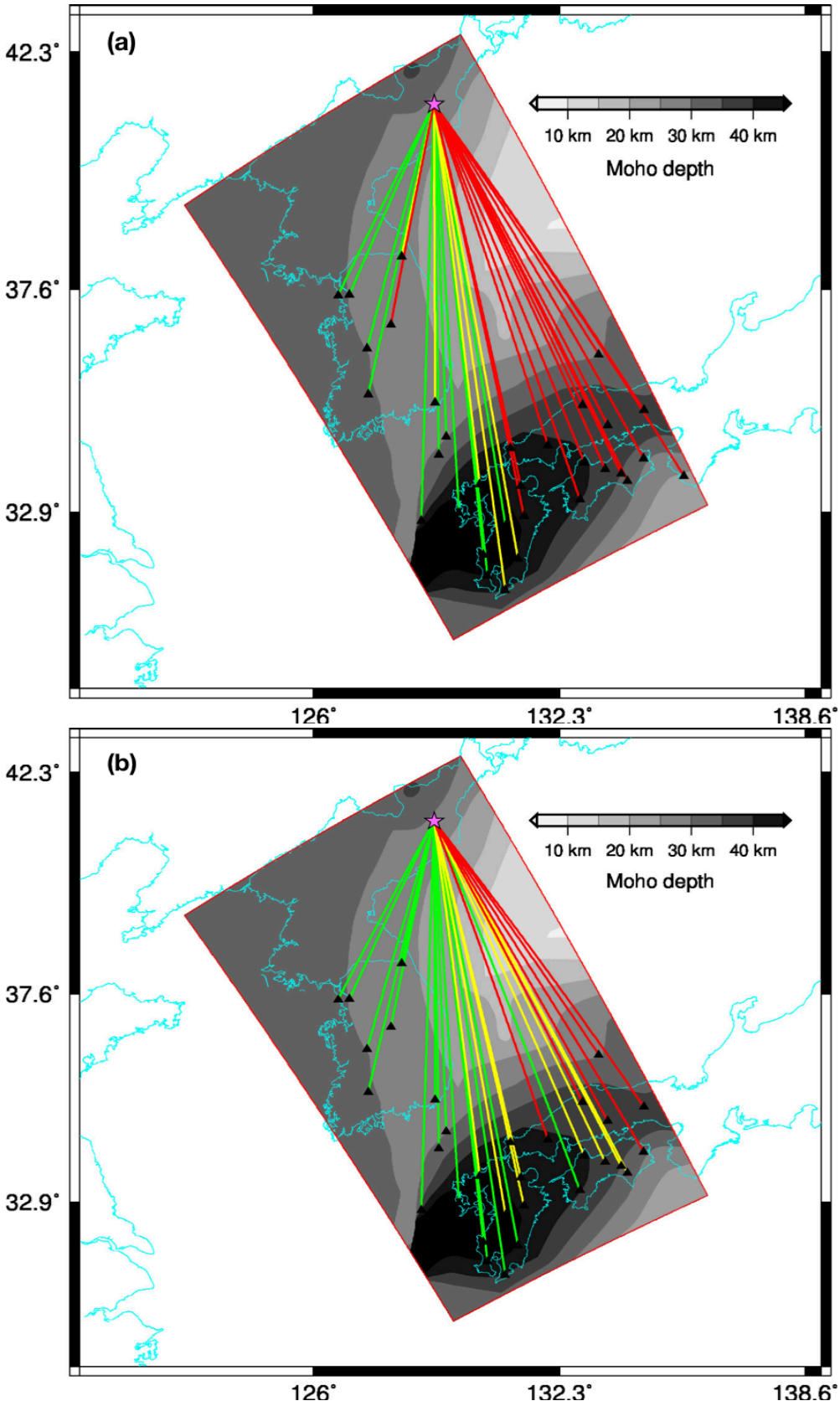

Figure 28. Comparison of 0.5 – 2 Hz Lg/Sn Ratios Measured from the Observed Seismograms (a) and from Simulations Without (b) and with (c) Small-scale Heterogeneities (SSH). ***Efficient Lg Propagation Paths are Shown in Green Where Lg/Sn > 1.5, Yellow Lines Show Less Efficient Lg Propagation Paths with 1 < Lg/Sn < 1.5, and Red Lines are Paths Where Lg is Highly Attenuated with Lg/Sn < 1***

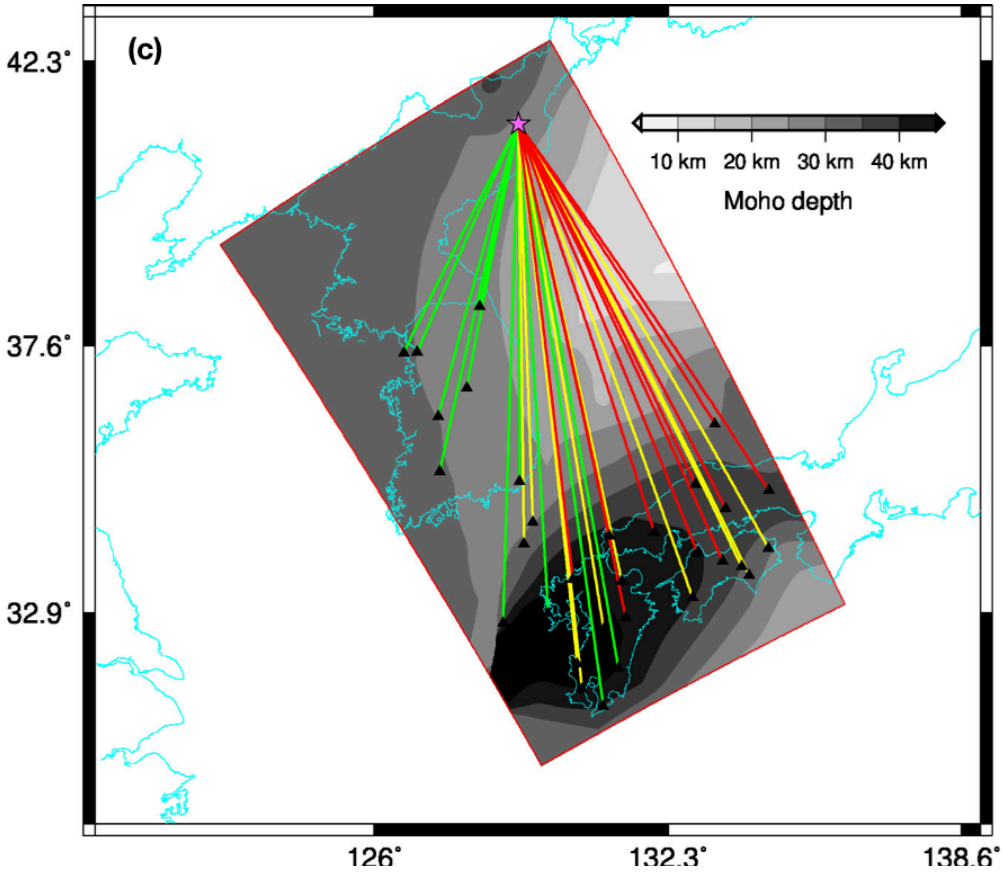

Figure 28. (Cont.) Comparison of 0.5 – 2 Hz Lg/Sn Ratios Measured from the Observed Seismograms (a) and from Simulations Without (b) and with (c) Small-scale Heterogeneities (SSH).*Efficient Lg Propagation Paths are Shown in Green Where Lg/Sn > 1.5, Yellow Lines Show Less Efficient Lg Propagation Paths with 1 < Lg/Sn < 1.5, and Red Lines are Paths Where Lg is Highly Attenuated with Lg/Sn < 1*

4.6 Statistical Characterization of Surface Topography

Another source of scattering is surface topography. We have analyzed the statistical properties of the topographic variation in North Korea in order to understand its statistical properties.

We first modeled the radially averaged 2D Power Spectral Density (PSD derived from the topography around the NKNTS using the same statistics as used for the small-scale heterogeneities in the current simulations, namely colored Gaussian noise with a von Karman autocorrelation and power spectrum of the form:

$$P(k) = \frac{4\pi\varepsilon^2 a^2 \Gamma(\kappa+1)}{\Gamma(\kappa)(1+a^2k^2)^{\kappa+1}} \quad , \qquad (7)$$

where a is the correlation length, κ is the Hurst exponent, ε is the magnitude of the fluctuation, and $\Gamma(x)$ is the Gamma function. To determine the parameters of the Von Karman function, we fit the observed 2D PSD by performing a nonlinear parameter optimization procedure. To estimate uncertainties of the model parameters, we collect an ensemble of models that give statistically similar misfits.

The results are shown in Figure 29. The estimate of the Hurst exponent κ is approximately 1.15, and the ensemble of plausible models show that a wide range of correlation lengths (50 km $\pm$ 20 km, much longer than those for the crustal heterogeneities, ~ 1-5 km) can fit the observed PSD equally well. In addition, the predicted von Karman function overpredicts the spectral energy for smaller wavenumbers. These results suggest that a von Karman distribution is not be an ideal function to model topography data.

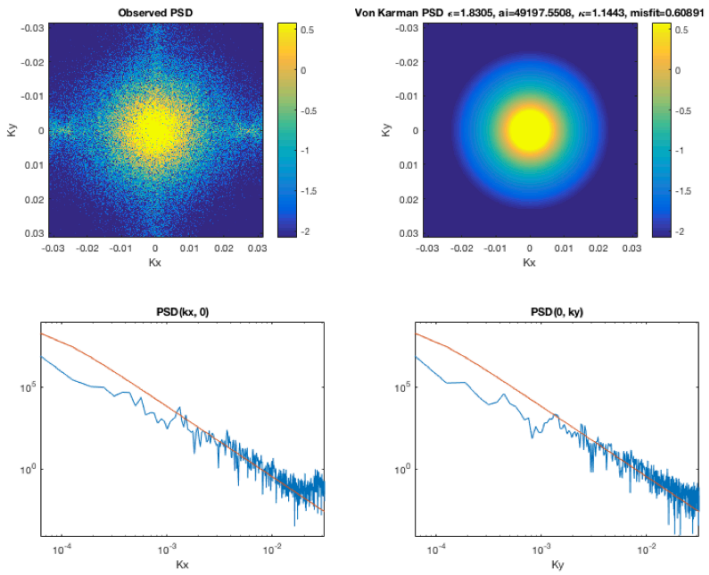

Figure 29. Comparison of Observed and Predicted 2D Power Spectral Density (PSD) using a von Karman Function. ***(Upper left) Observed 2D PSD of the Non-dimensional Topography. (Upper right) von Karman 2D PSD, Computed by the Parameters Shown at the Top of the Panel. (Lower left) Cross Section of Observed (Blue) and von Karman (Red) PSD Along the Kx Direction at Ky=0. (Lower Right) Cross Section of Observed (Blue) and von Karman (Red) PSD Along the Ky Direction at Kx=0***

Instead, we do the analysis using a power-law function,

$$P(k) = P_0 k^{\beta} \propto k^{\beta} \quad , \qquad (8)$$

where k is the wavenumber, P_0 is a scaling coefficient (not used in the following analysis), and the exponent β is the slope in log-log space. We examined the topography in 100 km x 100 km (Fig. 30), 150 km x 150 km (Fig. 31), and 200 km x 200 km (Fig. 32

domains around the NKNTS. The results reveal that the exponent β is approximately 3.5 regardless of domain sizes. This suggests that the statistical property of near-source topography is stable and can be well approximated by a power-law PSD with an exponent of 3.5.

Based on the results of the 100 km x 100 km domain analysis, an ensemble of simulated topography fields is generated to compare with the observed topography (Fig. 33). Note that the simulated topography fields are scaled such that they have the same mean and standard deviation as the observed topography. The comparison shows that observed and simulated fields are exhibiting similar features, supporting that the estimated statistical parameters can characterize the topography.

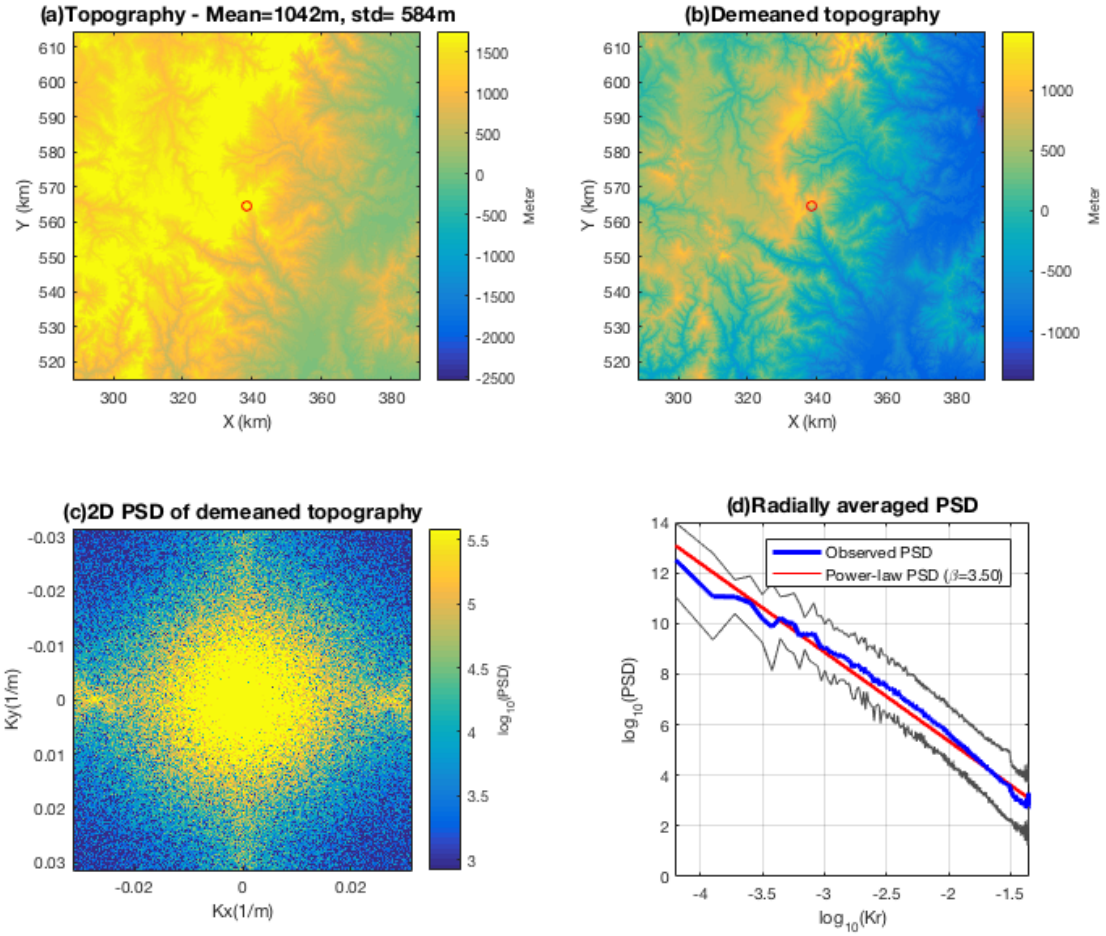

Figure 30. (a) Topography Included in a 100 km x 100 km Area Around the NKNTS, Where the Red Open Circle Indicates the Test Site. (b) De-meaned Version of the Topography Shown in (a). (c) 2D Power Spectral Density (PSD) of the De-meaned Topography Shown in (b). (d) Blue Curve Shows Radially Averaged PSD Derived from the 2D PSD Shown in (c) and the Red Curve Shows the Prediction of Power-law Function with Exponent of 3.5

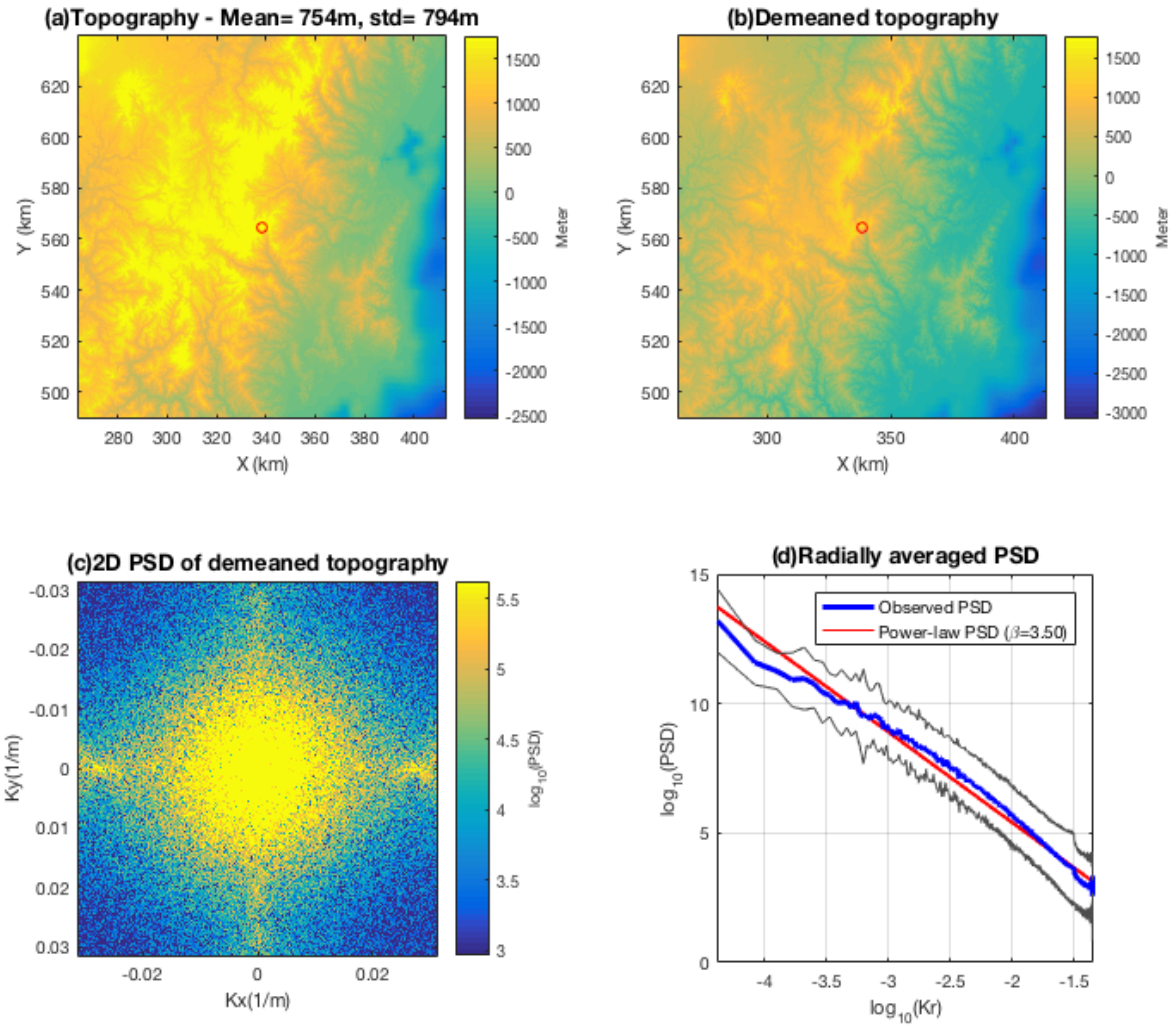

Figure 31. (a) Same as Fig. 30, but for a 150 km x 150 km Domain Around the NKNTS

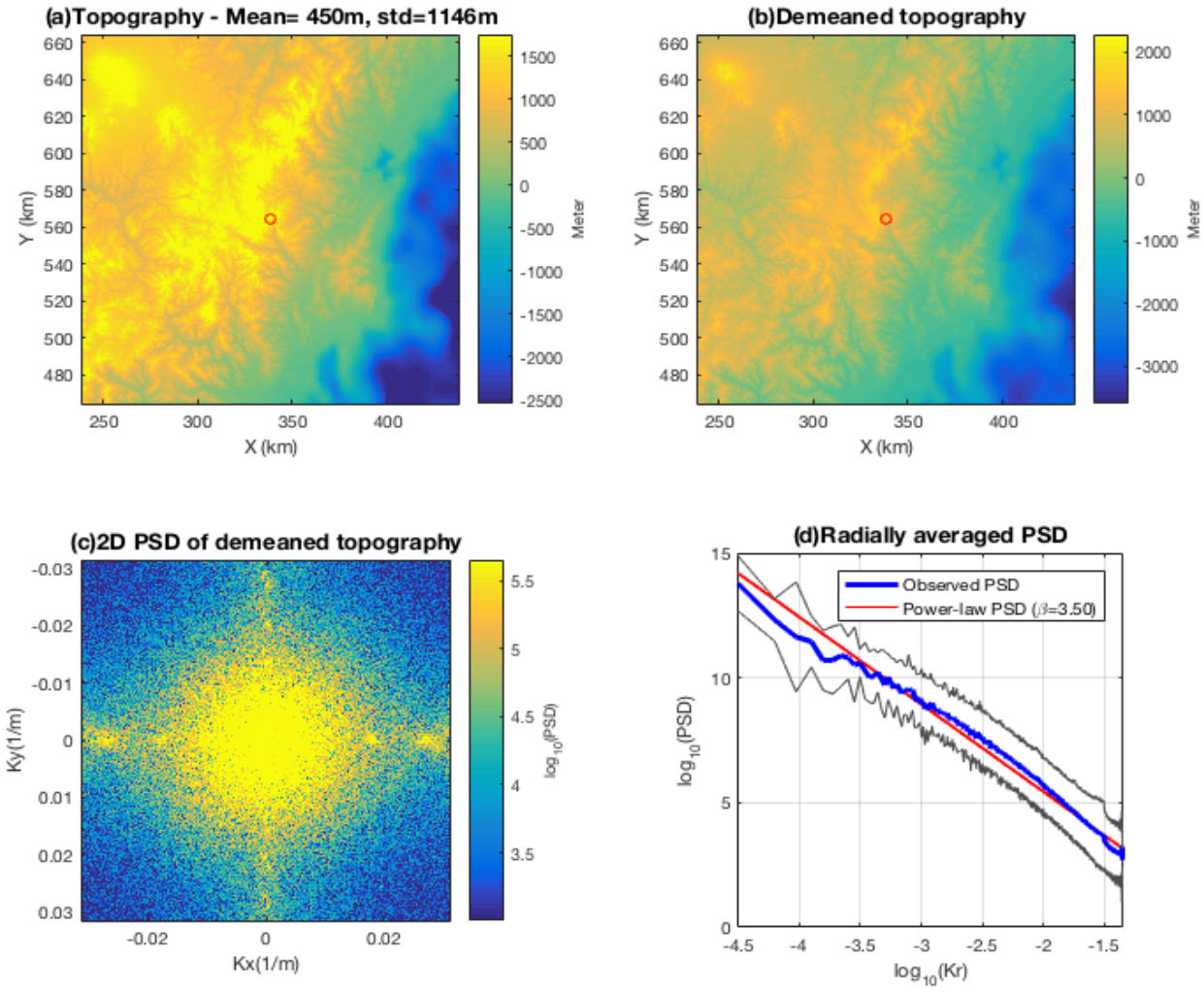

Figure 32. (a) Same as Fig. 30, but for a 200 km x 200 km Domain Around the NKNTS

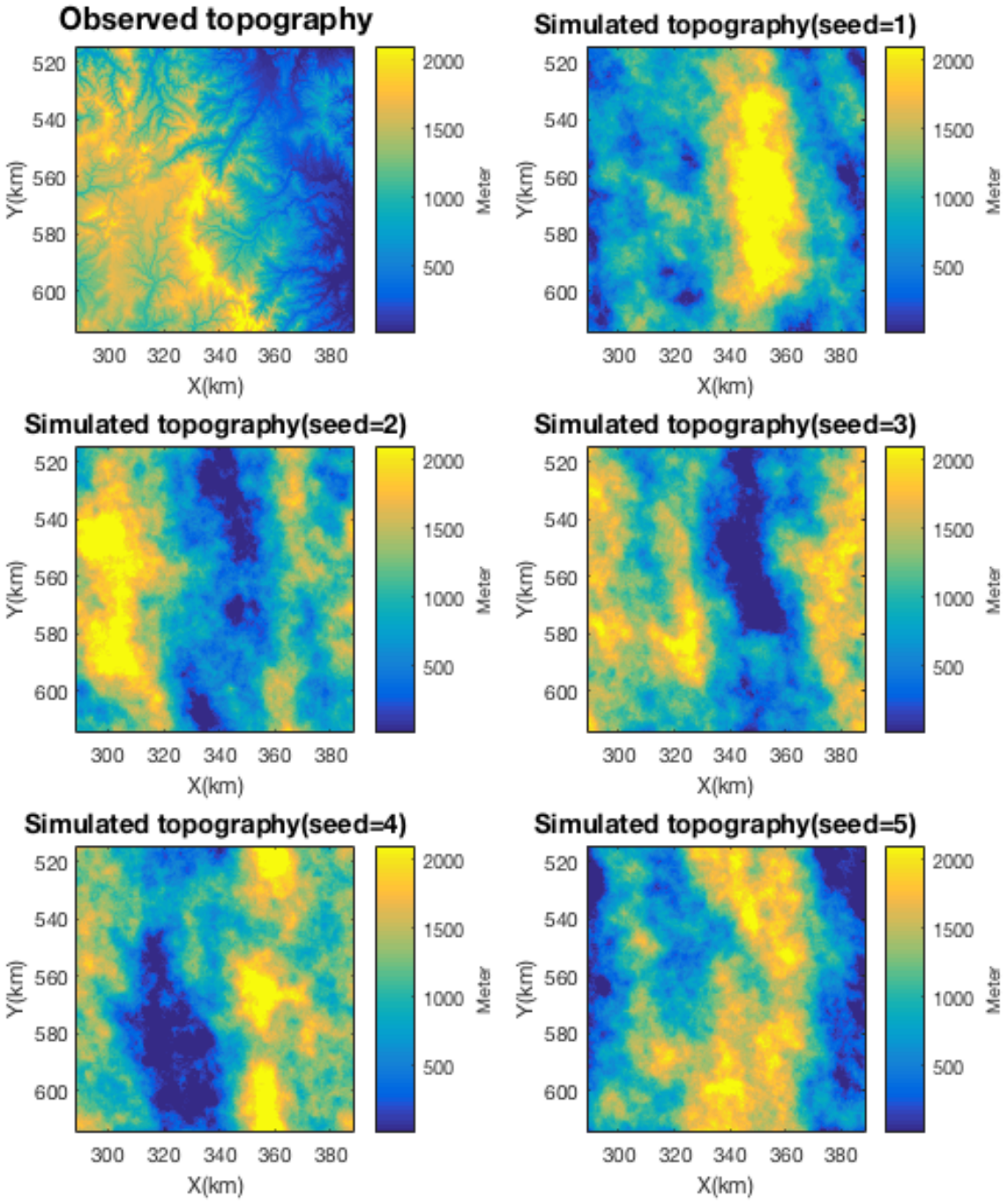

Figure 33. Comparison of the Observed Topography in the 100 km x 100 km Domain Around the NKNTS and Five Realizations of Simulated Topography Fields Based on the Power-law PSD with the Derived Statistical Parameters

5. CONCLUSIONS

Recent advances in high-performance computing have facilitated fully deterministic 3D elastodynamic simulations of regional wave propagation (400+ km). We demonstrate these capabilities by modeling time histories for the 2009 North Korea nuclear explosion recorded at stations in South Korea for frequencies up to 4 Hz in the Sandia/ Los Alamos National Laboratory SALSA3D velocity model. Comparison of the synthetics and data show that the SALSA3D model fails to reproduce the main characteristics of the data for this bandwidth. In particular, the synthetics grossly overpredict Rayleigh-wave amplitudes and underpredict the amplitudes of the coda. On the other hand, the addition to SALSA3D of small-scale perturbations of the P and S velocities and densities following a von Karman distribution with correlation lengths of ~1000 m, a Hurst number of 0.1, and an H/V anisotropy of ~5 improves the fit considerably. The results show that constant Q of 200 (INCN) to 350 (TJN) below 1 Hz and a power-law exponent of ~0.3 for both P and S waves generate synthetics in best agreement with the data. The results show that the wave propagation along the 400+ km path from the 2009 NKNTS to INCN and TJN is strongly sensitive to the parameters of the small-scale crustal and mantle heterogeneities, as well as to the frequency-dependent attenuation. Larger scale structure may also contribute to the reduction of an otherwise much-too-large amplitude Rayleigh wave.

Our simulations show a strong depth dependency of the strength of the small-scale heterogeneities on the signature of the synthetics simulated at INCN and TJN from the NKNTS with constraints from data. In particular, models with a gradient in the strength of the velocity and density perturbations and strong scattering (10%) limited to the top 7.5–10 km of the crust tend to provide the synthetics with the best fit to data. Scattering contributions from deeper parts of the crust and mantle are shown to generate Pn and Pg amplitudes much below those for the data at the two stations. Specifically, the amplitude at the onset of the Pn phase can be significantly affected, even for a standard deviation as low as 2% of the small-scale velocity and density perturbations, with respect to the background SALSA3D variation in the lower crust and upper mantle. This result is important for methods used to discriminate between explosive and earthquake sources based on the amplitudes of P and S waves.

The fit between synthetics and data is improved for the transverse component at regional distances on the long periods, while the match of the envelope at higher frequencies is mostly unchanged when a ~20% non-isotropic energy component is included in the source. The results of simulations for which the small-scale heterogeneities are omitted in the close vicinity of the source indicate that a little (high-frequency) scattering from the near-source area accumulates over the regional path. Our study thus suggests that a significant portion of the high-frequency S-wave energy is generated by P-S wave scattering, primarily in the upper crust.

Observed Pg and Lg amplitudes and Pg/Lg ratios are well predicted in all frequency bands up to 4 Hz by explosive (isotropic and 20% non-isotropic and double-couple sources, while the Pg/Lg ratios from the double-couple source are lower by ~0.5 log units in the 2 - 4 Hz band. Pn amplitudes are overpredicted, particularly in the 0-2 Hz bandwidth, where the 20% non-isotropic moment tensor source generates Pn amplitudes closer to the observations than those predicted by the isotropic source. Pn/Lg ratios are

over-predicted, and the isotropic and the 20% non-isotropic moment tensor simulations underpredict Sn amplitudes at the high frequencies. This result indicates that the inclusion of a realistic S-wave content at the source is not able to produce Sn amplitudes in agreement with data. As a result, the simulated Pn/Sn ratios are not as effective for event discrimination as Pg/Lg and Pn/Lg.

Array analysis for KSRS data and synthetics for NKNTS events and deep double-couple events confirms that our favored small-scale heterogeneity models of the Korean crust dramatically lower the coherency for the simulations, to a level similar to that for the data. Back azimuths and apparent velocities are generally in the expected range for Pn, Pg, Sn, Lg and Rg. A drop in apparent velocities from the expected P-wave speeds to S-wave speeds after Pn compared to those for the double-couple source indicates a different scattering behavior for the two different source types (e.g., P-S versus S-P scattering). A likely interpretation is that the predominant S wave train for the double-couple source is very efficiently generating converted S-P scattered waves after Pn.

Lg/Sn ratios computed from 0-2 Hz simulated waveforms for a 20% non-isotropic source from NKNTS at 20 stations in Korea and Japan with and without small-scale heterogeneities produce similar patterns as those for the observed for paths along continental and oceanic crusts. We find that both data and simulations show more efficient Lg propagation along continental Asia to Kyushu and less efficient propagation along paths across the Sea of Japan, consistent with the findings of Furumura et al. (2014) for earthquake sources.

Finally, we successfully model the radially-averaged 2D Power Spectral Density (PSD) derived from the topography around the NKNTS using a power-law PSD with an exponent of 3.5.

Our results demonstrate that state-of-the-art high-frequency 3D wave propagation simulations using high-performance computing can reproduce the general character of records for stations located hundreds of kilometers from the source. We recommend that future work continue to take advantage of these computing capabilities to refine the estimates of the parameters for Q(f) and small-scale heterogeneities with systematic inversion methods, rather than trial and error modeling, to further minimize any bias from inter-dependency between modeling parameters.

REFERENCES

Amante, C. and B. W. Eakins (2009), ETOPO1 arc-minute global relief model: procedures, data sources and analysis, Technical Memorandum NESDIS NGDC-24, National Oceanic and Atmospheric Administration, Miami, FL.

Baker, G. Eli, J. L. Stevens and H. Xu (2012), "Explosion Shear-Wave Generation in High-Velocity Source Media," Bulletin of the Seismological Society of America, **102**, pp. 1301-1319, doi:10.1785/0120110119.

Begnaud, M. (2015), Extending SALSA3D: Adding secondary phases to a global 3D model for improved seismic event location, Seism. Res. Lett., **86**:2B, p. 679.

Bielak, J., R.W. Graves, K.B. Olsen, R. Taborda, L. Ramirez-Guzman, S.M. Day, G.P. Ely, D. Roten, T.H. Jordan, P.J. Maechling, J. Urbanic, Y. Cui, and G. Juve (2010), The ShakeOut earthquake scenario: Verification of three simulation sets, Geophysical Journal International, **180**, pp. 375-404, doi: 10.1111/j.1365-246X.2009.04417.x.

Birch, F. (1961), The velocity of compressional waves in rocks to 10 kilobars, Part 2, Journal of Geophysical Research, **66** (7), pp. 2199-2224.

Chaves, E. J., T. Lay, and D. P. Voytan (2018), Yield Estimate (230 kt) for a Mueller-Murphy Model of the 3 September 2017, North Korean Nuclear Test (mbNEIC= 6.3) From Teleseismic Broadband P Waves Assuming Extensive Near-Source Damage, Geophysical Research Letters, **45**(19), pp. 10,314-10,322.

Chiang, A., G. A. Ichinose, D S. Dreger, S. R. Ford, E. M. Matzel, S. C. Myers, and W. R. Walter (2018), Moment Tensor Source-Type Analysis for the Democratic People's Republic of Korea–Declared Nuclear Explosions (2006–2017) and 3 September 2017 Collapse Event, Seismological Research Letters, **89**(6), pp. 2152-2165.

Cui, Y., E. Poyraz, K.B. Olsen, J. Zhou, K. Withers, S. Callaghan, J. Larkin, C. Guest, D. Choi, A. Chourasia, Z. Shi, S.M. Day, J.P. Maechling, and T.H. Jordan (2013), Physics-based seismic hazard analysis on petascale heterogeneous supercomputers, Procs, Supercomputing Conference, Denver, CO, 17-21 November.

Cui, Y., K. Olsen, T. Jordan, K. Lee, J. Zhou, P. Small, D. Roten, G. Ely, D. Panda, A. Chourasia, et al. (2010), Scalable earthquake simulation on petascale supercomputers, Procs. Supercomputing Conference, New Orleans, Louisiana, 13-19 November.

Day, S. M., R. W. Graves, J. Bielak, D. Dreger, S. Larsen, K. B. Olsen, A. Pitarka, and L. Ramirez-Guzman (2008), Model for basin effects on long-period response spectra in southern California, Earthquake Spectra, **24**, pp. 257-277.

Day, S. M., J. Bielak, D. Dreger, R. Graves, S. Larsen, K. B. Olsen, and A. Pitarka (2001), Tests of 3D elastodynamic codes: Final report for Lifelines Project 1A01, Pacific Earthquake Engineering Research Center, Berkeley, CA.

Day, S. M., J. Bielak, D. Dreger, R. Graves, S. Larsen, K. B. Olsen, and A. Pitarka (2003), Tests of 3D elastodynamic codes: Final report for Lifelines Project 1A02, Pacific Earthquake Engineering Research Center, Berkeley, CA.

De, G.S., D.F. Winterstein, and M.A. Meadows (1994), Comparison of P- and S-wave velocities and Q's from VSP and sonic log data, Geophysics, **59**(10), pp. 1512-1529.

Dolan, S., C. Bean, and B. Riollet (1998), The broad-band fractal nature of heterogeneity in the upper crust from petrophysical logs, Geophys. J. Int., **132**(3), pp. 489-507.

Ford, S.R., D.S. Dreger, and W.R. Walter (2009), Source analysis of the Memorial Day explosion, Kimchaek, North Korea, Geophysical Research Letters, **36,** L21304, doi:10.1029/2009GL040003.

Ford, S.R., W.S. Phillips, W. R. Walter, M.E. Pasyanos, K. Mayeda, and D. S. Dreger (2010), Attenuation Tomography of the Yellow Sea/Korean Peninsula from Coda-source normalized and direct Lg Amplitudes, Pure Appl. Geophys., **167**, pp. 1163-1170.

Frankel, A. and R. W. Clayton (1986), Finite difference simulations of seismic scattering: implications for the propagation of short-period seismic waves in the crust and models of crustal heterogeneity, J. geophys. Res., **91**(B6), pp. 6465-6489.

Furumura, T. and B.L.N. Kennett (2001), Variations in regional phase propagation in the region around Japan, Bull. Seism. Soc. Am., **91**, pp. 668-682.

Furumura, T., T. K. Hong, and B. L. Kennett (2014), Lg wave propagation in the area around Japan: observations and simulations, Progress in Earth and Planetary Science, **1,** pp. 1-20.

Hartzell, S., S. Harmsen, and A. Frankel (2010), Effects of 3D random cor-related velocity perturbations on predicted ground motions, Bull. Seism. Soc. Am., **100**(4), pp. 1415-1426.

Hole, J. A. (1992), Non-linear high resolution three-dimensional seismic travel time tomography, J. Geophys. Res., **97**, pp. 6553-6562.

Holliger, K. (1996), Upper-crustal seismic velocity heterogeneity as de- rived from a variety of P-wave sonic logs, Geophys. J. Int., **125**(3), pp. 813-829.

Holliger, K. (1997), Seismic scattering in the upper crystalline crust based on evidence from sonic logs, Geophys. J. Int., **128**(1), pp. 65-72.

Hong, T-K. and J. Rhie (2009), Regional source scaling of the 9 October 2006 underground nuclear explosion in North Korea, Bull. Seis. Soc. Am., **99**, 4, pp. 2523-2540.

Imperatori, W. and P.M. Mai (2013), Broad-band near-field ground motion simulations in 3-dimensional scattering media, Geophys. J. Int., **192**(2), pp. 725-744.

Jacobsen, B.H. and K.B. Olsen (2011), Spatial variability of ground motion amplification from low-velocity sediments including fractal inhomogeneities with special reference to the Southern California basins, EGU General Assembly, Vienna, Austria, 3-8 April..

Kennett, BLN and T. Furumura (2001), Regional phases in continental and oceanic environments, Geophys. J. Int., **146**, pp. 562-568.

Lekic, V., J. Matas, M. Panning, and B. Romanowicz (2009), Measurement and implications of frequency dependence of attenuation, Earth Planet. Sci. Lett., **282**, pp. 285-293.

Levander, A.R., R.W. England, S.K. Smith, R.W. Hobbs, J.A. Goff, and K. Holliger (1994), Stochastic characterization and seismic response of upper and middle crustal rocks based on the Lewisian Gneiss Complex, Scotland, Geophys. J. Int., **119**(1), pp. 243-259.

McNamara, D., M. Meremonte, J. Z. Maharrey, S.-L. Mildore, J. R. Altidore, D. Anglade, S. E. Hough, D. Given, H. Benz, L. Gee, et al. (2012), Frequency- dependent seismic attenuation within the Hispaniola Island region of the Caribbean Sea, Bull. Seismol. Soc. Am., **102**, pp. 773-782, ISSN: 0037-1106.

Mitchell, B.J., T. Pan, J. Xie, and L. Cong (1997), Lg coda Q variation across Eurasia and its relation to crustal evolution, Bull. Seis. Soc. Am., **102**, pp. 22,767-22,779.

Mueller, R. A. and J. R. Murphy (1971), Seismic characteristics of underground nuclear detonations: Part I, Seismic spectrum scaling, Bulletin of the Seismological Society of America, **61**(6), pp. 1675-1692.

Nafe, J.E. and C. L. Drake (1957), "Variation with depth in shallow and deep water marine sediments of porosity density and the velocities of compressional and shear waves," Geophysics, **22,** p. 523

Nakata, N. and G. Beroza (2015), Stochastic characterization of mesoscale seismic velocity heterogeneity in Long Beach, California, Geophys. Jour. Int., **203**, pp. 2049-2054.

Nie, S., Y. Wang, Y., K. B. Olsen, and S. M. Day (2017), Fourth-Order Staggered-Grid Finite-Difference Seismic Wavefield Estimation Using a Discontinuous Mesh Interface (WEDMI)Fourth-Order Staggered-Grid Finite-Difference Seismic WEDMI, Bulletin of the Seismological Society of America, **107**(5), pp. 2183-2193.

Olsen, K.B. (1994), Simulation of three-dimensional wave propagation in the Salt Lake Basin, Ph.D. Thesis, University of Utah, Salt Lake City, Utah.

Olsen, K.B. (2000), Site Amplification in the Los Angeles Basin from 3D Modeling of Ground Motion, Bull. Seis. Soc. Am., **90**, pp. S77-S94.

Olsen, K.B., M. Begnaud, S. Phillips, and B.H. Jacobsen (2018), Constraints of Crustal Heterogeneity and Q(f) from Regional (< 4 Hz) Wave Propagation for the 2009 North Korea Nuclear Test, Bull. Seism. Soc. Am., **108**(3A), pp. 1369-1383.

Patton, H.J. and F.V. Pabian (2014), Comment on "Advanced seismic analysis of the source characteristics of the 2006 and 2009 North Korean nuclear tests," by J.R. Murphy, J.L. Stevens, B.C. Kohl, and T.J. Bennett, Bull. Seis. Soc. Am., **104**, 4, pp. 2104-2110.

Phillips, W. S., K. M. Mayeda, and L. Malagnini (2013), How to invert multi-band, regional phase amplitudes for 2-D attenuation and source parameters: Tests using the USArray, Pure Appl. Geophys., **171**, pp. 469-484.

Pitarka, A., R. J. Mellors, W. R. Walter, S. Ezzedine, O. Vorobiev, T. Antoun, J. L. Wagoner, E. M. Matzel, S. R. Ford, A. J. Rodgers, et al. (2015), Analysis of ground motion from an underground chemical explosion, Bull. Seismol. Soc. Am., **105**, no. 5, pp. 2390-2410, doi: 10.1785/ 0120150066.

Raoof, M., R. Herrmann, and L. Malagnini (1999), Attenuation and excitation of three-component ground motion in southern California, Bull. Seismol. Soc. Am., **89**, pp. 888-902.

Rodgers, A. J., N. A. Petersson, and B. Sjogreen (2010), Simulation of topographic effects on seismic waves from shallow explosions near the North Korean nuclear test site with emphasis on shear wave generation, J. Geophys. Res.-Sol. Ea., **115**, B11309, doi: 10.1029/2010JB007707.

Savran, W.H. and K.B. Olsen (2016), Model for Small-Scale Crustal Heterogeneity in Los Angeles Basin Based on Inversion of Sonic Log Data, Geophys. Res. Lett., **205**, pp. 856-863.

Shin, J. S., D.-H. Sheen, and G. Kim (2010), Regional observations of the second North Korean test on 2009 May 25, Geophys. J. Int., **180**, pp. 243-250.

Takemura, S., T. Furumura, and T. Maeda (2015), Scattering of high-frequency seismic waves caused by surface topography and small-scale velocity inhomogeneity, Geophys. Jour. Int., **201**, pp. 459-474.

Wagner, G. (2017), Parameterizing Subsurface Heterogeneity, presentation at the 2017 Air Force Research Laboratories Technical Information Meeting, Shark Center, Satellite Beach, FL, 18 October.

Wagner, G. and C. Langston (1992), A numerical investigation of scattering effects for teleseismic plane wave propagation in a heterogeneous layer over a homogeneous half-space, Geophysical Journal International, **110**, Issue 3, 1 September, pp. 486-500, https://doi.org/10.1111/j.1365-246X.1992.tb02087.x. Withers, K.B.,

K.B. Olsen, and S.M. Day (2015), Memory Efficient Simulation of Frequency Dependent Q, Bull, Seis. Soc. Am., **105**, pp. 3129-3142, doi: 10.1785/0120150020.

von Seggern, D. and R. Blandford (1972), Source time functions and spectra for underground nuclear explosions, Geophysical Journal International, **31**(1-3), pp. 83-97.

Wu, R.S., Z. Xu, and X.-P. Li (1994), Heterogeneity spectrum and scale-anisotropy in the upper crust revealed by the German Continental Deep-Drilling (KTB) Holes, Geophys. Res. Lett., **21**(10), pp. 911-914.

Xie, J., Z. Wu, R. Liu, D. Schaff, Y. Liu, and J. Liang (2006), Tomographic regionalization of crustal Lg Q in eastern Eurasia, Geophys. Res. Lett., **33**, L03315, doi 10.1029/2005GL024410.

APPENDIX A - Supplementary Material

This Appendix contains a description of the source time function used in the simulations, and comparison of data to synthetics at station TJN for the same tests as reported for INCN in the main text.

List of Figures

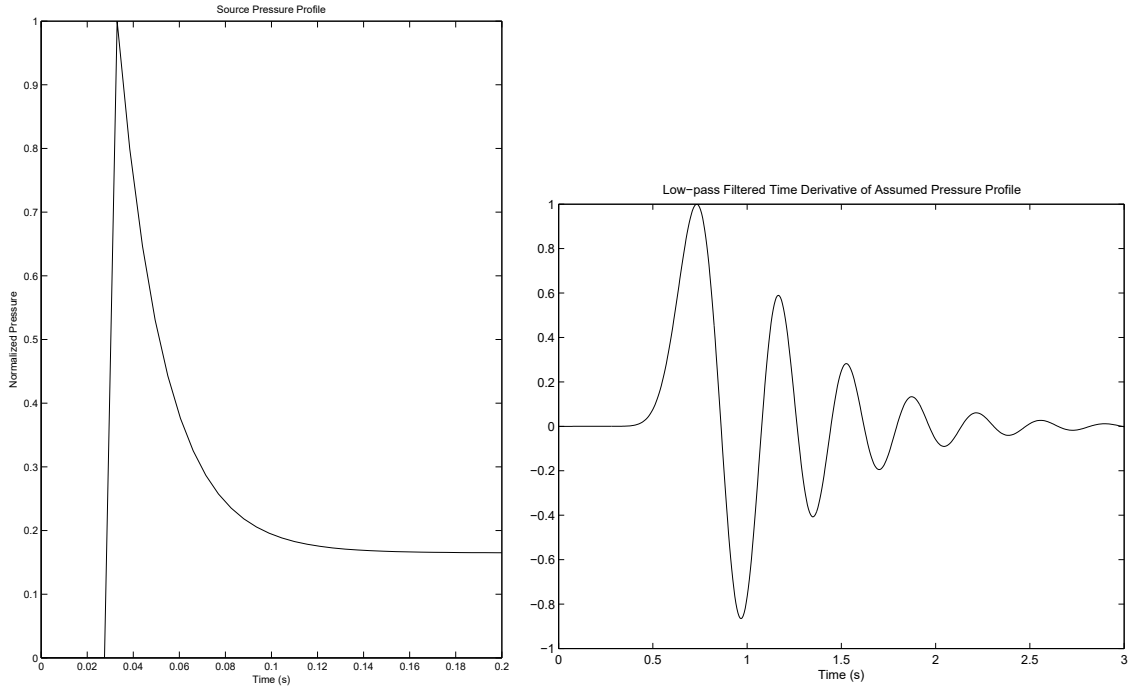

Figure A-1. Assumed Source (Left) Pressure Profile (exp(-50*dt)+0.15, Where dt is the Time Step in the Simulation), and (Right) its Low-pass Time Derivative, Inserted into the FD Simulation

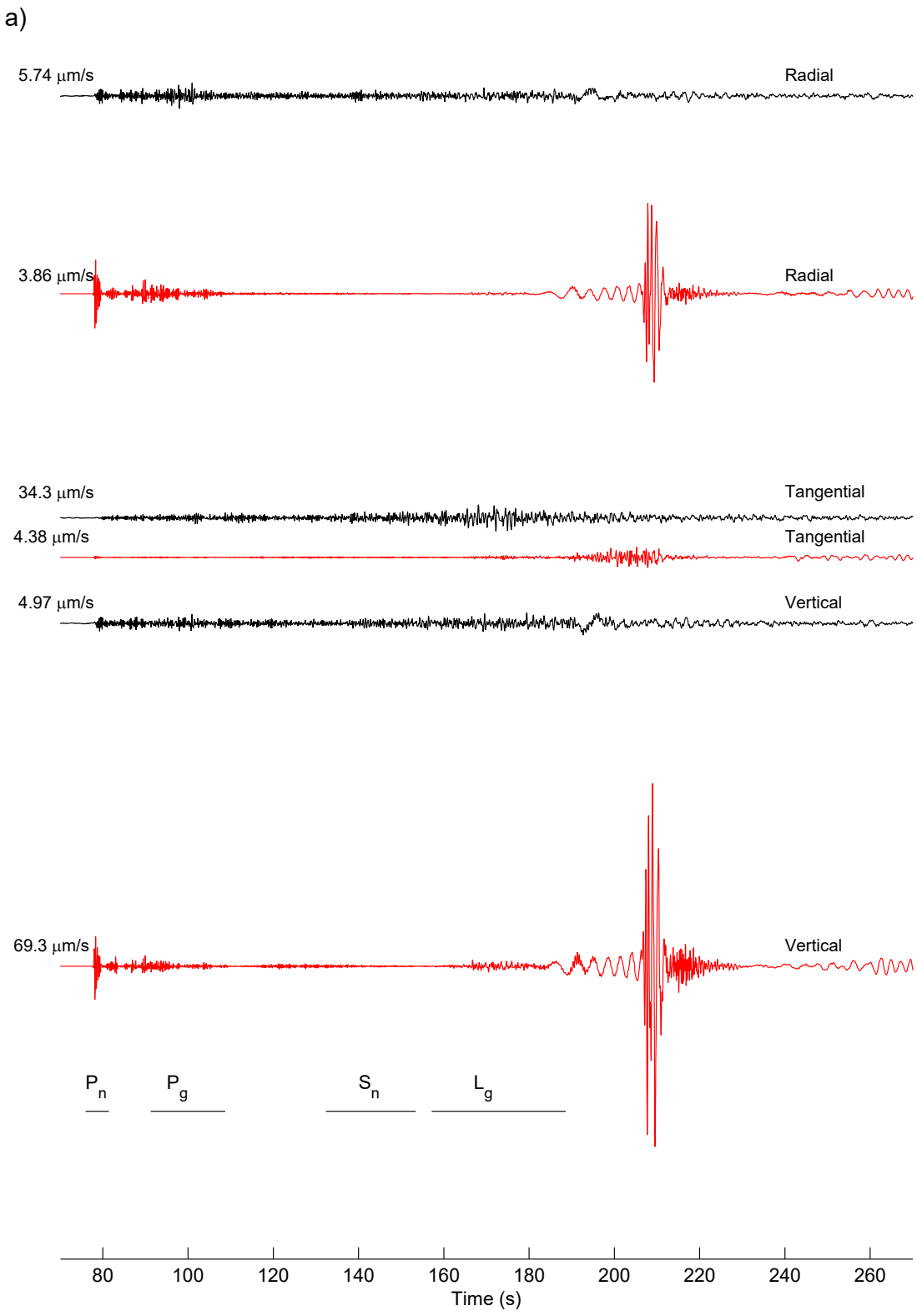

Figure A-2. Comparison of Observed (Black) and Synthetic Waveforms at TJN for the SALSA3D Model with Model 1 (Table 1) in (a) Time and (b) Frequency Domains

b)

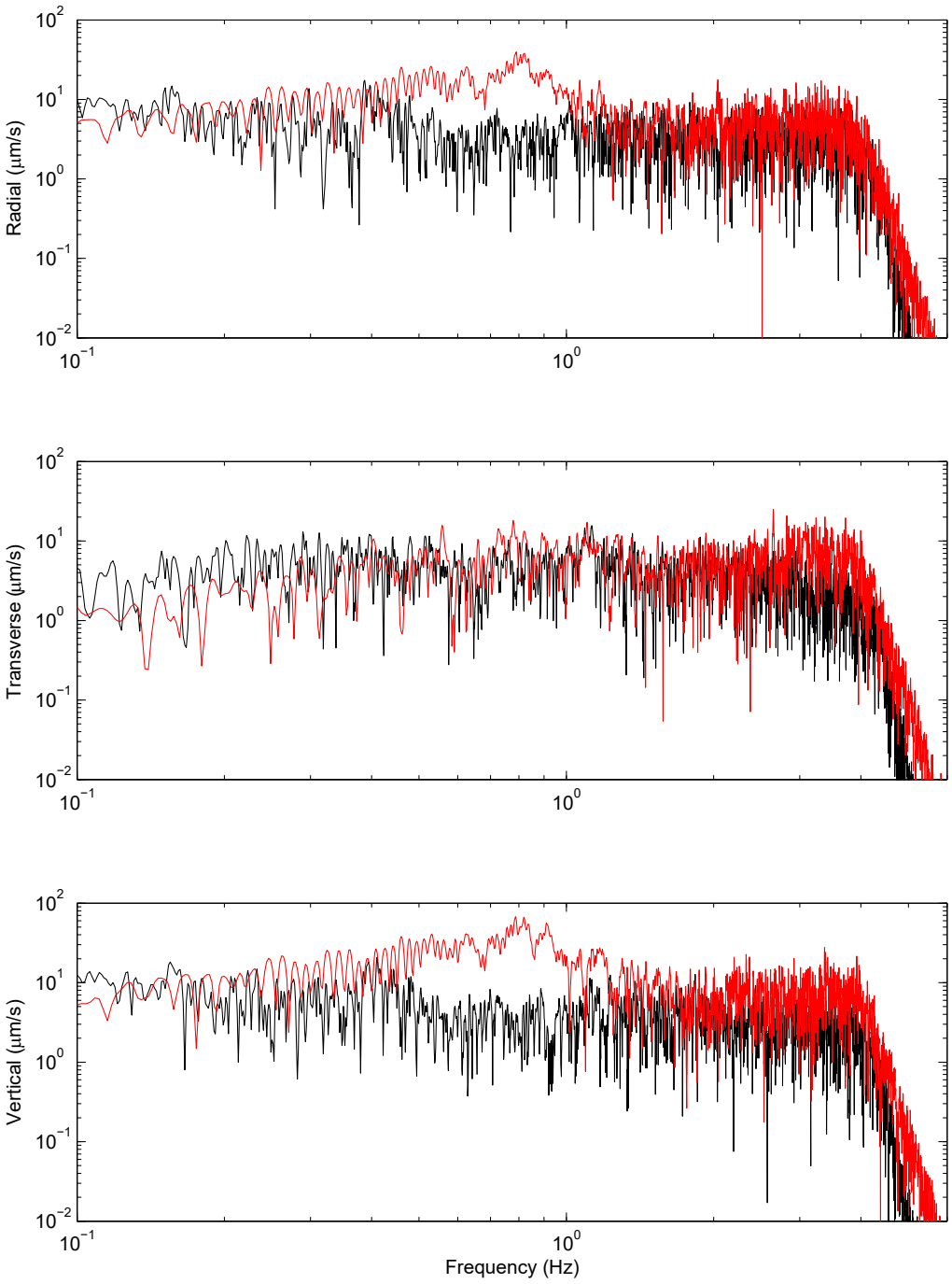

Figure A-2. (Cont.) Comparison of Observed (Black) and Synthetic Waveforms at TJN for the SALSA3D Model with Model 1 (Table 1) in (a) Time and (b) Frequency Domains

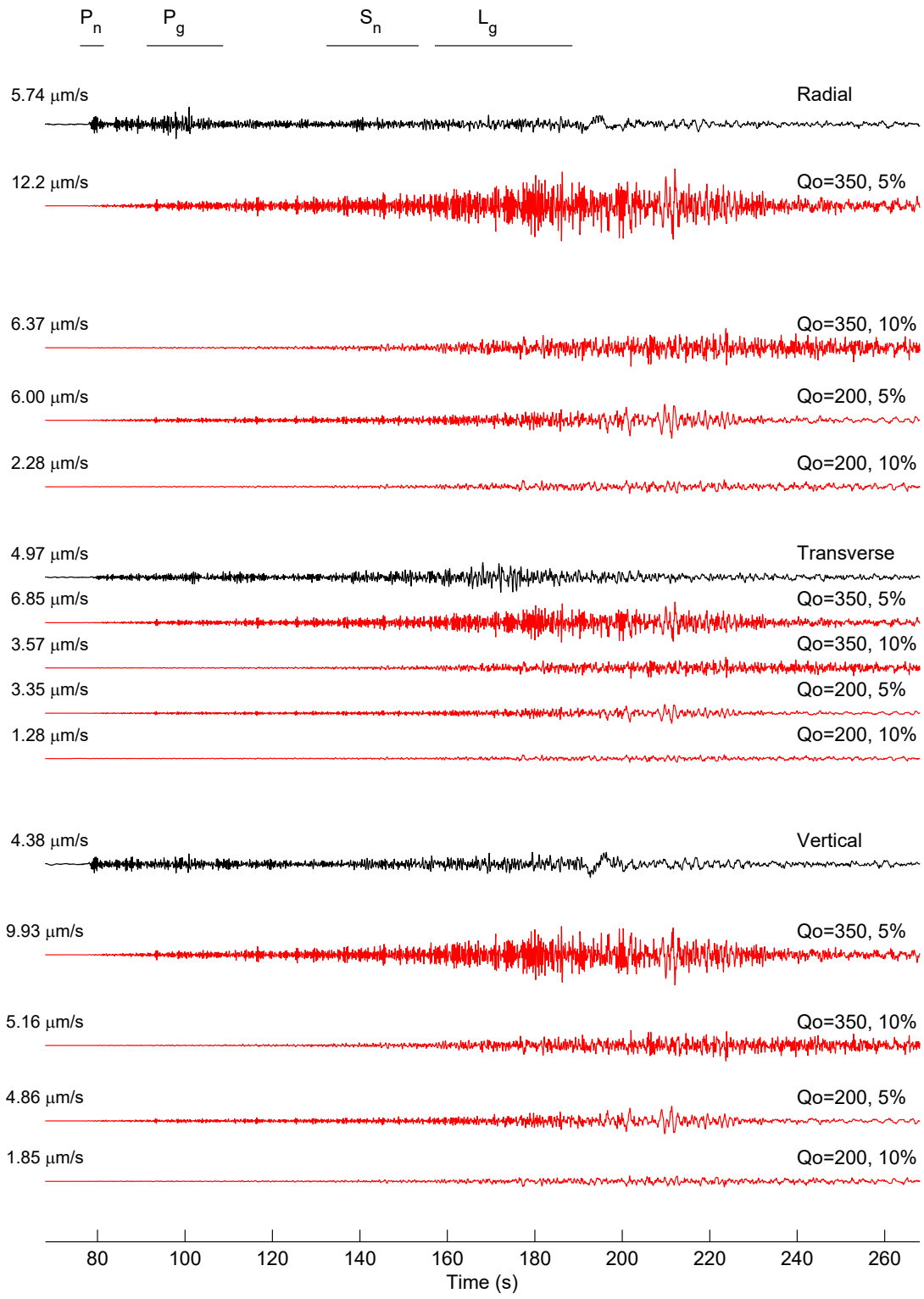

Figure A-3. Comparison of Observed (Black) and Synthetic Waveforms at TJN for the SALSA3D Model with Models 2-5 (Table 1)

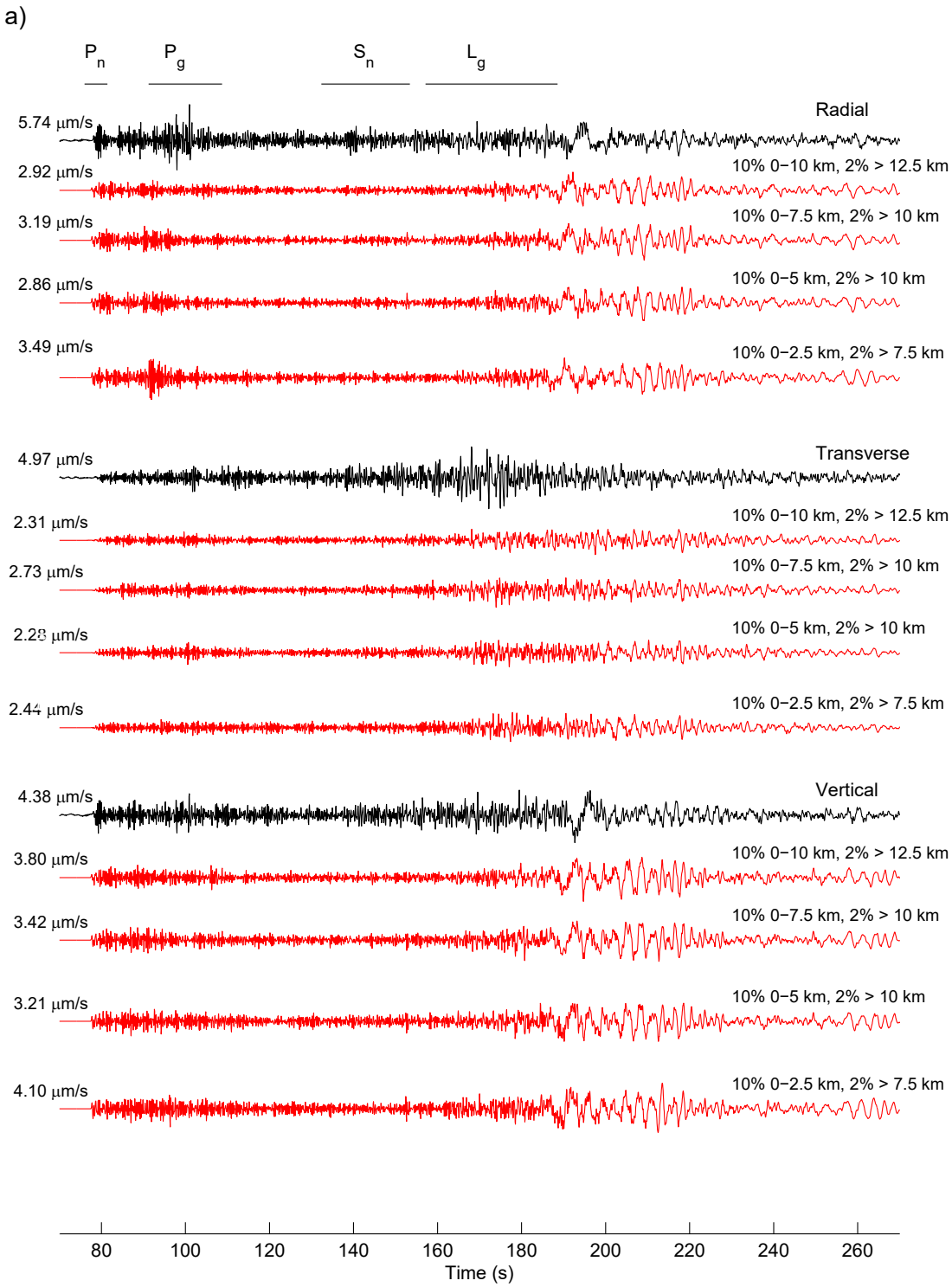

Figure A-4. (a) Comparison of Observed (Black) and Synthetic (Red) Waveforms at TJN for Models 6-9 (Table 1). The Gradient Models are all Characterized by s =10% from the Surface to a Depth of d1 km, s = 2% Below a Depth of d2 km, and a Linear Gradient in Between. The Values of d1 and d2 are Listed by the Synthetics. (b) Comparison in the Frequency Domain for Model 6 (Table 1)

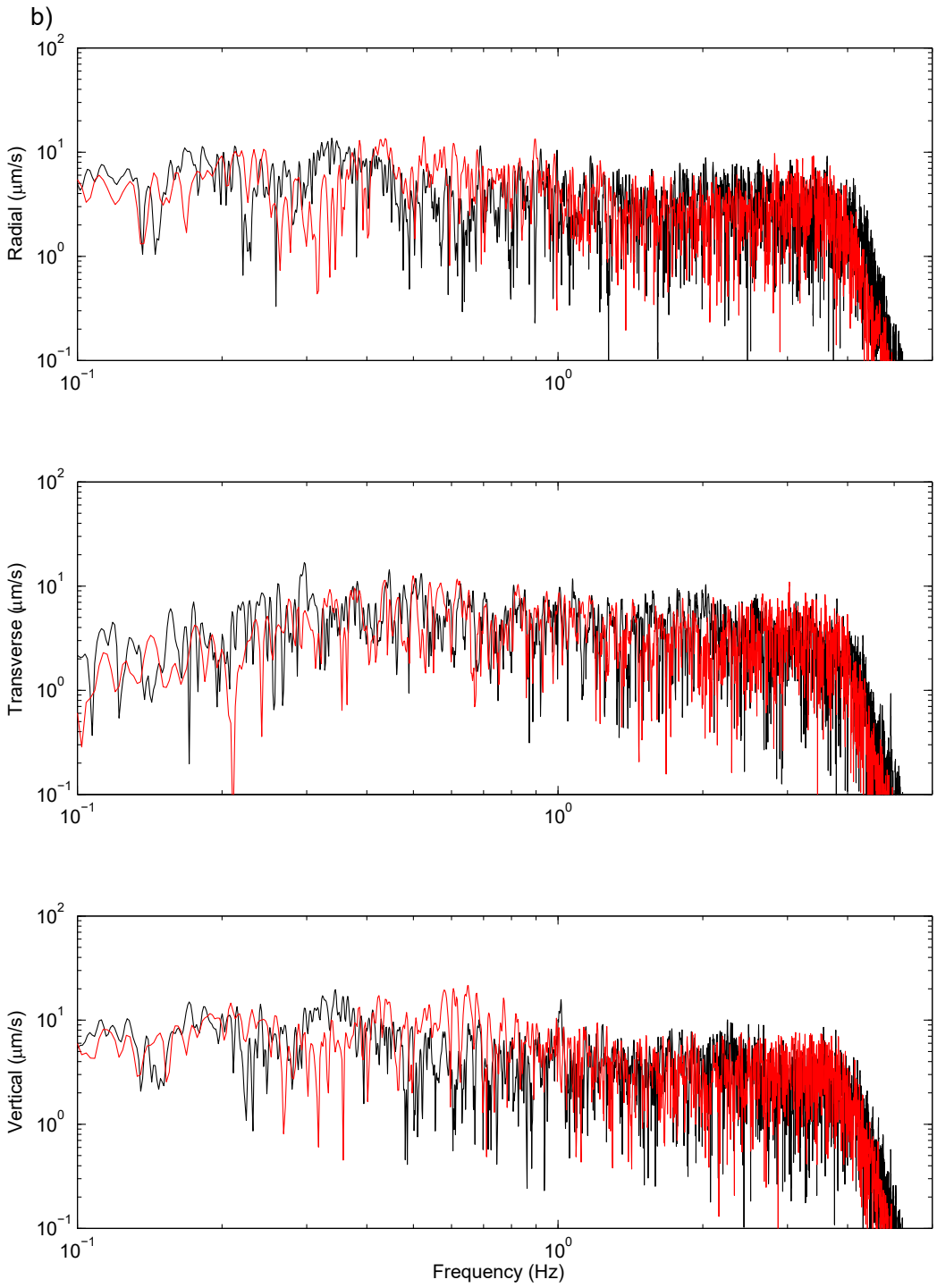

Figure A-4. (Cont.) (a) Comparison of Observed (Black) and Synthetic (Red) Waveforms at TJN for Models 6-9 (Table 1). The Gradient Models are all Characterized by σ = 10% from the Surface to a Depth of d_1 km, σ = 2% Below a Depth of d_2 km, and a Linear Gradient in Between. The Values of d_1 and d_2 are Listed by the Synthetics. (b) Comparison in the Frequency Domain for Model 6 (Table 1)

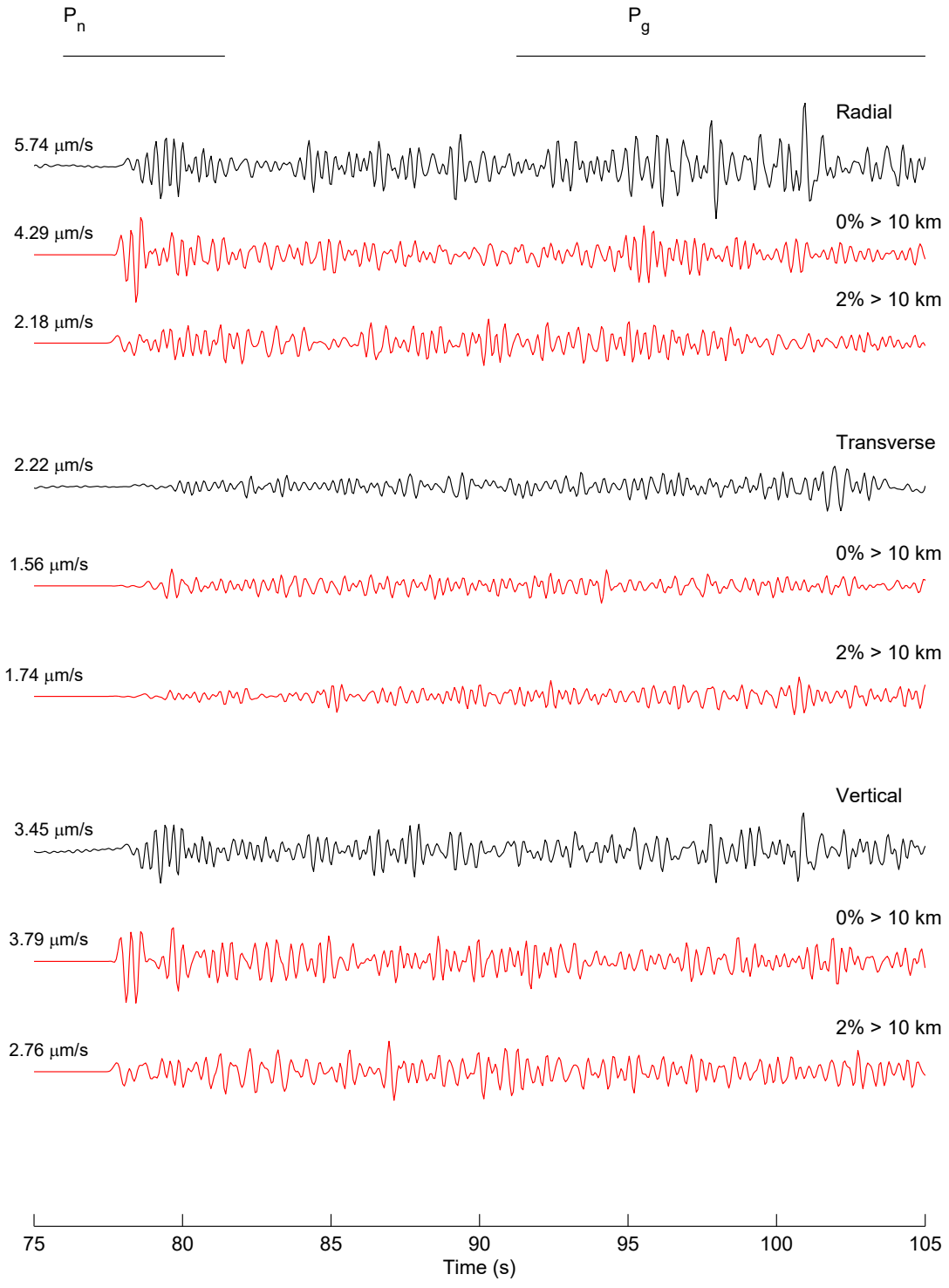

Figure A-5. Zoom of the Time Domain Comparison for TJN Using Models 7 and 7a (Table 1). Peak Velocities Listed Refer to the Time Interval Shown

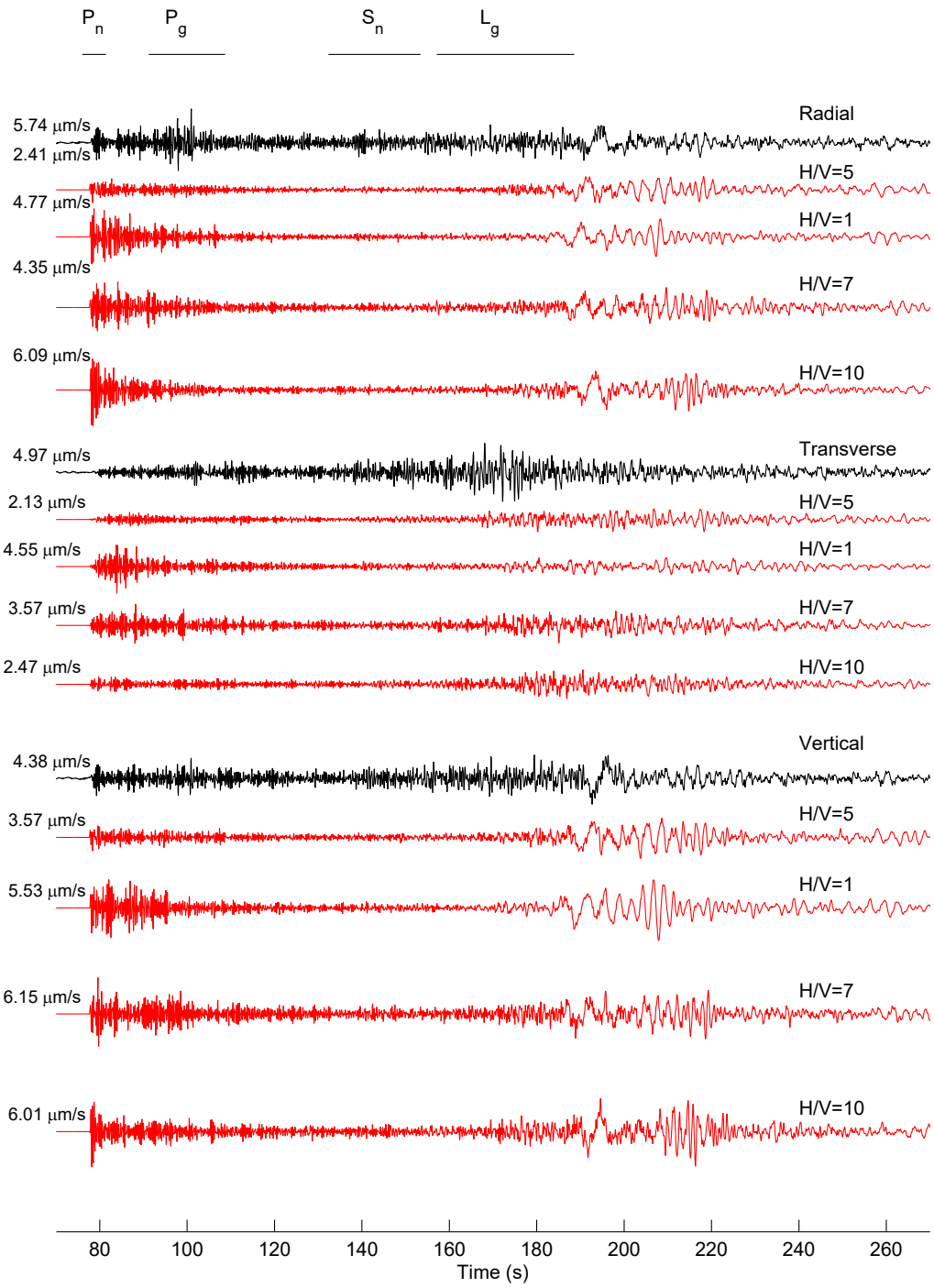

Figure A-6. Comparison at TJN of the Scattering Effects from Anisotropy in the Small-scale Heterogeneities, Quantified by the Ratio of Horizontal-to-vertical Dimensions of the Velocity and Density Perturbations (H/V). Results for H/V=1, 5, 7, and 10 (Models 10, 6, 11 and 12, Table 1) are Shown

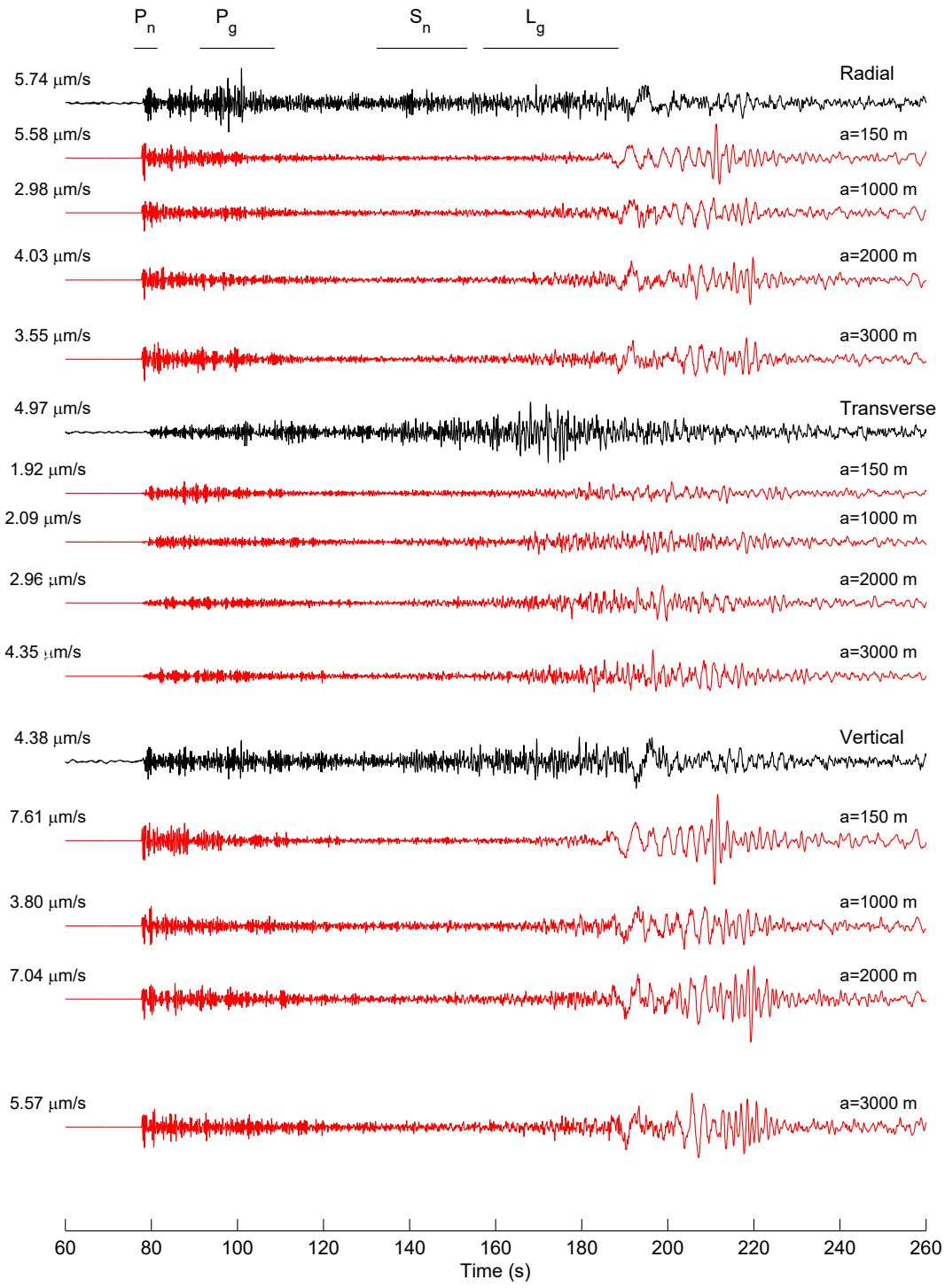

Figure A-7. Comparison at TJN of the Scattering Effects from Different Correlation Length in the Distribution of Small-scale Heterogeneities (150 m, 1,000 m, 2,000 m, and 3,000 m) as Defined by Models 13, 6a, 14 and 15 (Table 1)

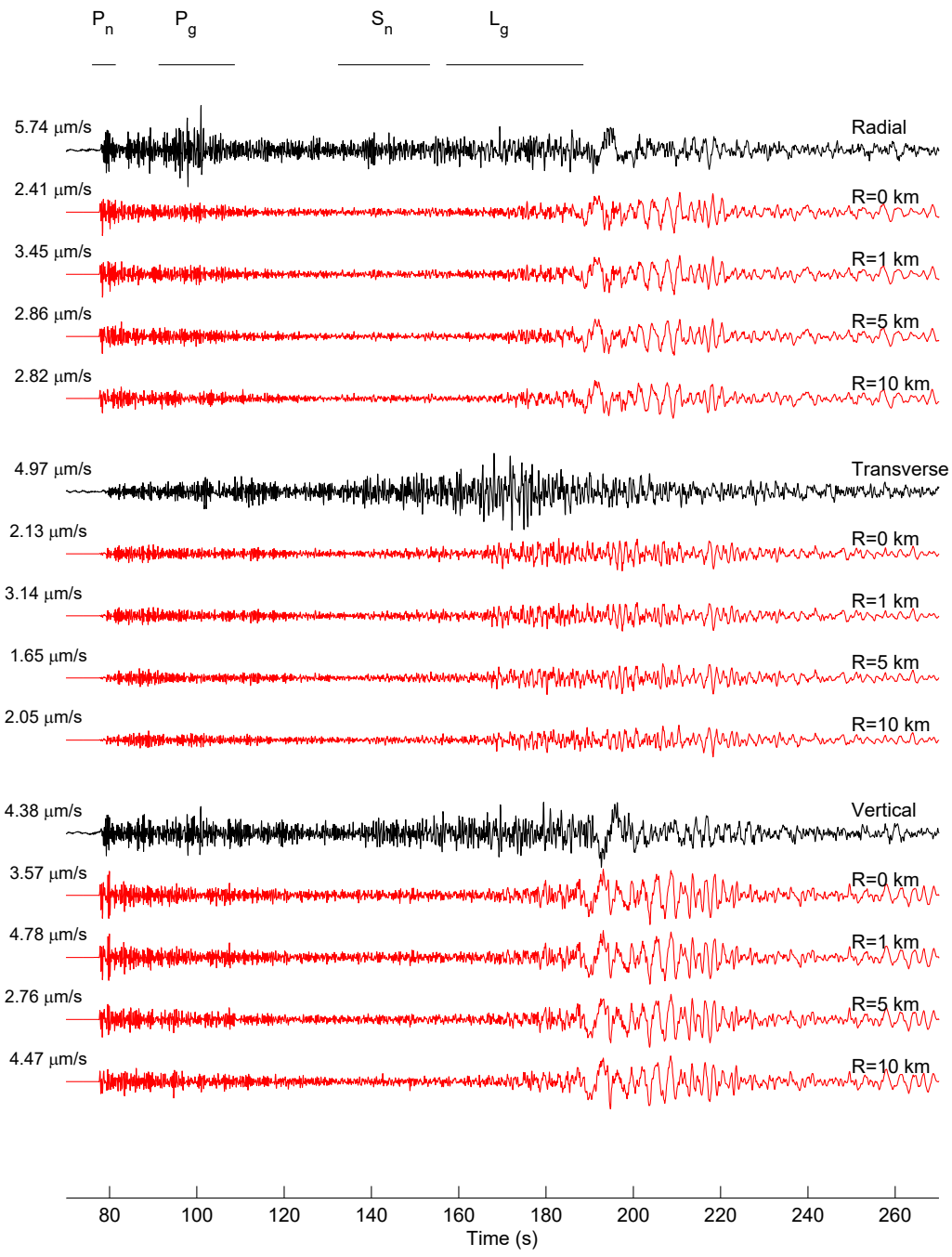

Figure A-8. Significance of Near-source Scattering Effects from Small-scale Heterogeneities at TJN. The Small-scale Heterogeneities (Model 6, Table 1) Have Been Removed Within radii (R) of 0-10 km from the Source, Listed by the Synthetics

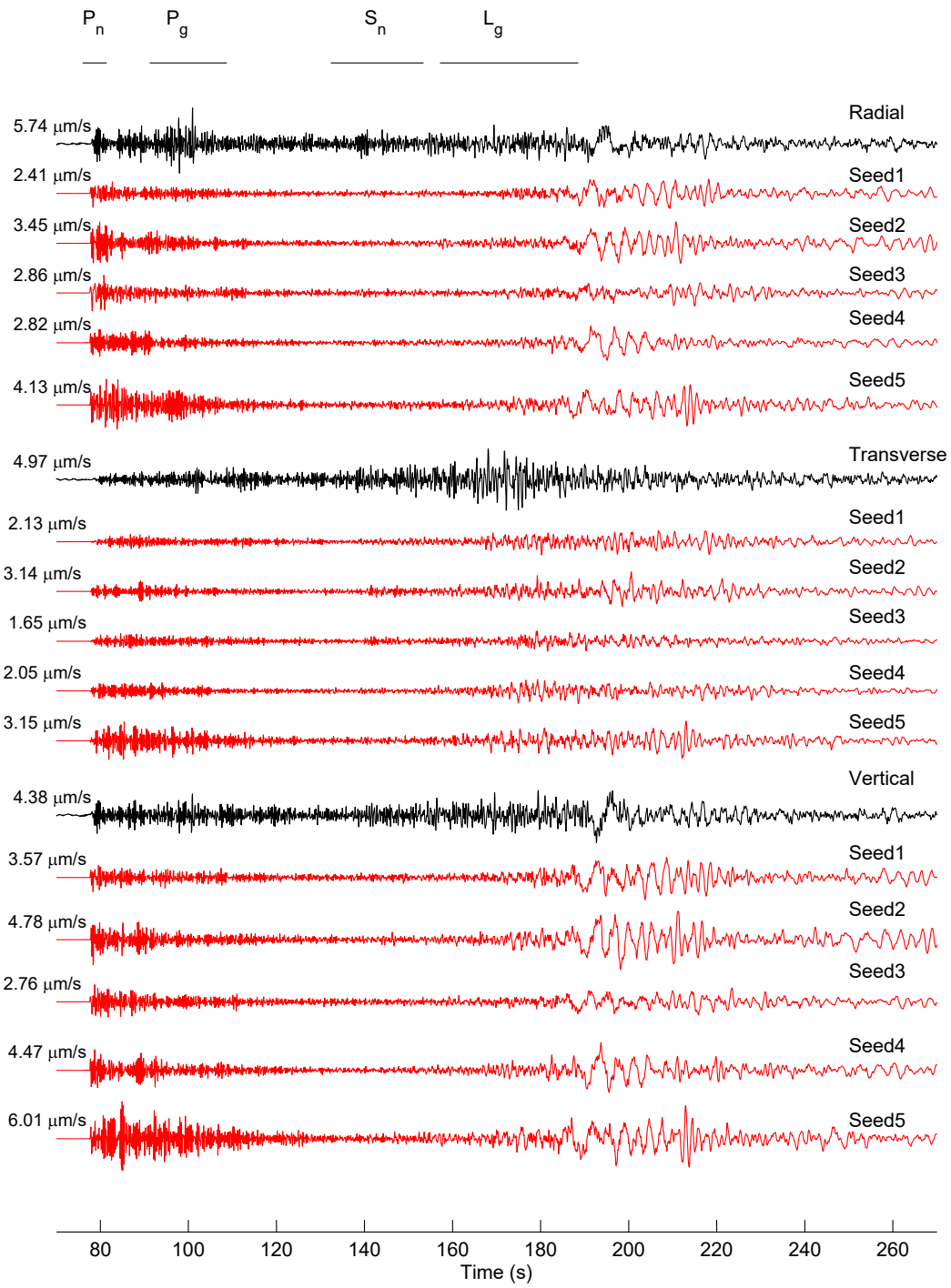

Figure A-9. Comparison of Data to Synthetics Generated from a 5-realization Ensemble of Statistical Models of Small-scale Heterogeneities with Different Seed Numbers at TJN. All Simulations use the Q(f), H, a, H/V and σ of Models 16-20 (Table 1)

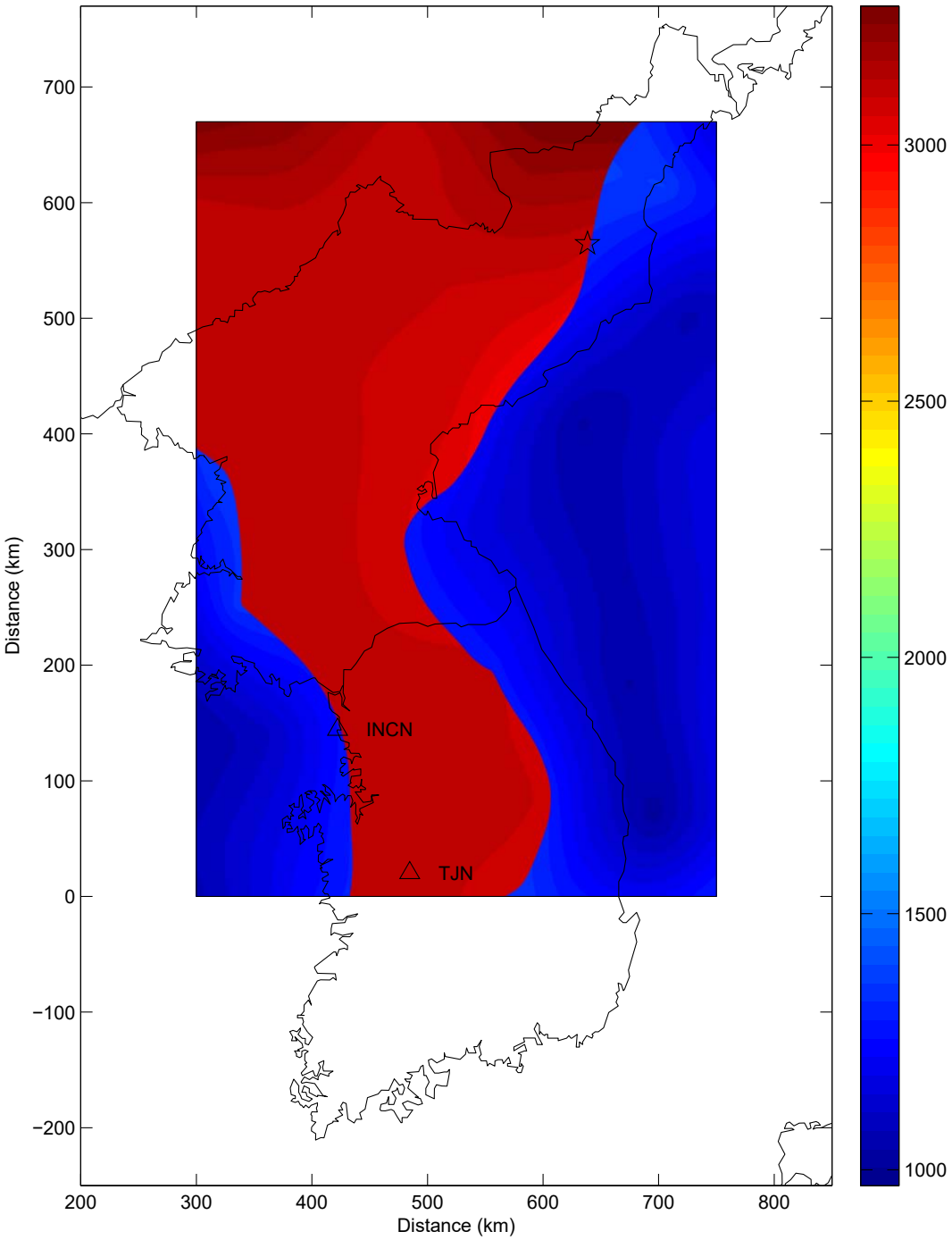

Figure A-10. V_s (m/s) at the Surface (z=0 km). The Star Denotes the Source Location for the May 25 2009 North Korea Nuclear Test. Two Stations (INCN, TJN) in South Korea with Instrument-corrected Records Available Used in This study are Shown by Triangles

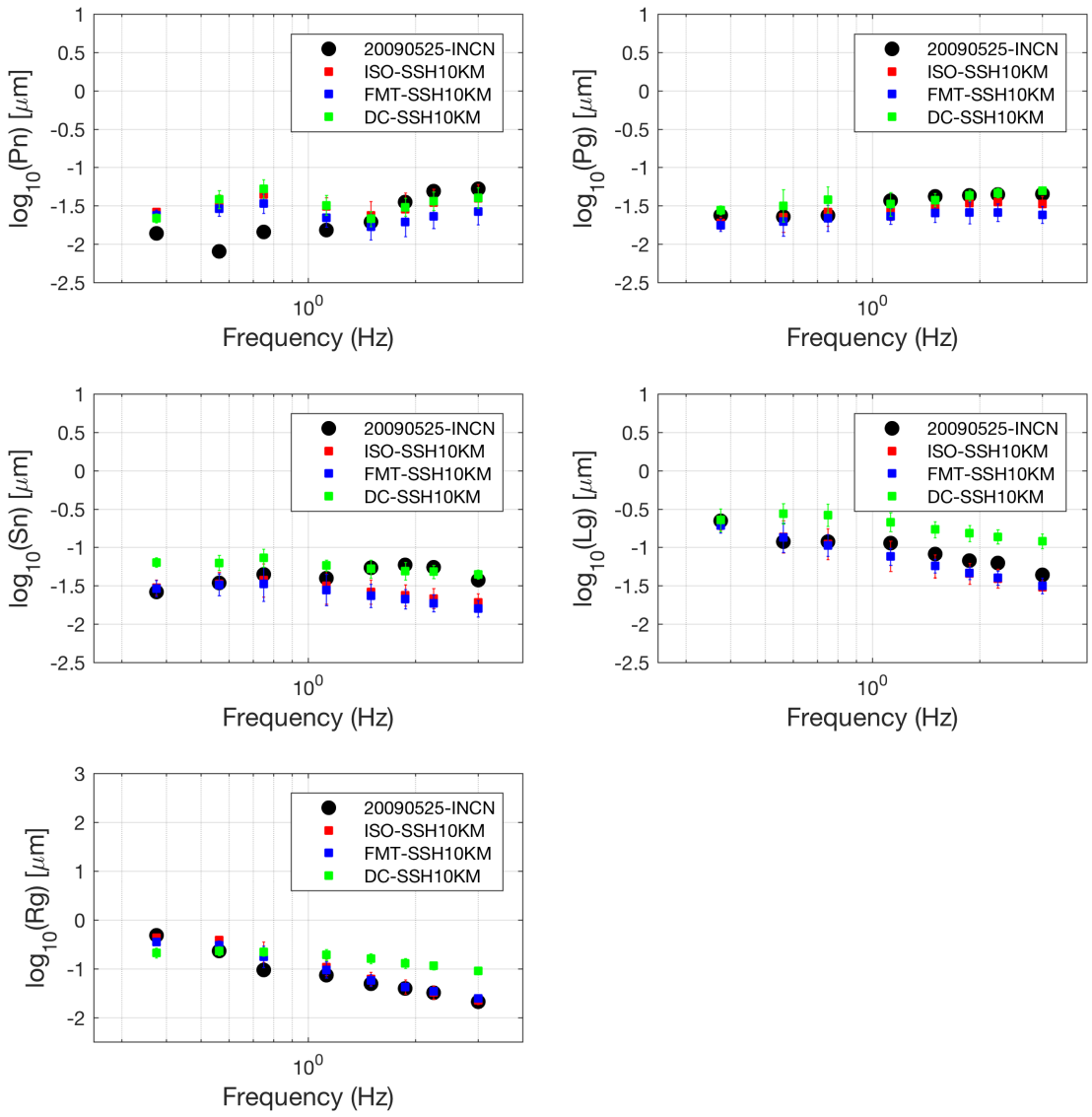

Figure A-11. (Top) RMS Phase Amplitudes and Ratios in Different Frequency Bands Measured from the Observed (Black) and Synthetic (Red: Isotropic Source, Blue: Moment Tensor Source by Chiang et al. (2018), Green: 10 km Double-couple Source) Vertical Velocity Component at INCN. Error Bars Indicate One Standard Deviation of the Mean. Similar to Figures 15-21, but for the Model with Small-scale Heterogeneities Extended to 10 km Depth

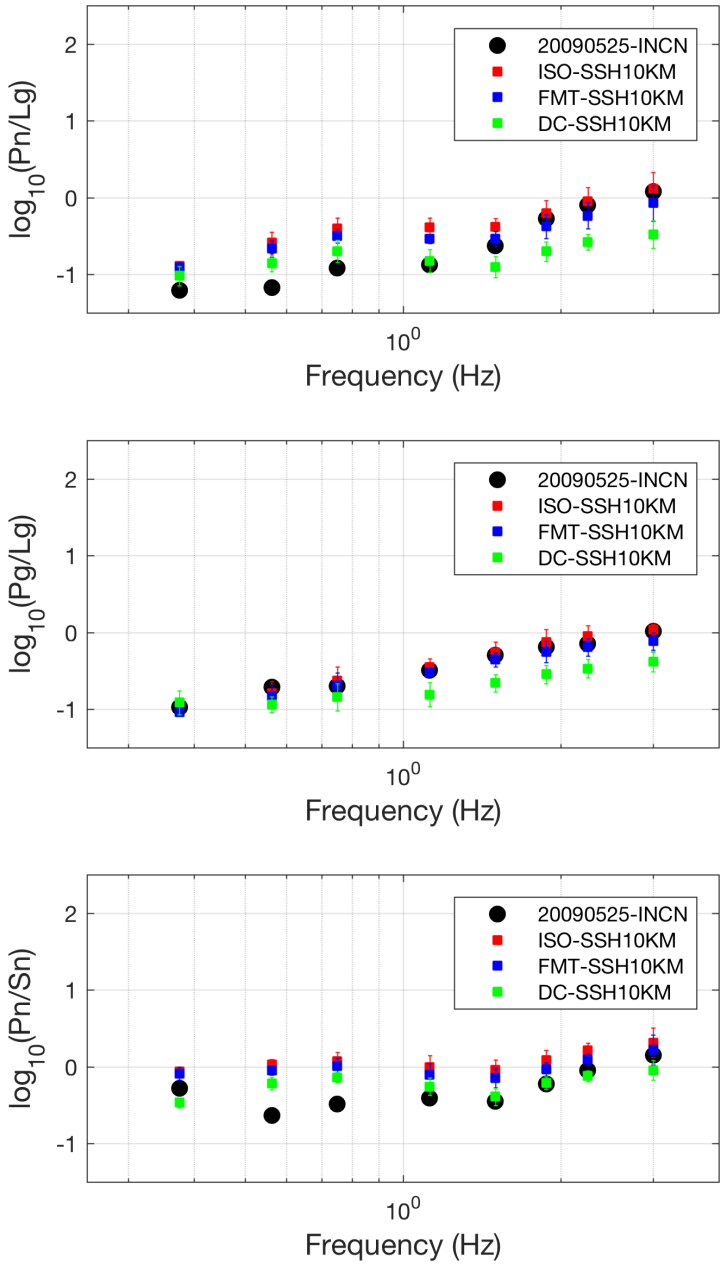

Figure A-11. (Cont.) (Top) RMS Phase Amplitudes and Ratios in Different Frequency Bands Measured from the Observed (Black) and Synthetic (Red: Isotropic Source, Blue: Moment Tensor Source by Chiang et al. (2018), Green: 10 km Double-couple Source) Vertical Velocity Component at INCN. Error Bars Indicate One Standard Deviation of the Mean. Similar to Figures 15-21, but for the Model with Small-scale Heterogeneities Extended to 10 km Depth

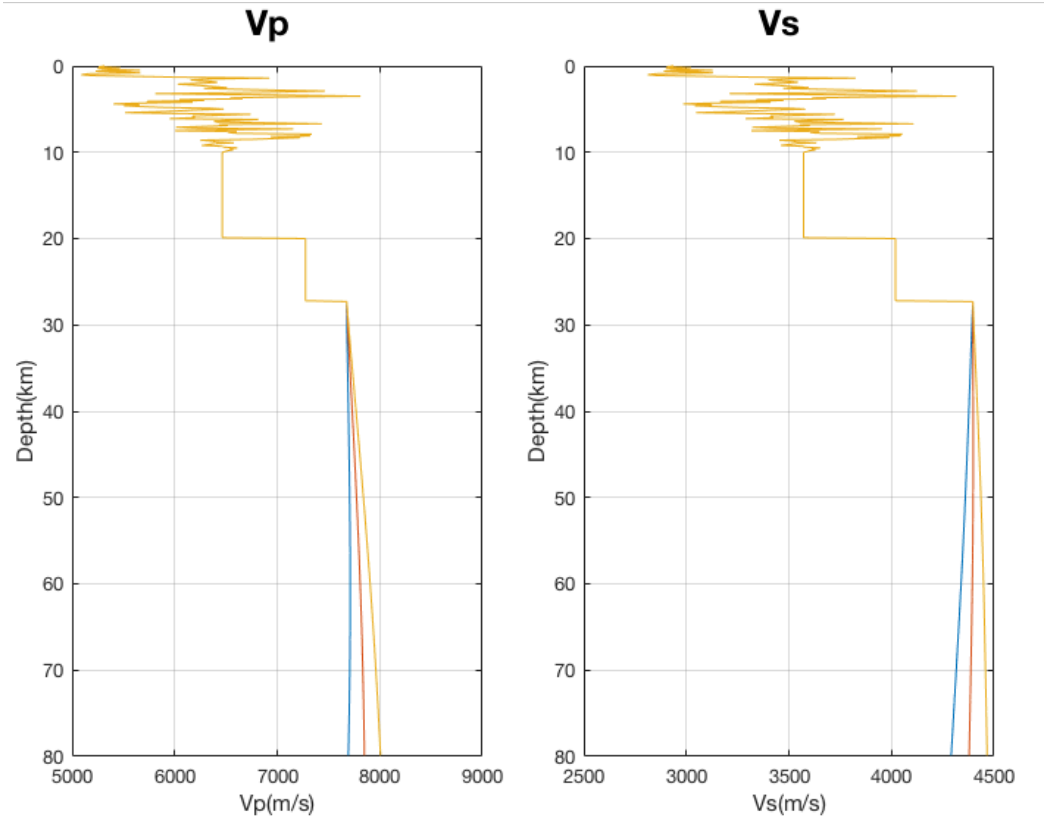

Figure A-12. Example of Vp and Vs Profiles of the Original Model (Red), and Those with -2% (Blue) and +2% (Yellow) Perturbations in the Velocity Gradients

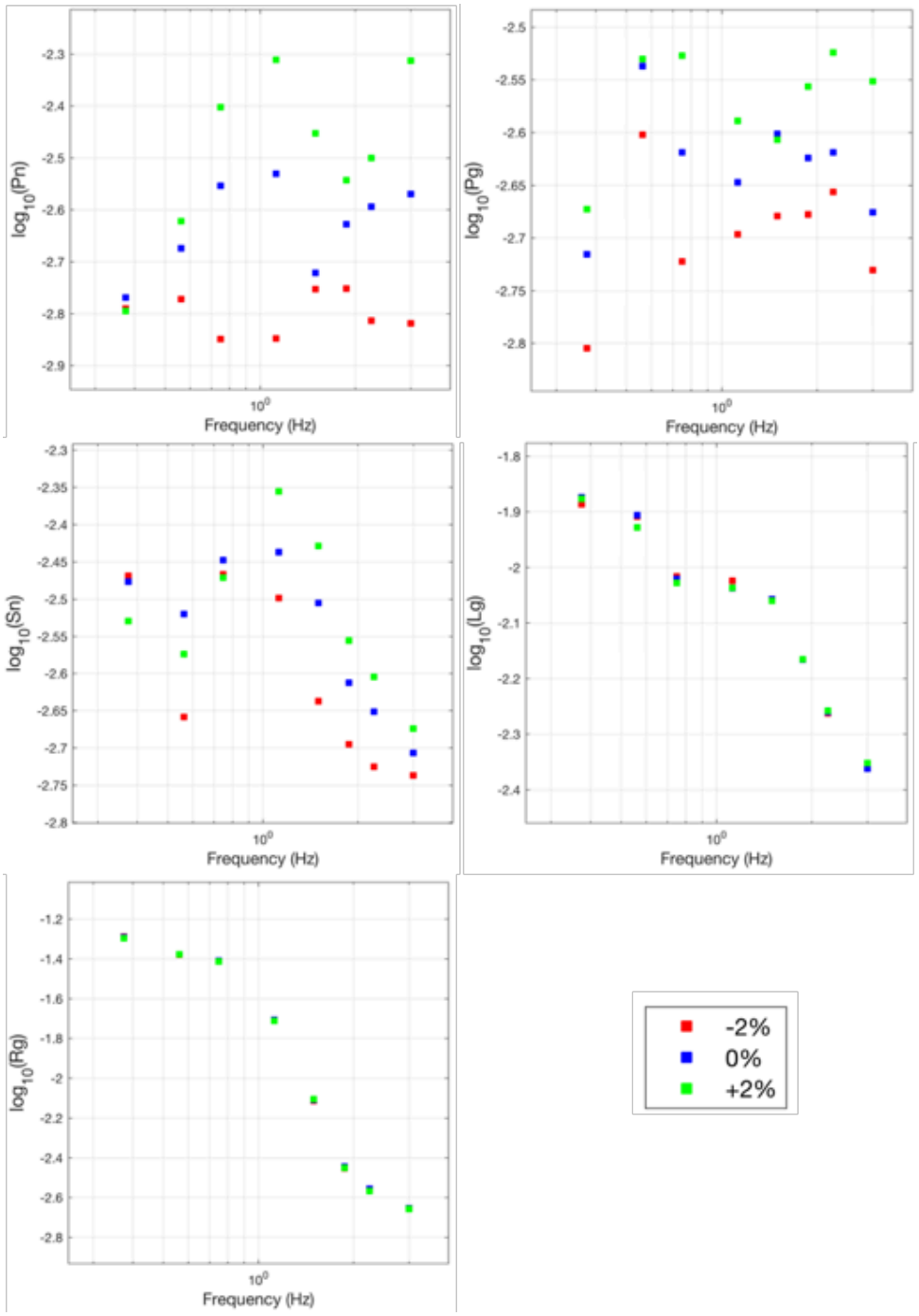

Figure A-13. Comparison of Amplitudes of Pn, Pg, Sn, Lg, and Rg at Different Frequencies Measured from Three 2D Simulations of the Unperturbed SALSA3D Model Cross-section (Blue), and Those Where we Applied -2% (Red) and +2% (Green) Perturbations on Both Vp and Vs Gradients in the Upper Mantle

Appendix B - Publications and Presentations

Olsen, K.B., B.H. Jacobsen, M. Begnaud, and S.W. Phillips (2017), Constraints on Crustal Heterogeneity and Q(f) from Regional (<4 Hz) Wave Propagation for the 2009 North Korea Nuclear Test, *Seism. Res. Lett* **88**, 2B, 2017, p 622.

Olsen, K.B., M. Begnaud, S. Phillips, and B.H Jacobsen (2018), Constraints of Crustal Heterogeneity and Q(f) From Regional (<4Hz) Wave Propagation for the 2009 North Korea Nuclear Test, *Bull. Seis. Soc. Am.*, **108(3A),** pp. 1369-1383.

Yeh, Te-Yang and K.B. Olsen (2018), Seismic Scattering from Topography and Small-Scale Crustal Heterogeneity: Application to the 2009 North Korean Nuclear Test, SSA, *Seism. Res. Lett.* **89**, 2B, p. 879.

Yeh, T.-Y. and K. B. Olsen (2019), Modeling 0-2 Hz 3D Wave Propagation of the North Korean Nuclear Tests Across the Sea of Japan, *Seism. Res. Lett.* **90**, 2B, p. 869.

LIST OF SYMBOLS, ABBREVIATIONS, AND ACRONYMS

AWP-ODC	Anelastic Wave Propagation-Olsen-Day-Cui
AFRL	Air Force Research Laboratory
HPC	High Performance Computing
NKNTS	North Korea Nuclear Test Site
ORNL	Oak Ridge National Laboratory
PSD	Power Spectral Density
RSTT	Regional Seismic Travel Time package
SALSA3D	SAndia LoS Alamos 3D
SSH	Small Scale Heterogeneities

DISTRIBUTION LIST

DTIC/OCP
8725 John J. Kingman Rd, Suite 0944
Ft Belvoir, VA 22060-6218 1 cy

AFRL/RVIL
Kirtland AFB, NM 87117-5776 1 cy

Official Record Copy
AFRL/RVB/Dr. Frederick Schult 1 cy